NEPAL JOURNAL OF SCIENCE AND TECHNOLOGY

Vol.22(2)

NEPAL ACADEMY OF SCIENCE AND TECHNOLOGY
KATHMANDU, NEPAL

Nepal Journal of Science and Technology (NJST) Board Members

NEPAL ACADEMY OF SCIENCE & TECHNOLOGY
CENTRAL OFFICE
NAST

Editorial Message from the Editor-in-Chief

Warm greetings from the *Nepal Journal of Science and Technology (NJST)*.

It gives me immense pleasure to present Volume 22(2) of NJST, a peer-reviewed multidisciplinary journal published biannually by the Nepal Academy of Science and Technology (NAST). NJST has been continuously striving to provide a credible platform for the dissemination of original research, reviews, perspectives, and communications in the diverse fields of applied and natural sciences.

In this issue, we are pleased to publish 10 peer-reviewed manuscripts contributed by national and international scholars. These papers represent a wide range of disciplines within science and technology and reflect the dedication of the research community to advancing knowledge and addressing pressing challenges. We believe the contributions included here will inspire further exploration, collaboration, and innovation.

The continued growth of NJST is possible only through collective effort. I would like to extend my sincere appreciation to the Advisory Board, Editorial Board, Managing Editor, Associate Editor, Journal publishing unit of Promotion and Publicity Division and especially our reviewers for their invaluable time and expertise in maintaining the academic rigor of this publication. I am equally grateful to our contributing authors who have chosen NJST to share their research work, thereby enriching the scientific discourse that this journal seeks to promote.

I hope this issue will inspire further research, innovation, and collaboration in the scientific community. Wishing you all continued success in your academic and professional endeavors.

Prof. Dr. Dilip Subba
Editor-in-Chief
Nepal Journal of Science and Technology (NJST)
Vice Chancellor
Nepal Academy of Science and Technology (NAST)

Address : Khumaltar, Lalitpur, Nepal, GPO Box 3323 Kathmandu, E-mail: Info@nast.gov.np
Telephone: +977-1-5547715, 5547720, 5547721, 5553132, Fax: 977-1-5547713

May 2018

Table of Contents

Evaluating the Mechanical Properties of Concrete with the use of Coconut Fiber

Khem Raj Joshi[1*], Bharat Mandal[2] and Tarumay Ghoshal[2]

[1] *Department of Civil Engineering, DIT University, Uttarakhand, India*

[2] *Department of Civil Engineering, TU Institute of Engineering, Pulchowk Campus, Nepal*

***CORRESPONDING AUTHOR:**

Khem Raj Joshi
Email:khemjoshi1978@gmail.com

ISSN : 2382-5359(Online), 1994-1412(Print)

DOI:
https://doi.org/10.3126/njst.v22i2.78601

Date of Submission: 16 Apr, 2024

Date of Acceptance: 11 Dec, 2024

ABSTRACT

Coconut fiber is readily available, it is a good substitute for steel fiber in concrete. Additionally, it offers coconut farmers a new revenue stream as demand from the construction sector increases. These natural fibers can be a cost-effective way to dispose of coir mattress waste and, being environmentally friendly, they can significantly reduce environment pollution from burning it. However, it is crucial to assess whether the use of these fibers affects the strength of concrete, determining their suitability for widespread use in the construction industry or identifying potential concerns.

This study aims to compare the strength of reinforced concrete without coconut fiber to that with coconut fiber reinforced concrete at various fiber concentrations. Tests were conducted with different fiber percentages (1%, 3%, and 5% by weight of cement) to evaluate the compressive, split tensile, and flexural strength of coconut fiber reinforced concrete. The results indicate that coconut fiber enhances both the flexural and compressive strength of concrete, along with improving its ductile behavior.

Keywords : *Tensile strength, Compressive strength, Flexural strength, Coconut Fiber.*

1. INTRODUCTION

Coconut fiber, an agricultural byproduct from processing various coconut products, is abundant in tropical regions like Africa, Asia, and America. Often discarded as waste, coconut fiber can be repurposed into valuable products such as floor mats, doormats, brushes, and cushions. This repurposing helps reduce the accumulation of coconut coir waste in soil and water resources.

In the construction industry, coconut fiber is gaining attention as a building material. Researchers have demonstrated its potential in cementitious composites, offering advantages over synthetic fibers, which can suffer from poor fire resistance, decreased

workability, and reduced shear strength (Khan et al., 2017).

While the use of fibers in reinforced concrete can be debated due to issues like exposure to rainfall and random fiber orientation, fiber-reinforced concrete (FRC) presents a cost-effective solution for affordable housing and secondary structures, especially in developing countries. The construction industry is evolving with innovative materials like high-performance concrete (HPC), which are environmentally friendly. Consequently, research on fibers, matrix materials, and production techniques has intensified.

FRCs, known for their high tensile strength-to-weight ratio and weather resistance, can be molded into various forms and used in secondary structures and offshore platforms (Thomas and Ramaswamy, 2007). Studies indicate that FRC offers significant opportunities for low-cost, non-traditional building materials (Olanipekun et al., 2006; Nor et al., 2010). Coconut fiber in particular, reduce crack in concrete (Adeyemi, 1998; Zain et al., 2010), providing an environmentally compliant disposal method for industrial coconut waste.

Recent research highlights the suitability of coconut fiber-reinforced concrete (CFRC) and coconut-fiber ropes in earthquake-resistant construction. CFRC has shown greater load resistance and reduced disintegration under seismic loading compared to conventional concrete, making it ideal for seismic-resistant structures (Kirandeep, 2023; Ali, 2016; Ali, 2014). Additionally, the biodegradable and non-toxic nature of coconut fibers promotes sustainability, reducing environmental impact (Martinelli et al., 2023; Ahmad et al., 2022). These fibers enhance the mechanical properties of concrete, including tensile, flexural, shear, and torsional strength, while preventing crack formation, improving load-bearing capacity, and increasing energy absorption (Martinelli et al., 2023; Ahmad et al., 2022).

Coconut fibers present a cost-effective alternative to synthetic fibers for use in construction materials (Ahmad et al., 2020; Agrawal et al., 2014). When treated with substances like sodium hydroxide, these fibers enhance the durability of concrete and resist decay (Martinelli et al., 2023; Naamandadin et al., 2020). Research indicates that an optimal fiber content of around 3% by weight significantly improves mechanical properties while maintaining a balance between workability and compressive strength (Ahmad et al., 2022; Naamandadin et al., 2020).

Choosing the optimal fiber content can improve torsion, toughness and tensile strength of concrete (Yalley & Kwan, 2009; Agrawal et al., 2014; Ahmad et al., 2022; Naamandadin et al., 2020). The use of coconut fiber-reinforced concrete (CFRC) as high-strength concrete is beneficial for its mechanical properties, energy absorption, and toughness indices. Additionally, CFRC fibers with lengths of 50 mm and 75 mm significantly enhance flexural and shear strength, making them suitable for paving block mixtures (Mudiyono & Sudarno, 2019).

This study focuses on the intrinsic use of coconut fiber in concrete, exploring its impact on mechanical properties and the effect of different fiber proportions on concrete strength.

2. MATERIALS AND METHODS

This study focuses on a comparative analysis of the strength of CFRC and normal concrete, as well as the impact of fiber length on concrete properties. Rabma, S et al. (2020) achieved optimal compressive and flexural strength with 5% coconut fiber compared to 10% and 15%. Similarly, Dharmik et al. (2021) found that concrete with 1% coconut fiber by weight of cement showed an increase in compressive strength. Consequently, processed coconut fibers of 3 cm length were used in experiments with fiber levels of 1%, 3%, and 5% by weight of cement. The suitability of various materials for concrete was first determined through material tests. The design mix was prepared according to IS 10262: 2009 with appropriate water content to prevent bleeding. Slump tests were conducted to ensure workability, and the cubes were sun-dried after 7 days wet curing up to 28 days before testing.

(i) Mixed Design

The mix design of M20 concrete is is prepared according to guidelines such as IS 10262: 2009, ensuring proper mixing, compaction, and curing to prevent issues like bleeding and segregation.

(ii) Slump Test

The slump test, as outlined in IS 1199:1959, is used to assess the workability of fresh concrete. The slump test observation it presents in the Table 2.

(iii) Bonding Length Test

The bonding length test typically involves embedding a single fiber in a concrete specimen and subjecting it to tensile forces until failure occurs. The critical length at which the fiber can no longer sustain the load without slipping or breaking is identified as the bonding length.

(iv) Compressive Strength Test

This test involves casting concrete into cube molds, of dimensions 150mm x 150mm x 150mm, and curing them for specified periods, of 7 and 28 days. After curing, the cubes are placed in a compression testing machine, which applies a gradually increasing load until the specimen fails. The maximum load at failure is recorded, and the compressive strength is calculated by dividing this load by the cross-sectional area of the cube.

(v) Splitting Tensile Strength Test

The splitting tensile strength test of concrete is performed, as per Indian Standard IS 5816:1999. This test involves placing a cylindrical concrete specimen horizontally between the platens of a compression testing machine. A diametrically opposed compressive load is then applied along the length of the cylinder until it splits along the vertical diameter. The maximum load at failure is recorded, and the tensile strength is calculated using a specific formula provided in the standard.

(vi) Flexural Strength Test

The single point flexural test of concrete, as per the Indian Standard IS 516:1959, involves determining the flexural strength of concrete using a simple beam with a single point load applied at the center is adopted for flexural strength test. The test specimen, typically a beam of dimensions 150 mm x 150 mm x 700 mm, is placed on two supporting rollers spaced 600 mm apart. A load is then applied at the midpoint of the beam until failure occurs. The flexural strength is calculated using the formula

$$Flexural\ Strength = \frac{bd^2}{PL},$$

where (P) is the maximum load applied, (L) is the span length, (b) is the width, and (d) is the depth of the specimen. This method provides valuable insights into the concrete's ability to withstand bending forces, which is critical for designing durable and resilient structures and adopted by researchers.

3. RESULTS AND DISCUSSION

(i) Mixed Design

The mix design of FRC incorporates fibers to enhance its mechanical properties, particularly tensile strength and crack resistance. A mix design was carried out according to IS 10262 –1982 to achieve a minimum target strength of 20 N/mm². This same mix design was applied to the FRC. The quantities of different ingredients per cubic meter of concrete mix are provided below.

Grade of concrete	: M20
Types of cement	: OPC
Cement Content	: 400kg/m^3
Aggregate Content (695 kg/m^3)	: 40% of 20mm
(455 kg/m^3)	: 60% of 40mm
Sand Content	: 700 kg/m^3
Water cement ratio	: 0.45
Workability (Slump)	: 95mm
Chemical Admixture	: 2 kg/m^3

Table 1: Strength during Trial Mixes

Specimen	w/c ratio	Slump Value(mm)	Compressive strength(N/mm2)	
	0.45	95	7 day	28 day
1			27.08	34.07

Table 1 shows the compressive strength of concrete from the trial mix. The test results indicate good agreement with target compressive strength. Consequently, the same ingredient proportions in the mix design were used for further tests, now including coconut fiber.

(ii) Slump Test:

Table 2: Slump test observation

Coconut fiber %	Trial	Avg. w/c ratio	Slump Value(mm)	Avg. Slump Value(mm)	Remarks
1%	Cube	0.45	95	83.33	Sample prepared for Cube, Cylinder and Beam separately at different days
	Cylinder		80		
	Beam		75		
3%	Cube	0.45	90	78.33	
	Cylinder		75		
	Beam		70		
5%	Cube	0.45	85	73.33	
	Cylinder		70		
	Beam		65		

The slump test is performed as per IS 516. The test results shows that workability of concrete get compromised as the percentage of fiber content increases.

(iii) Bonding Length

Fibers act as bridges within the concrete matrix, enhancing its ability to resist crack propagation by increasing the energy required for a crack to grow. The effectiveness of this bond depends on several factors, including the type of fiber, its surface texture, and its chemical compatibility with the concrete. Ideally, fibers should slip out of the matrix rather than break, as this gradual pull-out mechanism helps dissipate energy and improve the concrete's overall durability. According to IS 456:2000, bond strength is evaluated through pull-out tests, where a fiber is embedded in a concrete specimen and subjected to tensile loading until it is pulled out. In the lab, coconut fibers of various lengths (1.0, 1.5, 2.0, and 2.5 cm) were embedded in the concrete. After 28 days, the fibers were pulled out using a spring balance to determine their non-sleeve length. Table 3 indicates the gripping length of fibers, while Figures 1 and 2 show the preparation of development length and cutting length. (Fig. 1, Fig. 2)

Table 3: Gripping Length observation

Sample	Gripping Length (cm)	Remark
1	1.0	Non-Sleeve
2	1.5	Non-Sleeve
3	2.0	Non-Sleeve
4	2.5	Non-Sleeve

For the preparation of fiber-reinforced concrete, a development length of 1.5 cm was selected, and consequently, a cutting length of 3 cm was used for the laboratory test.

Fig.1: Grip Length

Fig.2: Coconut Fiber Cutting Length

(iv) Compressive Strength Test of Cubes

Fig.3: Photo Compressive Strength Test

Coconut fiber was added to concrete in varying amounts (1%, 3%, and 5% by weight of cement) at a water-cement ratio of 0.45 for compressive strength testing (Fig. 3). It was observed that traditional concrete (without fiber) has comparatively lower compressive strength than fiber-reinforced concrete. As the percentage of fiber increases, the compressive strength decreases. However, the maximum compressive strength was found at 3% coconut fiber content, which aligns well with previous studies (Ahmad et al., 2022; Naamandadin et al., 2020). Overall, the inclusion of 1% to 5% coconut fiber increases compressive strength compared to normal concrete.

Table 4: CFRC Cubes- Compressive Strength Values

Specimen	% of coconut fiber added	Compressive strength (N/mm2)	
		7 day	28 day
1	0%	27.08	34.07
2	1%	27.81	36.7
3	3%	29.14	38.5
4	5%	28.9	37.01

(v) Split Tensile Strength Test

Fig.4: Photo Split Tensile Strength Test

Concrete cylinders (diameter: 15 cm, height: 30 cm) were used for split tensile strength testing (Fig. 4). These concrete samples, reinforced with coconut fibers, were cast with varying fiber percentages (1%, 3%, and 5%). Each sample was subjected to a compression testing machine at 7 and 28 days to gather strength data. Table 5 presents the results of the split tensile strength test of CFRC.

Table 5: Split tensile strength for processed CFRC cylinders

Specimen	Percentage of coconut fiber added	Splitting Tensile strength(N/mm2)	
		7 day	28 day
1	1%	3.32	3.98
2	3%	3.55	4.03
3	5%	2.94	3.45

The test indicates that the strength of the reinforced structure increased with the addition of fibers. Notably, the 3% fiber content exhibited slightly higher strength than the 1% and 5% fiber contents, likely due to the optimal amount of coconut fiber and mixing quality. Above the optimal quantity of coconut fiber proper mixing of the concrete could not achieved though strength decrease. These findings are consistent with previous research by Ahmad et al. (2022), Naamandadin et al. (2020), Otunyo and Nyechieo (2017), Zaman and Awang (2009), and Yadav and Singh (2019).

(vi) Flexural Strength Test

Fig.5: Photo Flexural Strength Test

Flexural strength tests were conducted on beams measuring 15 cm x 15 cm x 70 cm (Fig. 7 & 8). Three samples of concrete reinforced with coconut fiber were prepared with varying fiber contents (1%, 3%, and 5%). For CFRC, the strength values at 7 and 28 days were determined using flexural strength test equipment. The results of these tests, with 1%, 3%, and 5% fiber additions, are presented in Table 6.

Table 6: Flexural strength for processed CFRC Beams

Specimen	Percentage of coconut fiber added	Flexural strength (N/mm2)	
		7 days	28 days
1	1%	3.09	3.72
2	3%	3.33	3.85
3	5%	2.94	3.55

Table 6 shows that an increase in fiber content leads to an increase in flexural strength, with the optimal strength observed at 3% fiber content due to the proper ratio and mixing quality. Above the optimal quantity of coconut fiber proper mixing of the concrete could not achieved though strength decrease. This test has been recommended by Sarangi, S., & Sinha, A. (2016) and Ranjitham et al. (2019, July) for evaluating the strength properties of CFRC.

4. CONCLUSION

As an organic waste material, coconut fiber offers potential as a concrete reinforcement material, aligning well with sustainability principles. This study investigates the strength of coconut fiber-reinforced concrete using fibers of predefined lengths. A mix design was performed to determine the ratios of ingredients (cement, sand, aggregate, water, and additional admixtures). It was found that the inclusion of coconut fiber reduced workability, as indicated by moderate slump values for cubes, cylinders, and beams. Testing various gripping lengths of coconut fibers (1 cm, 1.5 cm, 2.0 cm, and 2.5 cm) on 5 cm cubes revealed that while a 1 cm gripping length could suffice, a 1.5 cm length was chosen for safe bonding. The experiments showed that a maximum of 3% coconut fiber content in concrete provided adequate compressive strength. Although there was no significant difference in split tensile strength between 1% and 3% fiber content, the 3% fiber content produced slightly higher split tensile strength. The flexural strength values also confirmed similar results. Thus, this study finds that 3% processed coconut fiber by weight of cement is the optimal content to enhance both compressive and flexural strength of concrete, while 1% and 5% fiber content also improve the strength of concrete compared to normal concrete.

REFERENCES

Ali, M. (2014). Seismic performance of coconut-fibre-reinforced-concrete columns with different reinforcement configurations of coconut-fibre ropes. *Construction and Building Materials*, 70, 226-230. DOI: 10.1016/j.conbuildmat.2014.07.086

Ali, M. (2016). Use of coconut fibre reinforced concrete and coconut-fibre ropes for seismic-resistant construction. *Materiales de construccion*, 66(321), e073-e073. DOI: 10.3989/mc.2016.01015

Ahmad, W., Farooq, S. H., Usman, M., Khan, M., Ahmad, A., Aslam, F., ... & Sufian, M. (2020). Effect of coconut fiber length and content on properties of high strength concrete. *Materials*, 13(5), 1075. DOI: 10.3390/ma13051075 PMID: 32121125 PMCID: PMC7084858

Agrawal, R. A., Dhase, S. S., & Agrawal, K. S. (2014). Coconut fiber in concrete to enhance its strength and making lightweight concrete. *International Journal of Engineering Research and Development*, 9(8), 64-67

Adeyemi, A. Y. (1998). An investigation into the suitability of coconut shells as aggregates in concrete production. Journal of Environment Design and Management, 1(1-2), 17-26.

Ahmad,J.,Majdi,A.,Al-Fakih,A.,Deifalla,A.F.,Althoey, F., El Ouni, M. H., & El-Shorbagy, M. A. (2022). Mechanical and durability performance of coconut fiber reinforced concrete: a state-of-the-art review. *Materials*, 15(10), 3601. DOI: 10.3390/ma15103601 PMID: 35629628 PMCID: PMC9143988

PATIL, D. (2021). Effects of coconut fibers on mechanical properties of concrete. *International Journal of Innovations in Engineering and Science*, 6(3), 1-5. DOI: 10.46335/IJIES.2021.6.3.1

Khan, M. I., Abbas, Y. M., & Fares, G. (2017). Review of high and ultrahigh performance cementitious composites incorporating various combinations of fibers and ultrafines. Journal of King Saud University-Engineering Sciences, 29(4), 339-347. DOI: 10.1016/j.jksues.2017.03.006

Kirandeep c, K. (2023). Potency of Concrete by Utilizing Coconut Fiber to Improve Strength of Concrete. *International Journal of Innovative Research in Engineering & Management*, 10(3), 82-85.

Le, T. T., Austin, S. A., Lim, S., Buswell, R. A., Gibb, A. G., & Thorpe, T. (2012). Mix design and fresh properties for high-performance printing concrete. *Materials and structures*, 45, 1221- 1232. DOI: 10.1617/s11527-012-9828-z

Martinelli, F. R. B., Ribeiro, F. R. C., Marvila, M. T., Monteiro, S. N., Filho, F. D. C. G., & Azevedo, A. R. G. D. (2023). A review of the use of coconut fiber in cement composites. *Polymers*, 15(5), 1309. DOI: 10.3390/polym15051309 PMID: 36904550 PMCID: PMC10007414

Mudiyono, R., & Sudarno, S. (2019). The Influence of Coconut Fiber on the Compressive and Flexural Strength of Paving Blocks. *Engineering, Technology & Applied Science Research*, 9(5), 4702-4705. DOI: 10.48084/etasr.3008

Nor, M. J. M., Ayub, M., Zulkifli, R., Amin, N., & Fouladi, M. H. (2010). Effect of different factors on the acoustic absorption of coir fiber. DOI: 10.3923/jas.2010.2887.2892

Naamandadin, N. A., Rosdi, M. S., Mustafa, W. A., Aman, M. N. S. S., & Saidi, S. A. (2020, September). Mechanical behaviour on concrete of coconut coir fiber as additive. In *IOP Conference Series: Materials Science and Engineering* (Vol. 932, No. 1, p. 012098). IOP Publishing.) DOI: 10.1088/1757-899X/932/1/012098

Olanipekun, E. A., Olusola, K. O., & Ata, O. (2006). A comparative study of concrete properties using coconut shell and palm kernel shell as coarse aggregates. Building and environment, 41(3), 297-301. DOI: 10.1016/j.buildenv.2005.01.029

Otunyo, A. W., & Nyechieo, N. D. (2017). Mechanical properties and fracture behaviour of coconut fibre reinforced concrete (CFRC). *American Journal of Civil Engineering and Architecture*, 5(5), 208-216. DOI: 10.12691/ajcea-5-5-5

Ranjitham, M., Mohanraj, S., Ajithpandi, K., Akileswaran, S., & Sree, S. K. (2019, July). Strength properties of coconut fibre reinforced concrete. In *AIP Conference Proceedings* (Vol. 2128, No. 1). AIP Publishing. DOI: 10.1063/1.5117917

Rumbayan, R., Sudarno & Ticoalu, A. (2019). A study into flexural, compressive and tensile strength of coir-concrete as sustainable building material, MATEC Web of Conferences 258, 010 DOI:10.1051/matecconf/201925801011

Rabma, S., Narksitipan, S., & Jaitanong, N.(2020). Coconut fiber reinforced cement-based composites. *Solid State Phenomena*, 302, 101-106. DOI: 10.4028/www.scientific.net/SSP.302.101

Sarangi, S., & Sinha, A. (2016). Mechanical properties of hybrid fiber reinforced concrete. *Indian Journal of Science and Technology*, 9(30), 1. DOI: 10.17485/ijst/2016/v9i30/99234

Thomas, J., & Ramaswamy, A. (2007). Mechanical properties of steel fiber-reinforced concrete. *Journal of materials in civil engineering*, 19(5), 385-392. DOI: 10.1061/(ASCE)0899-1561(2007)19:5(385)

Tastani, S. P., & Pantazopoulou, S. J. (2013). Reinforcement and concrete bond: State determination along the development length. *Journal of Structural Engineering*, 139(9), 1567-1581. DOI: 10.1061/(ASCE)ST.1943-541X.0000725

Yalley, P. P., & Kwan, A. S. K. (2009). Use of coconut fibre as an enhancement of concrete. *Journal of Engineering and Technology*, 3, 54-73.

Yadav, S. K., & Singh, A. (2019). An experimental study on coconut fiber reinforced concrete. *Int. Res. J. Eng. Technol*, 6, 2250-2254.

Yan, L., Chouw, N., Huang, L., & Kasal, B. (2016). Effect of alkali treatment on microstructure and mechanical properties of coir fibres, coir fibre reinforced-polymer composites and reinforced-cementitious composites. Construction and Building Materials, 112, 168-182. DOI: 10.1016/j.conbuildmat.2016.02.182

Zain, M. F. M., Abd, S. M., Hamid, R., & Jamil, M. (2010). Potential for utilising concrete mix properties to predict strength at different ages. Journal of Applied Sciences (Faisalabad), 10(22), 2831-2838. DOI: 10.3923/jas.2010.2831.2838

Zaman, I., & Awang, M. K. (2009). Influence of fiber volume fraction on the tensile properties and dynamic characteristics of coconut fiber reinforced composite. *Journal of Science and Technology, 1*(1).

Cytoscape A Tool to Visualize Protein-Protein interactions using Eugenol, a Phytochemical of *Ocimum sanctum* L

Vanitha Surender[1*] and Tanushree Sharma[1]

[1] Department of Biochemistry, Bhavan's Vivekananda College of Science, Humanities and Commerce, Secunderabad 500094

***CORRESPONDING AUTHOR:**

Vanitha Surender

Email:vanitha.biochem@bhavansvc.ac.in

ISSN : 2382-5359(Online), 1994-1412(Print)

DOI:
https://doi.org/10.3126/njst.v22i2.78602

Date of Submission: 8 Feb, 2023

Date of Acceptance: 2 Jun, 2024

ABSTRACT

Eugenol (4-hydroxy-3-methoxy-allylbenzene) is an important bioactive compound found in various medicinal plants and has been extensively investigated for its pharmacological properties. Apart from its anaesthetic and analgesic properties, this phenolic compound has antimicrobial, anti-inflammatory, anticancer and antioxidant properties. One of the promising candidates with versatile applications in designing new drugs will be Eugenol for its pharmacological effects. While the metabolism and pharmacokinetics of Eugenol have been studied in humans, still there is lack of data available on its precise mode of action and its impact on system level protein networks. To identify the action of Eugenol on protein interaction network, an interactome was constructed using STRING and Cytoscape tools, based on 98 key proteins extracted from PubMed literatures. Swiss Target Prediction was used to predict the possible macromolecular targets in humans. It was predicted that the target classes included 20% enzymes, secreted protein, and Family A G- protein coupled receptors, 13.3% of Ligand-gated ion channel and 6.7% of kinase, eraser, lyase and oxidoreductases. Further, using the Cytoscape 3.9.1 version *in-silico* study, it could be observed that 92 nodes in total were connected with 61 edges with a clustering coefficient of 0.369. Using a phytochemical Eugenol, the possible network analysis has been predicted. Evaluating the network among the other phytochemicals of *Ocimum sanctum* could help us to investigate the role played by these key phytochemicals at gene and molecular level and can help us explore their interference in disease patterns in humans.

Keywords: *Cytoscape 3.9.1 version, Edges, Nodes, String database*

1. INTRODUCTION

From ancient times medicinal plants have been used to fight different types of diseases (Petrovska 2012). To manage diseases, bioactive compounds derived naturally has wide potential in medicinal and also as therapeutic agents. To maintain a balance within the cell, certain important phytochemicals present in the medicinal plants act as multiple protein targets (Ding et al. 2009). Eugenol is an example of a phytochemical present in the leaves of *Ocimum sanctum*. The molecule's extensive *in vitro* and *in vivo* reports as a therapeutic agent, and the lack of experimental data on its interactions with proteins, make it a compelling study target (Huang et al. 2018).

Modern molecular biology requires biologists to focus on biomolecular components, such as Eugenol, and their interaction with other proteins via a complex web system in a living cell (Hartwell et al. 1999). Protein-protein interactions (PPIs) are the most common type of macromolecular interaction in a living system. PPIs are dynamic in nature and adjust according to the varying stimuli and environmental conditions. Eugenol has been reported to interact with various proteins to alter their function. For instance, Eugenol increases Vitamin D3 upregulated protein 1 (VDUPI) and IκBα levels in the NF-κB pathway, displaying anti-asthmatic effect (Pan and Dong, 2015).

To study these complex proteome networks, graph theory and advanced system biology approaches are employed by researchers. System biology, as an interdisciplinary field, can bridge the gap between *in vitro* and *in vivo* models through the data procured from *omics* and reveal the function of biological micro and macromolecules present in any biological model (Koutsogiannouli et al. 2013). With the currently available *in-silico* tools, screening and analyzing the network via pharmacological aspects of natural plant products like phytochemicals can be performed to understand the multi-targeted action of plant metabolites, to create a protein network system (Chandran et al. 2017).

Cytoscape version 3.9.1 was developed to understand the interactions among proteins at molecular level and create a profile of networks that can be used to visualize all possible molecular interactions within the networks (Shannon et al. 2003, Smoot et al. 2010). Developing networks reduces the complexity in data, is more efficient than table interpretations, and data integration can be done at optimal level with attractive visualization features. Biological Network Taxonomy can be categorized into metabolic, signalling and regulatory pathways and diseases.

Constructing the PINs (Protein Interaction Networks) of Eugenol involved screening the phytochemical compound from PubChem database and saving the structure as its SMILES notation. A network can be created to predict the interactions between phytochemicals and proteins, protein targets, and enriched pathways using the Swiss Target Prediction tool. This allows us to predict the protein-protein interactions with which a downstream analysis can be performed. Using String database, the data related to phytochemical interaction with proteins present in humans can be exported to Cytoscape tool to analyze, visualize, and interpret the outcome. These networks can be sorted based on organelles, tissues, text mining of the data, clustering coefficients, neighbourhood's, in betweenness, number of nodes and edges, etc. With the available output, the major proteins involved in interactions can be shortlisted about eugenol.

2. MATERIALS AND METHODS

The workflow includes the use of following tools,

- Retrieve the phytochemical structure and SMILES notation from PubChem database. https://pubchem.ncbi.nlm.nih.gov/
- Screening the probable macromolecular targets of small molecules assumed as bioactive using Swiss Target Prediction version 11.5. It predicts both the two- and three-dimensional (2D and 3D) similarity among the 3,70,000 libraries of known actives of nearly 3,000 different proteins available on three different animal species. http://swisstargetprediction.ch/
- Screening for the protein-protein interactions using string database. https://string-db.org/
- Building networks using Cytoscape network tool 3.9.1 version.
- Analyse and interpret the data

2.1. Protein-Protein Interaction Network Construction and Visualization

The SMILES notation for Eugenol was submitted to the online Swiss Target Prediction tool, and a set of

target proteins were obtained for *Homo sapiens*. The retrieved data was saved as an .csv file. The excel sheet obtained contained the set of proteins with target, common name, ChEMBL ID code, Uniport ID, Target class, known active 2D and 3D from Swiss Target Prediction (Fig. 1).

The common names of all possible protein targets were submitted into the string database (version 11.5), a tool used to predict all possible protein-protein interactions. Selecting the multiple proteins and feeding their common names into string database gave a visual output network with all possible interactions (Fig. 3). The obtained results were retrieved and stored in an .csv format. From the obtained Functional Enrichment data, KEGG pathway output was selected and exported to Cytoscape tool for further analysis.

2.2. Protein Interaction Network Analysis

The interaction network in Cytoscape was analyzed using its inbuilt Network Analyzer plugin, which gave the primary topological framework of Eugenol-rewired PINs, like clustering coefficient, network density, network heterogeneity, network centralization, and connected components. MCODE plug-in of Cytoscape was applied for modulation of the network (finding highly interconnected regions or clusters in the network). Clusters in PINs are often metabolic pathways and protein complexes (Bader and Hogue 2003). Cytoscape scored each module based on density and size, incase if the output is with higher score probably it indicates a possible tighter module.

3. RESULTS AND DISCUSSION

3.1. Retrieving Target Proteins

To retrieve the SMILES notation of Eugenol [COC1=C(C=CC(=C1)CC=C)] interaction with proteins in *Homo sapiens* PubChem online portal was exercised. 101 possible protein targets were retrieved by submitting the SMILES notation in the online Swiss Target Prediction Tool (TABLE 1). Out of these targets 20% belonged to Family A G-protein coupled receptor, enzymes, and secreted proteins each, while 6.7 % were Erasers, oxidoreductases, lyases, and kinases. Ligand-gated ion channels covered the remaining 13.3% of targets (Fig. 2).

3.2. Network Construction in STRING

STRING database was used to generate the PINs rewired by Eugenol by inputting the common names of targets retrieved from Swiss Target Prediction Tool. The 98 nodes or proteins in the network output (Fig. 4) covered 81 different GO molecular functions, 124 KEGG pathways, 414 interactions (physical or functional). The network statistics indicated an average node degree, local clustering coefficient of 7.67 and 0.583 respectively with a PPI enrichment p-value $<1.0e^{-16}$ (Table 2 & 3).

3.3. Topology and Network Modulation in Cytoscape

The Protein Interaction Network of an intricate cellular system can be studied through its topology, which can reveal the connections and interactions of biological macromolecules in various pathways that is metabolic and cellular in nature (Ba et al. 2015). This study was focused on, understanding the gene/protein connection pathways that was altered by Eugenol, and Cytoscape's Network Analyser plug-in was applied for topological analysis (Fig. 5) (Table 4).

The shortest path length for a Protein Interaction Network shows the number of edges through the shortest paths between two nodes. On the other hand, closeness centrality is the inverse of the average shortest path. These parameters outline the ability to transport information and the comprehensive navigability of the interactome (Ba *et al.* 2015, Delprato 2012). The characteristic pathlength for Eugenol-rewired PIN was 2.809 (Fig. 6).

Clustering coefficient tells us how close the nodes are to their neighbours and the hierarchical modularity of the PIN. It is used to identify the potential functional modules and unwrap the complexity in molecular and signalling pathways in the network (Bader and Hogue 2003, Ba et al. 2015, Barabási and Oltvai 2004). For the current PIN generated with Eugenol, 0.369 was found to be the clustering coefficient distribution (Fig. 7). Plug-in MCODE was used to work out 5 modules from the KEGG PIN rewired by Eugenol (Fig. 8).

4. CONCLUSION

With a simple workflow, Cytoscape tool was used to predict and understand the number of protein- protein interactions possible within the selected phytochemical Eugenol. This visual network data output was in terms of subcellular locations and pharmacokinetic data. From the above study it was observed that, the KEGG enriched PIN has 92 nodes with 61 edges

and a clustering coefficient of 0.369 (TABLE 4). Eugenol, has been recognized as a safe food additive under food substance category by Federal Food, Drug and Cosmetic administration as it could work synergistically with various antimicrobial compounds present in foods. Further, researchers are designing and developing eugenol structure-based derivatives predicting to have different structural and biological properties. While the current study only focused on one phytochemical (Eugenol), protein network analysis of other phytochemicals can help us understand the role played by them at gene and molecular level. They can also provide an insight into their interference in disease patterns in human.

5. TABLES AND FIGURES

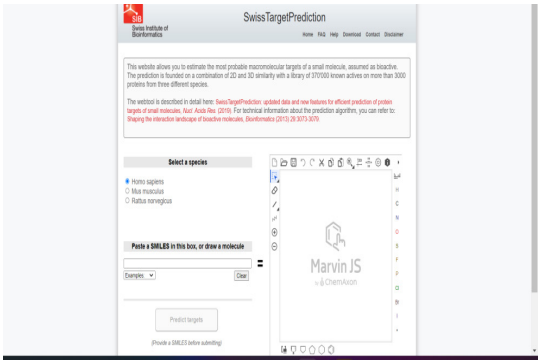

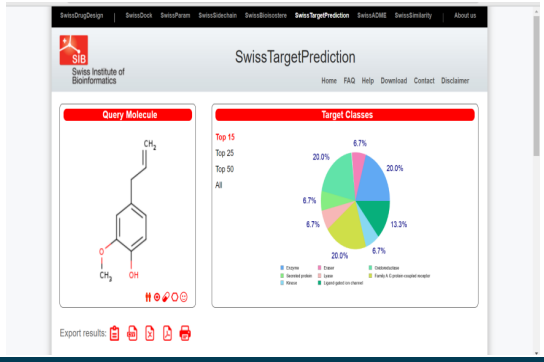

Fig.1: Swiss Target Prediction Tool Input and Output

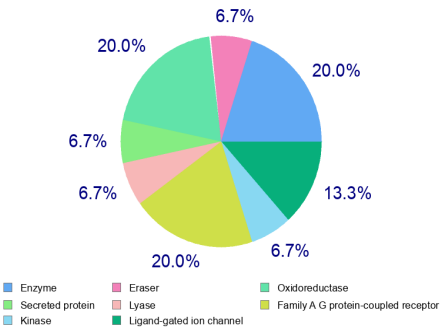

Fig.2: Target Classes of Eugenol

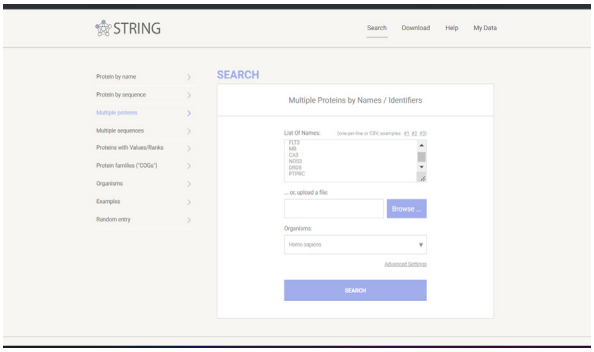

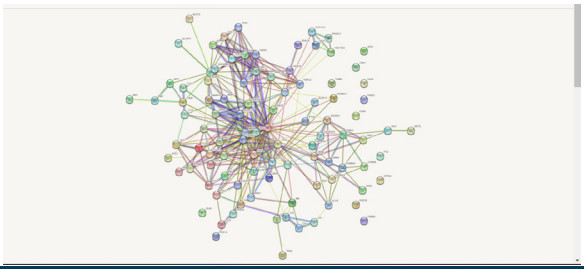

Fig.3: STRING Database Input and Output. Potential protein targets of Eugenol were retrieved from Swiss Target Prediction Tool and were entered in the STRING prompt, specific for Humans (left). The output displayed a complex interactome among the proteins retrieved (right).

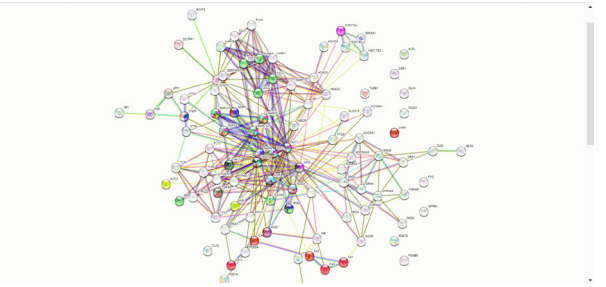

Fig.4: Protein Interaction Network (PIN in STRING). The PIN generated in STRING displays all the possible interactions among the potential protein targets for Eugenol

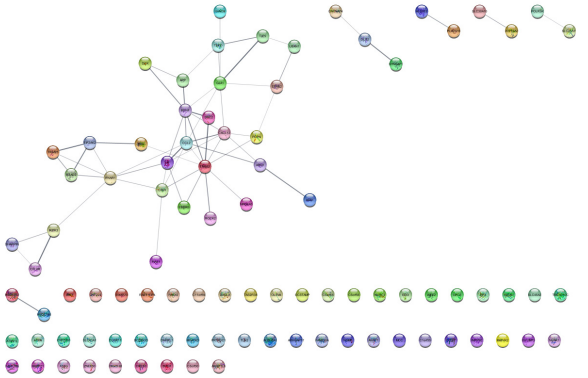

Fig.5: KEGG Enriched PIN in Cytoscape. The above PIN displays interactions between potential Eugenol targets that are found in various KEGG pathways

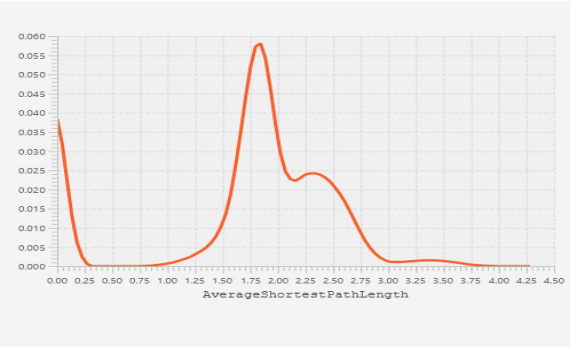

Fig. 6: Characteristic Pathlength is 2.809. Histogram generated by Cytoscape Network Analyzer. The y-axis represents the frequency of the average shortest path lengths found in the interaction network.

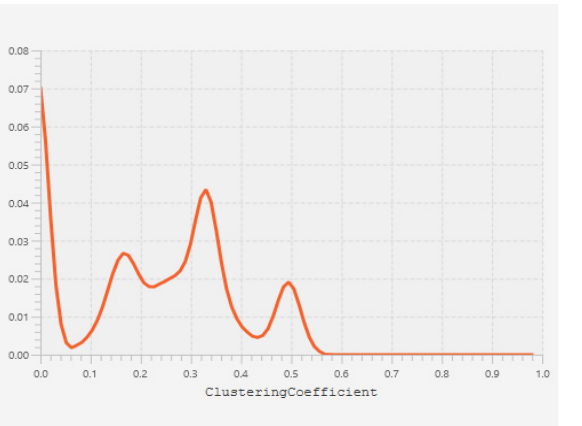

Fig.7: Clustering coefficient distribution is 0.369. Histogram generated by Cytoscape Network Analyzer. The y-axis represents the average clustering coefficient.

Fig.8: Cluster modules obtained through MCODE. The five clusters found may represent functionally homogenous sub-networks of proteins within the large PIN, based on their densely interconnected nodes.

Table 1: Possible protein targets for Eugenol obtained from Swiss Target Prediction tool

Target	Common name	Uniprot ID	ChEMBL ID	Target Class	Probability* Probability for the query molecule - assumed as bioactive - to have this protein as target.
Fatty acid desaturase 1	FADS1	O60427	CHEMBL5840	Enzyme	0.133391
Histone deacetylase 6	HDAC6	Q9UBN7	CHEMBL1865	Eraser	0.133391
Egl nine homolog 1	EGLN1	Q9GZT9	CHEMBL5697	Oxidoreductase	0.125076
Vascular endothelial growth factor A	VEGFA	P15692	CHEMBL1783	Secreted protein	0.125076
Carbonic anhydrase II	CA2	P00918	CHEMBL205	Lyase	0.125076
G-protein coupled receptor 84	GPR84	Q9NQS5	CHEMBL3714079	Family A G protein-coupled receptor	0.125076
Cyclooxygenase-1	PTGS1	P23219	CHEMBL221	Oxidoreductase	0.125076
D-amino-acid oxidase	DAO	P14920	CHEMBL5485	Enzyme	0.125076
Poly [ADP-ribose] polymerase-1	PARP1	P09874	CHEMBL3105	Enzyme	0.125076
Tyrosine-protein kinase SRC	SRC	P12931	CHEMBL267	Kinase	0.125076
Adenosine A1 receptor	ADORA1	P30542	CHEMBL226	Family A G protein-coupled receptor	0.125076
Adenosine A2a receptor	ADORA2A	P29274	CHEMBL251	Family A G protein-coupled receptor	0.125076
Steroid 5-alpha-reductase 1	SRD5A1	P18405	CHEMBL1787	Oxidoreductase	0.125076
Neuronal acetylcholine receptor subunit alpha-3	CHRNA3	P32297	CHEMBL3068	Ligand-gated ion channel	0.125076
Neuronal acetylcholine receptor protein alpha-4 subunit (by homology)	CHRNA4	P43681	CHEMBL1882	Ligand-gated ion channel	0.125076
Interleukin-8 receptor B	CXCR2	P25025	CHEMBL2434	Family A G protein-coupled receptor	0.125076
dCTP pyrophosphatase 1	DCTPP1	Q9H773	CHEMBL3769292	Enzyme	0.125076
Alkaline phosphatase, tissue-nonspecific isozyme	ALPL	P05186	CHEMBL5979	Enzyme	0.125076
Methionine aminopeptidase 2	METAP2	P50579	CHEMBL3922	Protease	0.116739
Carbonyl reductase [NADPH] 1	CBR1	P16152	CHEMBL5586	Enzyme	0.116739
Calcium-activated potassium channel subunit alpha-1	KCNMA1	Q12791	CHEMBL4304	Voltage-gated ion channel	0.116739
Arachidonate 15-lipoxygenase	ALOX15	P16050	CHEMBL2903	Enzyme	0.116739

Neuronal acetylcholine receptor; alpha3/beta4	CHRNA3 CHRNB4	P32297 P30926	CHEMBL1907594	Ligand-gated ion channel	0.116739
Vascular endothelial growth factor receptor 2	KDR	P35968	CHEMBL279	Kinase	0.116739
Histone deacetylase 8	HDAC8	Q9BY41	CHEMBL3192	Eraser	0.116739
Androgen Receptor	AR	P10275	CHEMBL1871	Nuclear receptor	0.116739
Proteasome Macropain subunit MB1	PSMB5	P28074	CHEMBL4662	Protease	0.116739
Tryptophan 2,3-dioxygenase (by homology)	TDO2	P48775	CHEMBL2140	Enzyme	0.116739
Neuronal acetylcholine receptor; alpha4/beta2	CHRNA4 CHRNB2	P43681 P17787	CHEMBL1907589	Ligand-gated ion channel	0.116739
Estradiol 17-beta-dehydrogenase 3	HSD17B3	P37058	CHEMBL4234	Enzyme	0.116739
Cytochrome P450 17A1 (by homology)	CYP17A1	P05093	CHEMBL3522	Cytochrome P450	0.116739
Serine/threonine-protein kinase Aurora-A	AURKA	O14965	CHEMBL4722	Kinase	0.116739
Metabotropic glutamate receptor 5	GRM5	P41594	CHEMBL3227	Family C G protein-coupled receptor	0
Transthyretin	TTR	P02766	CHEMBL3194	Secreted protein	0
Estradiol 17-beta-dehydrogenase 2	HSD17B2	P37059	CHEMBL2789	Enzyme	0
Dopamine D2 receptor	DRD2	P14416	CHEMBL217	Family A G protein-coupled receptor	0
Hematopoietic cell protein-tyrosine phosphatase 70Z-PEP	PTPN22	Q9Y2R2	CHEMBL2889	Phosphatase	0
Toll-like receptor (TLR7/TLR9)	TLR9	Q9NR96	CHEMBL5804	Toll-like and Il-1 receptors	0
Tubulin beta-1 chain	TUBB1	Q9H4B7	CHEMBL1915	Structural protein	0
Tyrosine-protein kinase JAK1	JAK1	P23458	CHEMBL2835	Kinase	0
Tyrosine-protein kinase JAK2	JAK2	O60674	CHEMBL2971	Kinase	0
Tyrosine-protein kinase TYK2	TYK2	P29597	CHEMBL3553	Kinase	0
Serine/threonine-protein kinase B-raf	BRAF	P15056	CHEMBL5145	Kinase	0
Thymidylate synthase	TYMS	P04818	CHEMBL1952	Transferase	0
Uridine phosphorylase 1 (by homology)	UPP1	Q16831	CHEMBL4811	Enzyme	0
Mannose-6-phosphate isomerase	MPI	P34949	CHEMBL2758	Isomerase	0
Dual specificity protein phosphatase 3	DUSP3	P51452	CHEMBL2635	Phosphatase	0
Phosphodiesterase 7A	PDE7A	Q13946	CHEMBL3012	Phosphodiesterase	0
Fibroblast growth factor receptor 1	FGFR1	P11362	CHEMBL3650	Kinase	0
Carbonic anhydrase VA	CA5A	P35218	CHEMBL4789	Lyase	0
Ribosomal protein S6 kinase alpha 3	RPS6KA3	P51812	CHEMBL2345	Kinase	0

Matrix metalloproteinase 9	MMP9	P14780	CHEMBL321	Protease	0
Nitric-oxide synthase, brain	NOS1	P29475	CHEMBL3568	Enzyme	0
Serine/threonine-protein kinase Chk1	CHEK1	O14757	CHEMBL4630	Kinase	0
Muscarinic acetylcholine receptor M5	CHRM5	P08912	CHEMBL2035	Family A G protein-coupled receptor	0
Cyclin-dependent kinase 2	CDK2	P24941	CHEMBL301	Kinase	0
Thymidine phosphorylase	TYMP	P19971	CHEMBL3106	Enzyme	0
Toll-like receptor (TLR7/ TLR9)	TLR7	Q9NYK1	CHEMBL5936	Toll-like and Il-1 receptors	0
Endothelial PAS domain-containing protein 1	EPAS1	Q99814	CHEMBL1744522	Unclassified protein	0
Matrix metalloproteinase 1	MMP1	P03956	CHEMBL332	Protease	0
Phosphodiesterase 5A	PDE5A	O76074	CHEMBL1827	Phosphodiesterase	0
c-Jun N-terminal kinase 1	MAPK8	P45983	CHEMBL2276	Kinase	0
c-Jun N-terminal kinase 3	MAPK10	P53779	CHEMBL2637	Kinase	0
c-Jun N-terminal kinase 2	MAPK9	P45984	CHEMBL4179	Kinase	0
Thrombin	F2	P00734	CHEMBL204	Protease	0
Serine/threonine-protein kinase AKT	AKT1	P31749	CHEMBL4282	Kinase	0
Dual specificity phosphatase Cdc25B	CDC25B	P30305	CHEMBL4804	Phosphatase	0
Carbonic anhydrase I	CA1	P00915	CHEMBL261	Lyase	0
Carbonic anhydrase XII	CA12	O43570	CHEMBL3242	Lyase	0
Carbonic anhydrase IX	CA9	Q16790	CHEMBL3594	Lyase	0
Serine/threonine-protein kinase PLK4	PLK4	O00444	CHEMBL3788	Kinase	0
Dual specificity protein kinase CLK4	CLK4	Q9HAZ1	CHEMBL4203	Kinase	0
Dual specificity protein kinase CLK2	CLK2	P49760	CHEMBL4225	Kinase	0
Amine oxidase, copper containing	AOC3	Q16853	CHEMBL3437	Enzyme	0
P-glycoprotein 1	ABCB1	P08183	CHEMBL4302	Primary active transporter	0
Histone deacetylase 2	HDAC2	Q92769	CHEMBL1937	Eraser	0
TGF-beta receptor type I	TGFBR1	P36897	CHEMBL4439	Kinase	0
MAP kinase p38 alpha	MAPK14	Q16539	CHEMBL260	Kinase	0
Metabotropic glutamate receptor 4	GRM4	Q14833	CHEMBL2736	Family C G protein-coupled receptor	0
Transmembrane domain-containing protein TMIGD3	TMIGD3	P0DMS9	CHEMBL3712907	Unclassified protein	0
Acetylcholinesterase	ACHE	P22303	CHEMBL220	Hydrolase	0
Macrophage migration inhibitory factor	MIF	P14174	CHEMBL2085	Enzyme	0

Dopamine D1 receptor	DRD1	P21728	CHEMBL2056	Family A G protein-coupled receptor	0
Branched-chain-amino-acid aminotransferase, mitochondrial	BCAT2	O15382	CHEMBL3616354	Transferase	0
Serine/threonine-protein kinase Aurora-B	AURKB	Q96GD4	CHEMBL2185	Kinase	0
Cyclin-dependent kinase 1	CDK1	P06493	CHEMBL308	Kinase	0
Collagen-binding protein 1	SERPINH1	P50454	CHEMBL5286	Other cytosolic protein	0
Cathepsin (V and K)	CTSV	O60911	CHEMBL3272	Protease	0
Cathepsin L	CTSL	P07711	CHEMBL3837	Protease	0
CDC7/DBF4 (Cell division cycle 7-related protein kinase/ Activator of S phase kinase)	CDC7	O00311	CHEMBL5443	Kinase	0
Phosphodiesterase 7B	PDE7B	Q9NP56	CHEMBL4716	Phosphodiesterase	0
Alpha-ketoglutarate-dependent dioxygenase FTO	FTO	Q9C0B1	CHEMBL2331065	Oxidoreductase	0
Purine nucleoside phosphorylase	PNP	P00491	CHEMBL4338	Enzyme	0
Dopamine D4 receptor	DRD4	P21917	CHEMBL219	Family A G protein-coupled receptor	0
Tyrosine-protein kinase receptor FLT3	FLT3	P36888	CHEMBL1974	Kinase	0
Myoglobin	MB	P02144	CHEMBL2406892	Unclassified protein	0
Carbonic anhydrase III	CA3	P07451	CHEMBL2885	Lyase	0
Nitric-oxide synthase, endothelial	NOS3	P29474	CHEMBL4803	Enzyme	0
Dopamine D5 receptor	DRD5	P21918	CHEMBL1850	Family A G protein-coupled receptor	0
Leukocyte common antigen	PTPRC	P08575	CHEMBL3243	Enzyme	0

Table 2: Network statistics of PIN from STRING

Network Statistics	Results
Number of Nodes	98
Number of Edges	365
Average Node Degree	7.24
Average local clustering coefficient	0.559
Expected Number of Edges	161
PPI Enrichment p-value	$<1.0e^{-16}$

Table 3: KEGG functional enrichment output from STRING

Pathway	Description	Count in network	Strength	False discovery in data
hsa00910	Nitrogen metabolism	6 of 17	1.86	4.58E-08
hsa05219	Bladder cancer	6 of 41	1.47	1.87E-06
hsa04914	Progesterone-mediated oocyte maturation	11 of 94	1.38	8.03E-10
hsa00360	Phenylalanine metabolism	2 of 17	1.38	0.0127
hsa04917	Prolactin signaling pathway	8 of 69	1.37	1.29E-07
hsa05212	Pancreatic cancer	8 of 73	1.35	1.76E-07
hsa04370	VEGF signaling pathway	6 of 57	1.33	8.11E-06
hsa04215	Apoptosis - multiple species	3 of 30	1.31	0.0024
hsa00220	Arginine biosynthesis	2 of 21	1.29	0.0169
hsa04926	Relaxin signaling pathway	12 of 128	1.28	8.03E-10
hsa04933	AGE-RAGE signaling pathway in diabetic complications	9 of 98	1.27	9.71E-08
hsa01521	EGFR tyrosine kinase inhibitor resistance	7 of 78	1.26	2.93E-06
hsa05120	Epithelial cell signaling in Helicobacter pylori infection	6 of 67	1.26	1.54E-05
hsa00240	Pyrimidine metabolism	5 of 56	1.26	8.59E-05
hsa05418	Fluid shear stress and atherosclerosis	11 of 130	1.24	6.13E-09
hsa01522	Endocrine resistance	8 of 95	1.23	9.37E-07
hsa05161	Hepatitis B	13 of 159	1.22	8.03E-10
hsa04659	Th17 cell differentiation	8 of 101	1.21	1.20E-06
hsa04658	Th1 and Th2 cell differentiation	7 of 87	1.21	5.16E-06
hsa00790	Folate biosynthesis	2 of 25	1.21	0.0222
hsa05145	Toxoplasmosis	8 of 105	1.19	1.51E-06
hsa05211	Renal cell carcinoma	5 of 66	1.19	0.00015
hsa04664	Fc epsilon RI signaling pathway	5 of 66	1.19	0.00015
hsa05210	Colorectal cancer	6 of 82	1.17	4.01E-05
hsa04012	ErbB signaling pathway	6 of 83	1.17	4.18E-05
hsa04920	Adipocytokine signaling pathway	5 of 69	1.17	0.00018
hsa04728	Dopaminergic synapse	9 of 128	1.16	6.06E-07
hsa04068	FoxO signaling pathway	9 of 127	1.16	6.06E-07
hsa05142	Chagas disease	7 of 99	1.16	1.01E-05
hsa04620	Toll-like receptor signaling pathway	7 of 101	1.15	1.07E-05
hsa04540	Gap junction	6 of 87	1.15	5.13E-05
hsa00140	Steroid hormone biosynthesis	4 of 59	1.14	0.0012
hsa04380	Osteoclast differentiation	8 of 122	1.13	3.35E-06
hsa05162	Measles	9 of 138	1.12	9.53E-07
hsa04657	IL-17 signaling pathway	6 of 92	1.12	6.63E-05

hsa04930	Type II diabetes mellitus	3 of 46	1.12	0.0062
hsa05215	Prostate cancer	6 of 96	1.11	7.97E-05
hsa04137	Mitophagy - animal	4 of 63	1.11	0.0015
hsa04722	Neurotrophin signaling pathway	7 of 114	1.1	2.10E-05
hsa04071	Sphingolipid signaling pathway	7 of 116	1.09	2.28E-05
hsa04660	T cell receptor signaling pathway	6 of 101	1.08	9.64E-05
hsa04625	C-type lectin receptor signaling pathway	6 of 102	1.08	9.96E-05
hsa04622	RIG-I-like receptor signaling pathway	4 of 70	1.07	0.0021
hsa00350	Tyrosine metabolism	2 of 35	1.07	0.0394
hsa05135	Yersinia infection	7 of 125	1.06	3.55E-05
hsa04931	Insulin resistance	6 of 107	1.06	0.00013
hsa05235	PD-L1 expression and PD-1 checkpoint pathway in cancer	5 of 88	1.06	0.00046
hsa04912	GnRH signaling pathway	5 of 89	1.06	0.00047
hsa04725	Cholinergic synapse	6 of 110	1.05	0.00014
hsa04923	Regulation of lipolysis in adipocytes	3 of 54	1.05	0.0093
hsa05167	Kaposi sarcoma-associated herpesvirus infection	10 of 187	1.04	9.53E-07
hsa05152	Tuberculosis	9 of 168	1.04	3.06E-06
hsa04217	Necroptosis	8 of 149	1.04	1.07E-05
hsa04668	TNF signaling pathway	6 of 112	1.04	0.00015
hsa04750	Inflammatory mediator regulation of TRP channels	5 of 94	1.04	0.00059
hsa05220	Chronic myeloid leukemia	4 of 75	1.04	0.0025
hsa05133	Pertussis	4 of 74	1.04	0.0025
hsa04210	Apoptosis	7 of 132	1.03	4.50E-05
hsa04935	Growth hormone synthesis, secretion and action	6 of 118	1.02	0.00019
hsa04114	Oocyte meiosis	6 of 120	1.01	0.0002
hsa04110	Cell cycle	6 of 120	1.01	0.0002
hsa04010	MAPK signaling pathway	14 of 288	1	1.23E-08
hsa05034	Alcoholism	7 of 144	1	7.04E-05
hsa04611	Platelet activation	6 of 122	1	0.00021
hsa00590	Arachidonic acid metabolism	3 of 61	1	0.0127
hsa04024	cAMP signaling pathway	10 of 208	0.99	1.87E-06
hsa05169	Epstein-Barr virus infection	9 of 193	0.98	8.11E-06
hsa04720	Long-term potentiation	3 of 64	0.98	0.0139
hsa05205	Proteoglycans in cancer	9 of 196	0.97	8.68E-06
hsa05221	Acute myeloid leukemia	3 of 66	0.97	0.0147
hsa04015	Rap1 signaling pathway	9 of 202	0.96	1.03E-05
hsa05032	Morphine addiction	4 of 89	0.96	0.0042
hsa04520	Adherens junction	3 of 67	0.96	0.0152
hsa05203	Viral carcinogenesis	8 of 182	0.95	3.82E-05
hsa05230	Central carbon metabolism in cancer	3 of 69	0.95	0.0163

hsa05140	Leishmaniasis	3 of 70	0.94	0.0167
hsa05231	Choline metabolism in cancer	4 of 96	0.93	0.0053
hsa05218	Melanoma	3 of 72	0.93	0.0176
hsa04115	p53 signaling pathway	3 of 72	0.93	0.0176
hsa04510	Focal adhesion	8 of 198	0.92	6.11E-05
hsa04218	Cellular senescence	6 of 150	0.91	0.00056
hsa05166	Human T-cell leukemia virus 1 infection	8 of 211	0.89	8.59E-05
hsa04140	Autophagy - animal	5 of 130	0.89	0.0023
hsa04066	HIF-1 signaling pathway	4 of 106	0.89	0.0073
hsa05130	Pathogenic Escherichia coli infection	7 of 187	0.88	0.00025
hsa04910	Insulin signaling pathway	5 of 133	0.88	0.0025
hsa05017	Spinocerebellar ataxia	5 of 135	0.88	0.0026
hsa05200	Pathways in cancer	19 of 517	0.87	9.25E-10
hsa04080	Neuroactive ligand-receptor interaction	12 of 330	0.87	1.87E-06
hsa04020	Calcium signaling pathway	7 of 193	0.87	0.0003
hsa04014	Ras signaling pathway	8 of 226	0.86	0.00013
hsa04550	Signaling pathways regulating pluripotency of stem cells	5 of 140	0.86	0.003
hsa05323	Rheumatoid arthritis	3 of 85	0.86	0.0259
hsa04621	NOD-like receptor signaling pathway	6 of 174	0.85	0.0012
hsa05226	Gastric cancer	5 of 144	0.85	0.0032
hsa04723	Retrograde endocannabinoid signaling	5 of 145	0.85	0.0033
hsa05170	Human immunodeficiency virus 1 infection	7 of 204	0.84	0.0004
hsa04072	Phospholipase D signaling pathway	5 of 147	0.84	0.0034
hsa05012	Parkinson disease	8 of 240	0.83	0.00017
hsa05132	Salmonella infection	7 of 209	0.83	0.00046
hsa05160	Hepatitis C	5 of 156	0.82	0.0043
hsa00230	Purine metabolism	4 of 127	0.81	0.0128
hsa05206	MicroRNAs in cancer	5 of 160	0.8	0.0048
hsa04022	cGMP-PKG signaling pathway	5 of 162	0.8	0.005
hsa05164	Influenza A	5 of 165	0.79	0.0053
hsa04371	Apelin signaling pathway	4 of 131	0.79	0.0139
hsa04915	Estrogen signaling pathway	4 of 133	0.79	0.0145
hsa05010	Alzheimer disease	10 of 355	0.76	8.59E-05
hsa05163	Human cytomegalovirus infection	6 of 218	0.75	0.0032
hsa05131	Shigellosis	6 of 218	0.75	0.0032
hsa04726	Serotonergic synapse	3 of 108	0.75	0.0475
hsa04062	Chemokine signaling pathway	5 of 186	0.74	0.0084
hsa04932	Non-alcoholic fatty liver disease	4 of 148	0.74	0.0192
hsa04151	PI3K-Akt signaling pathway	9 of 350	0.72	0.00034

hsa04530	Tight junction	4 of 156	0.72	0.0226
hsa04630	JAK-STAT signaling pathway	4 of 160	0.71	0.0244
hsa04810	Regulation of actin cytoskeleton	5 of 209	0.69	0.013
hsa05016	Huntington disease	7 of 298	0.68	0.003
hsa05020	Prion disease	6 of 265	0.66	0.0074
hsa01100	Metabolic pathways	28 of 1447	0.6	1.23E-08
hsa05165	Human papillomavirus infection	6 of 325	0.96	0.0042
hsa04520	Adherens junction	3 of 67	0.96	0.0152
hsa05203	Viral carcinogenesis	8 of 182	0.95	3.82E-05
hsa05230	Central carbon metabolism in cancer	3 of 69	0.95	0.0163
hsa05140	Leishmaniasis	3 of 70	0.94	0.0167
hsa05231	Choline metabolism in cancer	4 of 96	0.93	0.0053
hsa05218	Melanoma	3 of 72	0.93	0.0176
hsa04115	p53 signaling pathway	3 of 72	0.93	0.0176
hsa04510	Focal adhesion	8 of 198	0.92	6.11E-05
hsa04218	Cellular senescence	6 of 150	0.91	0.00056
hsa05166	Human T-cell leukemia virus 1 infection	8 of 211	0.89	8.59E-05
hsa04140	Autophagy - animal	5 of 130	0.89	0.0023
hsa04066	HIF-1 signaling pathway	4 of 106	0.89	0.0073
hsa05130	Pathogenic Escherichia coli infection	7 of 187	0.88	0.00025
hsa04910	Insulin signaling pathway	5 of 133	0.88	0.0025
hsa05017	Spinocerebellar ataxia	5 of 135	0.88	0.0026
hsa05200	Pathways in cancer	19 of 517	0.87	9.25E-10
hsa04080	Neuroactive ligand-receptor interaction	12 of 330	0.87	1.87E-06
hsa04020	Calcium signaling pathway	7 of 193	0.87	0.0003
hsa04014	Ras signaling pathway	8 of 226	0.86	0.00013
hsa04550	Signaling pathways regulating pluripotency of stem cells	5 of 140	0.86	0.003
hsa05323	Rheumatoid arthritis	3 of 85	0.86	0.0259
hsa04621	NOD-like receptor signaling pathway	6 of 174	0.85	0.0012
hsa05226	Gastric cancer	5 of 144	0.85	0.0032
hsa04723	Retrograde endocannabinoid signaling	5 of 145	0.85	0.0033
hsa05170	Human immunodeficiency virus 1 infection	7 of 204	0.84	0.0004
hsa04072	Phospholipase D signaling pathway	5 of 147	0.84	0.0034
hsa05012	Parkinson disease	8 of 240	0.83	0.00017
hsa05132	Salmonella infection	7 of 209	0.83	0.00046
hsa05160	Hepatitis C	5 of 156	0.82	0.0043
hsa00230	Purine metabolism	4 of 127	0.81	0.0128
hsa05206	MicroRNAs in cancer	5 of 160	0.8	0.0048
hsa04022	cGMP-PKG signaling pathway	5 of 162	0.8	0.005
hsa05164	Influenza A	5 of 165	0.79	0.0053

hsa04371	Apelin signaling pathway	4 of 131	0.79	0.0139
hsa04915	Estrogen signaling pathway	4 of 133	0.79	0.0145
hsa05010	Alzheimer disease	10 of 355	0.76	8.59E-05
hsa05163	Human cytomegalovirus infection	6 of 218	0.75	0.0032
hsa05131	Shigellosis	6 of 218	0.75	0.0032
hsa04726	Serotonergic synapse	3 of 108	0.75	0.0475
hsa04062	Chemokine signaling pathway	5 of 186	0.74	0.0084
hsa04932	Non-alcoholic fatty liver disease	4 of 148	0.74	0.0192
hsa04151	PI3K-Akt signaling pathway	9 of 350	0.72	0.00034
hsa04530	Tight junction	4 of 156	0.72	0.0226
hsa04630	JAK-STAT signaling pathway	4 of 160	0.71	0.0244
hsa04810	Regulation of actin cytoskeleton	5 of 209	0.69	0.013
hsa05016	Huntington disease	7 of 298	0.68	0.003
hsa05020	Prion disease	6 of 265	0.66	0.0074
hsa01100	Metabolic pathways	28 of 1447	0.6	1.23E-08
hsa05165	Human papillomavirus infection	6 of 325	0.58	0.017

Table 4: Summary statistics on Eugenol PIN (KEGG enriched) in Cytoscape

Number of Nodes	92
Number of Edges	61
Average number of neighbours	3.667
Network Diameter	6
Network Radius	3
Characteristic path length	2.809
Clustering coefficient	0.369
Network Density	0.126
Network heterogeneity	0.680
Network Centralization	0.234
Connected components	57
Analysis time	0.0032

COPYRIGHT

DECLARATION OF COMPETING INTEREST

The authors declare no conflict of interest.

ACKNOWLEDGEMENT

The authors would like to thank the Management, Principal and Faculty of the Department of Biochemistry, Bhavan's Vivekananda College of Science, Humanities and Commerce, Sainikpuri, Secunderabad, for their support.

REFERENCES

Ba, Q., Li, J., Huang, C., Li, J., Chu, R., Wu, Y., Wang, H., 2015. Topological, functional, and dynamic properties of the protein interaction networks rewired by benzo(a)pyrene. *Toxicology and Applied Pharmacology* 283(2):83-91.
DOI: 10.1016/j.taap.2015.01.006
PMID: 25596431

Bader, G.D., Hogue, C.W., 2003. An automated method for finding molecular complexes in large protein interaction networks. *BMC Bioinformatics* 4(1):2.
DOI: 10.1186/1471-2105-4-2
PMID: 12525261 PMCid:PMC149346

Barabási, A. L., and Oltvai, Z. N., 2004. Network biology: understanding the cell's functional organization. *Nature Reviews Genetics* 5(2):101-113.
DOI: 10.1038/nrg1272
PMID: 14735121

Chandran, U., Mehendale, N., Patil, S., Chaguturu, R., & Patwardhan, B., 2017. Network Pharmacology. Pages 127-164 in B. Patwardhan and R.Chaguturu. , editors. Innovative Approaches in Drug Discovery. Elsevier.
DOI: 10.1016/B978-0-12-801814-9.00005-2
PMID: PMC7148629

Delprato, A., 2012. Topological and Functional Properties of the Small GTPases Protein Interaction Network. PloS one 7(9):e44882.
DOI: 10.1371/journal.pone.0044882
PMID: 23028658 PMCID: PMC3441499

Ding, H., Tauzin, S., & Hoessli, D. C., 2009. Phytochemicals as Modulators of Neoplastic Phenotypes. Pathobiology: journal of immunopathology, molecular and cellular biology 76(2):55-63.
DOI: 10.1159/000201674
PMID: 19367126

Hartwell, L. H., Hopfield, J. J., Leibler, S., & Murray, A. W., 1999. From molecular to modular cell biology. Nature 402 (S6761):47-52.
DOI: 10.1038/35011540
PMID: 10591225

Huang, H., Zhang, G., Zhou, Y., Lin, C., Chen, S., Lin, Y., Mai, S., & Huang, Z., 2018. Reverse Screening Methods to Search for the Protein Targets of Chemo preventive Compounds. Frontiers in Chemistry 6:138.
DOI: 10.3389/fchem.2018.00138
PMID: 29868550 PMCID: PMC595412

Koutsogiannouli, E., Papavassiliou, A. G., & Papanikolaou, N. A., 2013. Complexity in cancer biology: is systems biology the answer? Cancer Medicine 2(2):164-177.
DOI: 10.1002/cam4.62
PMID: 23634284 PMCID: PMC3639655

Pan C. & Dong Z., 2015. Antiasthmatic Effects of Eugenol in a Mouse Model of Allergic Asthma by Regulation of Vitamin D3 Upregulated Protein 1/NF-kappaB Pathway. Inflammation 38: 1385-1393.
DOI: 10.1007/s10753-015-0110-8
PMID: 25588851

Petrovska, B. B., 2012. Historical review of medicinal plants′ usage. Pharmacognosy Reviews 6(11):1-5.
DOI: 10.4103/0973-7847.95849
PMID: 22654398 PMCID: PMC3358962

Shannon, P., Markiel, A., Ozier, O., Baliga, N. S., Wang, J. T., Ramage, D., Amin, N., Schwikowski, B., & Ideker, T., 2003. Cytoscape: A Software Environment for Integrated Models of Biomolecular Interaction Networks. Genome Research 13(11):2498-2504.
DOI: 10.1101/gr.1239303
PMID: 14597658 PMCID: PMC403769

Smoot, M. E., Ono, K., Ruscheinski, J., Wang, P. L., & Ideker, T., 2010. Cytoscape 2.8: new features for data integration and network visualization, Bioinformatics 27(3):431-432.
DOI: 10.1093/bioinformatics/btq675
PMID: 21149340 PMCID: PMC3031041

Phytochemical Composition, Anti-oxidant, Anti-glycation, α-amylase and α-glucosidase Inhibition of Silver Nanoparticles from Extracts of Ardisia Solanacea and Cytotoxic Studies

S. Ravi Kiran[1*], A. Kavitha[1], B.S. Ravi Kumar[2] and A. Rajani[1]

[1] *Department of Botany and Food & Nutrition, R.B.V.R.R. Women's College, Narayanaguda, Hyderabad-500027, Telangana, India*

[2] *Department of Botany and Environmental Studies, AV Kanthamma College for Women, Hassan-573201, Karnataka, India*

***CORRESPONDING AUTHOR:**

S. Ravi Kiran
Email: srksuripeddi@gmail.com

ISSN : 2382-5359(Online), 1994-1412(Print)

DOI:
https://doi.org/10.3126/njst.v22i2.78603

Date of Submission: 8 Feb, 2023

Date of Acceptance: 27 Dec, 2024

ABSTRACT

The aim of this work is to evaluate the anti-oxidant and anti-diabetic activity of extracts of Ardisia solanacea and assess the cytotoxicity as well. The leaves were subjected to solvent extraction and nanoparticles were synthesized using the extracts. The AgNP of methanol extract from leaves of A. solanacea showed the highest total phenolic and flavonoid contents of 35.44 mg of gallic acid/gm and 15.77 mg of quercetin /gm respectively. The TEM analysis revealed that the size of AgNPs ranged between 30 and 47 nm with λmax of 440nm. The AgNP of methanolic extract at 100µg/mL exhibited maximum activity of 89.6% and 84.9% for DPPH and H2O2 scavenging activities respectively. Further, the extracts exhibited excellent NO scavenging, Xanthine oxidase inhibition and anti-glycation activities. The AgNP of methanol extract displayed excellent inhibitory activity with IC50 of 45.47 µg/mL and 56.42 µg/mL respectively for α-amylase and α-glucosidase. The MTT assay for the cytotoxic studies in vitro of extracts on HepG2 cells at varied concentrations was carried out and all the tested extracts and compounds displayed low levels of toxicity in a dose-dependent approach. However, all the extracts exhibited <50% cell death even at the highest concentration of 200 µg/mL. Therefore, Ardisia solanacea could be explored as a bio-friendly natural source of phytoconstituents, which serves as an alternative to conventional synthetic compounds for the treatment and management of various diseases.

Keywords: Anti-oxidant activity, α-amylase, α-glucosidase, Ardisia solanacea, Cytotoxic activity and Silver Nanoparticles

1. INTRODUCTION

Diabetes mellitus is the most common disorder of insulin metabolism and is recognized as one of the health problems that need to be addressed on an urgent basis. According to the current data available in the Diabetes Atlas of the International Diabetes Federation (fourth edition), 285 million among the 7 billion of total world population are affected by diabetes mellitus (Wild et al, 2004). In addition, number of people suffering from impaired glucose tolerance are 344 million and numbers are expected to rise to 438 million for diabetes and 472 million for IGT by 2030 (IDF Diabetes Atlas 2021). Recent research depicts significant evidence stating that diabetes mellitus is a scourge in many low and middle-income countries. Almost one-fifth of the world's people in Southeast Asia are suffering from this disorder, which is responsible for many deaths in most of the countries, and caused 4.6 million deaths in 2011 (IDF Diabetes Atlas, 2021). According to the latest data from the World Health Organization published in 2016, the deaths in Sri Lanka due to diabetes mellitus are 5.7% of total deaths. Sri Lanka is a multi-etimic and multi-religious country with about 20 million people (WHO 2016). Suffering from diabetes is increasing globally with changes in urbanization, lifestyle changes and lack of physical activity. Diabetes cannot be cured as of now and however the blood glucose levels can be maintained through pharmacological and dietary interventions. Phytoconstituents from MAPs have excellent antioxidant and anti-glycation activities that prevent this auto-oxidation and help in preventing complications in diabetes. Over the last few decades, recognition of herbal treatments for diabetes has increased globally as they offer more efficacy, minimal side effects with affordable cost (Brusotti et al. 2014). There are several medicinal plants used in the herbal formulations of traditional medicine like Unani, Chinese and Ayurveda for the management of Diabetes mellitus, but few scientific experiments have proven the efficacy of the plants for their therapeutic potential in either prevention or management of Diabetes mellitus (Brusotti et al. 2014; Dhakad et al. 2018). Therefore, the cutting-edge research needs to evaluate the pharmacological potential and identify the active compounds, as these scientific findings helps the future remedy development industry, to prove the efficacy and standardize herbal medicines.

Medicinal plants and their products have been employed in the management of various metabolic disorders since time immemorial. Research on phytoconstituents from various botanicals showed that they regulate oxidative stress damage by scavenging the free radicals and reactive oxygen species (Ames et al. 1993; Pérez et al. 2021). Previous studies suggest that there is a correlation between disease incidence and diet where, the risk of occurrence of degenerative diseases is less with a higher intake of foods rich in antioxidants (Ghadermazi et al. 2017). Among these, are essential oils from medicinal and aromatic plants comprising mostly of volatile constituents with characteristic aroma and employed in drug, food and perfumery industries (Christenhusz & Byng 2016; Dhakad et al. 2018). There has been growing interest in the usage of plant extracts as anti-oxidant and anti-glycation agents thus conscientious efforts have been placed recently by many researchers throughout the world in the development of novel lead products for the maintenance of well being and management of diabetes.

Ardisia solanacea (A. solanacea) belonging to the family Myrsinacea is an evergreen shrub or tree growing to a height of 12 meters tall and distributed in tropical and subtropical regions of the world. It is commonly known as Duck's Eye in English, Bodina Gida in Kannada and Adavi Mayuri in Telugu. In Asia it is particularly distributed in Southern China, India, Sri Lanka, Nepal, Bhutan, Myanmar and Malaysia. The plant is a repertoire bioactive compounds and is widely used in the treatment of diarrhea, sore throat, dysmenorrhea, gout, rheumatic arthritis, vertigo, bacterial infections and thrombolytic diseases (Khatun et al. 2013; Amin et al. 2015). As a part of screening medicinal plants available in the Western Ghats, A. solanacea was selected based on the ethnobotanical information and literature and therefore, we here present our results of the investigative study.

2. MATERIALS AND METHODS

2.1 Chemicals, solvents, standard compounds and enzymes

The enzymes, α-amylase and α-glucosidase were purchased from Sigma-Aldrich, Bengaluru, India. The solvents and chemicals (analytical grade), Gallic acid, Ascorbic acid, Allopurinol, Aminoguanidine and Acarbose were procured from Sigma-Aldrich, India.

2.2 Plant material

The leaves and stems of Ardisia solanacea were collected near Korahalli (13°2'1.6728'' N 76° 4' 38.1864'' E), near Hassan, Karnataka, India in July 2021 and a voucher specimen has been deposited in the Department of Botany, AV Kanthamma College for Women, Hassan Karnataka (AVK BOT 3018).

2.3 Solvent extraction

The leaves and A. solanacea were subjected to solvent extraction by soaking them separately in various solvents such as Petroleum ether, Ethyl acetate, and Methanol for 8 h followed by homogenization in a mortar and pestle. Then the extracts were filtered using separating funnel, excess solvent was removed using a rotary evaporator under vacuum and dried over anhydrous Na_2SO_4. The light green and pale yellow extracts thus obtained were stored at 4 °C in a refrigerator for further studies.

2.4 Phytochemicals screening

The phytochemicals screening was carried out according to the qualitative standard chemical methods (Trease & Evans 2009). All the solvent extracts were screened for the presence of various phytochemicals such as carbohydrates, alkaloids, Terpenoids, Anthraquinones, Tannins, sterols, and flavonoids using various qualitative analytical tests.

2.5 Biosynthesis of Silver nanoparticles (AgNPs)

Freshly prepared extracts were used for the biosynthesis of AgNPs as per the method described (Parashar et al. 2009). A queous solution of silver nitrate (50 mL of 5×10^{-3} M) was prepared in an Erlenmeyer flask and 1 ml of each solvent extract (0.2 g/mL) was added and kept in the dark for 24 h until the appearance of a brownish color. The absorbance of silver nanoparticles was recorded using Sl-159 spectrophotometer at 200-800 nm range (Theerthavathy et al. 2019) followed by TEM analysis for determination of the size and shape of AgNPs formed (Elevazhagan & Arunachalam 2011).

2.6 Estimation of Total Phenolic content

This was performed as per published method (Ainsworth & Gillespie 2007) with slight modifications and in quintuplicate. Extracts and AgNPs (1 µg/mL; 100 µL), 1M Na_2CO_3 were mixed with Folin-Ciocalteau reagent and incubated in the dark for 15 minutes. The absorbance of the color developed was recorded at 760 nm against reagent blank. Gallic acid was employed as a positive control sample. The total phenolics were determined as mg of gallic acid equivalent per gm of extracts and samples.

2.7 Determination of Total Flavonoid content

The flavonoid content in the extracts and AgNPs was determined using colorimetric assay as per the published method (Aiyegoro et al. 2010) with slight modifications and in quintuplicate. Briefly, extracts (1ml), AgNPs (1mL), aluminum chloride (10%; 0.2 mL), potassium acetate (1M, 0.2 mL) and distilled water (5.6 mL) were mixed thoroughly and incubated at 37 °C for 30 min. Absorbance was recorded at 420 nm in a SL-159 spectrophotometer and the total flavonoids were determined as mg of quercetin equivalents per gram of sample from the calibration curve of quercetin.

2.8 In vitro Antioxidant activity

This was evaluated by adopting the following methodologies.

2.8.1 Determination of FRSA potential using DPPH

The Free Radical Scavenging Ability (FRSA) of extracts and AgNPs of extracts of A. solanacea determined using 1,1-diphenyl-2picrylhydrazyl (DPPH) radical scavenging method (Karadag et al. 2009) with slight modifications and in quintuplicate. The reaction mixture consisted of DPPH solution (1mmol/l in methanol, 2ml) and 1ml of extracts and Ascorbic acid (positive control) were incubated at 37°C for 20 min. The decrease in the absorbance was measured at 517 nm against a reagent blank. The FRSA potential of all samples was determined using the formula.

Free radical scavenging activity (%) = $(A_s - A_t) / A_s \times 100$

Where A_s = Absorbance of standard compound

A_t = Absorbance of sample

2.8.2 Determination of FRSA potential using H_2O_2

This was carried out as per the published method (Ruch et al. 1989) with slight modifications and in quintuplicate. Hydrogen peroxide (43 mM) in phosphate buffer (1 M, pH 7.4) was prepared and used for the analysis. Different concentrations of extracts (10-500µg/ml) were added to an H_2O_2 solution (0.6 mL, 43 mM), incubated for 10 min and absorbance was

measured at 230 nm against phosphate buffer (without H_2O_2) blank. The FRSA potential was assessed by the % inhibition using the formula

% inhibition = (Control- Test) /control ×100

2.8.3 β -Carotene bleaching assay

This assay was performed as per the method of Wettasinghe and Shahidi (1999) with slight modifications and in quintuplicate. Briefly, β -carotene (200µg/ml in chloroform; 2mL) was taken in a round bottom flask and added linoleic acid (20 µL) and Tween 20 (200 µL) mixed and vortexed and evaporated for 10 min at 40 °C. This was followed by the addition of 100 ml of distilled water (HPLC grade). Then the mixture was vortex and 5 ml of the resultant solution was transferred into test tubes containing varied concentrations (10-500 µg/mL) of extracts. Subsequently, the tubes were heated in a water bath at 50 °C for 2 h and then absorbance at 470 nm was measured every 15 min. The antioxidant activity was determined using the formula

Anti-oxidant activity % = $1 - (A_0 - A_t) / (A_0^0 - A_0^t)$

Where, A_0 = Absorbance of control; A_t = Absorbance of sample

2.9 Anti-glycation activity

The Anti-glycation assay was carried out as per the method of Bhatwadekar & Ghole (2005) with slight modifications and in quintuplicate. Briefly, 1 mg/mL of bovine serum albumin was incubated with fructose (0.25 M) and glucose (0.25 M) in phosphate-buffered saline (0.1M, pH 7.4) along with extracts and aminoguanidine (positive control) were dissolved in 50% DMSO and incubated in the dark for 4 days. The glycated protein thus formed was measured at two different wavelengths, 335 nm (Fluorescence, excitation wavelength) and 385 nm (emission wavelength). Extracts at varied concentrations ranging from 1- 100 µg/mL were tested and IC_{50} values were calculated. Subsequently, the percentage inhibition of AGEs was determined using the formula:

AGE % = $(F_{control} - F_{control\ blank}) \times 100 / (F_{extract} - F_{extract\ blank})$

Where,

$(F_{control} - F_{control\ blank})$ is the difference between the fluorescent intensity of BSA incubated with or without glucose and fructose.

$(F_{extract} - F_{extract\ blank})$ is the difference between the fluorescent intensity of BSA and sugars incubated with or without plant extracts.

2.10 α-Amylase inhibitory activity

The assay was performed as per the method of McCue and Shetty, 2004 with slight modifications and in quintuplicate. Extracts (10-100 µg/mL; 250 µL) were taken in suitable vials along with phosphate buffer (0.02 M; pH 6.9; 250 µL) consisting of **α**-amylase (0.5 mg/mL). The mixture was incubated for 10 min. at 37 °C. Starch at a concentration was employed as a substrate and added to the above mixture and further incubated for 10 min. Then the reaction was terminated by the addition of DNS (dinitro-salicylic acid) reagent (500 µL). Subsequently, the vials were placed in boiling water for 5 min, cooled and then diluted with water (5 mL). Subsequently absorbance was recorded at 540 nm. The mixture without extracts and Acarbose were served as negative control and positive control respectively. The enzyme inhibition percentage was measured using the following formula

% Inhibition = $\frac{A_{control} - A_{sample}}{A_{control}} \times 100$

2.11 α-Glucosidase inhibition assay

The α-glucosidase inhibition potential of extracts was evaluated according to the method of Kim et al. (2005) with slight modifications. p-Nitrophenylglucopyranoside (pNPG) (20 mM phosphate buffer, pH 6.9) was employed as a substrate. The **α**-glucosidase (1.0 U/mL, 100 µL) was first incubated with 50 µL of extracts of various concentrations (10-100 µg/mL) for 10 min followed by the addition of 50 µL of 3.0 mM pNPG and further incubated for 20 min at 37 °C. The reaction was terminated by using 2 mL of 0.1 M sodium carbonate. The p-nitrophenol released (yellow color) from pNPG was measured at 405 nm. The results were expressed as % blank control (background absorbance was corrected by replacing enzymes with buffer). Acarbose and buffer were employed as positive and negative controls respectively. The α-glucosidase inhibition percentage was determined by using the following formula

% Inhibition = $\frac{A_{control} - A_{sample}}{A_{control}} \times 100$

2.12 Cytotoxicity Assay

The cytotoxicity of the extracts was assessed according to the method of Mosmann (1983). The HepG2 cells were seeded into 96-well plates (100 µL, 8000 cells per well) and left overnight for adhesion process. Then 100 µl of each of the extracts at concentrations of 10-200

µl/ml/well were added and incubated for 48h at 37 °C. The worn-out medium was removed through aspiration. Subsequently, the DMEM medium (100 µL containing 10% fetal calf serum) and 0.5 mg/ml MTT were added and further incubated for 3h at room temperature. The MTT crystals from the medium were dissolved in DMSO (200 µL/well) and absorbance was recorded at 540 nm. The cytotoxicity was then measured as control % (medium only) and the cell death % and expressed using the equation.

$$\% \text{ Cell death} = 1 - \frac{Absorbance\ of\ test\ well}{Absorbance\ of\ untreated\ well} \times 100$$

2.13 Statistical Analysis

The IC_{50} values were determined by probit analysis. The data obtained was subjected to statistical analysis using GraphPad Prism version 8.01 (Graph pad software, Inc., La Jolla, CA, USA.) and Sigma plot (enzyme module) statistical software.

3. RESULTS AND DISCUSSION

The preliminary phytochemical screening of extracts from leaves of A. solanacea showed the occurrence of alkaloids, terpenoids, flavonoids, tannins, carbohydrates and sterols (Table 1). The results showed that the addition of 0.2 g of the extract to 50 mL of 5 mM aqueous silver nitrate ($AgNO_3$) resulted in the formation of the brown solution after the overnight incubation at 40 °C in the dark. This indicates the formation of silver nanoparticles (AgNPs) that showed a maximum absorption at 440 nm (Fig-1). The TEM analysis revealed that the size of AgNPs ranged between 30 and 47 nm (Fig-2). The total phenolics and flavonoid contents were determined and expressed as mg of gallic acid per gm of sample and depicted in Table 2. The AgNP of methanol extract from leaves of A. solanacea showed the highest total phenolic and flavonoid contents of 35.44 mg of gallic acid/gm and 15.77 mg of quercetin /gm respectively. While, it was 33.71 mg of gallic acid/gm and 13.08 mg of quercetin / gm respectively in the crude methanol extract.

3.1 Anti-oxidant activity

The antioxidant efficacy of extracts of A. solanacea was evaluated and results were depicted in Tables 3-5. The AgNP methanolic extract at 100µg/ml showed maximum activity of 89.6% and 84.9% for DPPH and H_2O_2 scavenging activities respectively. Ascorbic acid exhibited 100% activity at 80µg/ml in both the assays. These results indicate that AgNPs methanol extract has excellent antioxidant activity and is comparable with that of ascorbic acid. The results of β-carotene bleaching assay revealed good antioxidant activity of AgNPs methanol extract with IC_{50} of 58.19 µg/mL followed by methanol extract (IC_{50} of 64.81 µg/mL), ethyl acetate (IC_{50} of 73.34 µg/mL) and pet ether extracts (IC_{50} of 87.28 µg/mL). With the increase in concentration of extracts, a subtle but noticeable increase in the activities was observed in a dose-dependent manner.

3.2 NO scavenging activity

The NO scavenging ability of all the samples was evaluated in a dose-dependent manner using gallic acid as a positive control sample and the results were presented in Table 6. Among all the samples tested, AgNP methanol extract exhibited potent NO scavenging activity with IC_{50} of 37.41 µg/mL followed by methanol (48.12 µg/mL), Ethyl acetate (57.19 µg/mL) and pet ether (76.62 µg/mL) extracts. However, the positive control gallic acid showed an IC_{50} of 29.53 µg/mL. The percentage inhibition with an increase in concentration of extracts and gallic acid was evaluated and the significant observation was that with an increase in concentration, a notable increase in percentage inhibition of NO scavenging activity was observed.

3.3 Xanthine oxidase inhibition

All the extracts were evaluated as potential XO inhibitors and compared favorably with Allopurinol, a positive control and the results are summarized in Table 7. Among all the extracts tested, AgNP methanol extract showed maximum xanthine oxidase inhibition activity with an IC_{50} of 28.78 µg/mL. The methanol, ethyl acetate, and pet ether extract also demonstrated excellent xanthine oxidase inhibition with an IC_{50} of 38.13, 60.08, and 72.18 µg/mL respectively. While, Allopurinol showed an IC_{50} of 18.17 µg/mL.

3.4 Anti-glycation activity

The ability of A. solanacea extracts to inhibit advanced glycation end product (AGE) formation was evaluated and presented. In the assay, bovine serum albumin, glucose and fructose served as the model protein and glycating agents respectively. The formation of AGEs was evaluated by monitoring the production of fluorescent products formed at 335 nm and 385 nm, respectively, and the results are depicted in Table 8 and all the extracts inhibited AGE formation in a

dose-dependent manner. The AgNP methanol extract presented a higher inhibitory effect of more than 90% inhibition of AGE formation at a concentration of 100 µg/mL with an IC_{50} of 35.12 µg/mL. Methanol extract also displayed excellent anti-glycation activity with an IC_{50} value of 44.28 µg/ml followed by Ethyl acetate (64.13 µg/mL) and Pet ether (72.29 µg/mL) extracts. While, the Aminoguanidine, showed IC_{50} of 22.76 µg/mL. The degree of activity was evaluated for all the extracts and compounds at a concentration ranging from 1-100 µg/mL where, increase in percentage inhibition with increase in concentration was observed.

3.5 α- Amylase inhibition

The α-amylase enzyme inhibition of extracts was evaluated and presented in Table 9. The AgNP methanol extracts demonstrated excellent inhibitory activity with IC_{50} of 45.47 µg/mL while Acarbose showed an IC_{50} value of 28.49 µg/mL. The methanol and ethyl acetate extract also showed good inhibition with an IC_{50} of 59.23 and 66.05 µg/mL respectively. The assay was performed at varied concentrations of 0-100 µg/mL and with increase in concentration a noticeable increase in the inhibition percentage was noticed (Fig. 3).

3.6 α-Glucosidase inhibition

The α-glucosidase enzyme inhibition of extracts was evaluated and presented in Table 10. AgNP methanol extract displayed excellent inhibitory activity with IC_{50} of 56.42 µg/mL while it was 33.51 µg/mL for acarbose. Both methanol and ethyl acetate extracts showed good inhibition with IC_{50} of 61.71 and 77.27 µg/mL respectively. While, pet ether extract demonstrated mild inhibition with IC_{50} of 88.61 µg/mL. The assay was performed at varied concentrations of 0-100 µg/mL where, increase in the inhibition percentage was noticed with increase in the concentration of samples (Fig. 4).

3.7 Cytotoxicity studies

The assay employed 3-(4,5-dimethylthiazol-2-yl)-2,5-diphenyl tetrazolium bromide (MTT) for evaluation of cytotoxicity of all the extracts on HepG2 cells at varied concentrations (0-200 µg/mL). All the tested extracts presented low level of toxicity at all the concentrations in a dose-dependent manner and the results are depicted in Fig. 5-8. The IC_{50} values obtained were 458.79, 358.53, 292.28 and 241.72 µg/mL respectively, for AgNP methanol extract, methanol, ethyl acetate and pet ether extracts. The significant feature was that all the extracts exhibited <40% cell death even at the highest concentration of 200 µg/mL.

4. DISCUSSION

The phenols, flavonoids, and terpenes of various medicinal plants are well known important compounds in plants contributing to the antioxidant potential of various botanicals (Khan et al. 2019; Batool et al. 2019; Bindu et al. 2020). Phytochemicals derived from medicinal botanicals are known to possess primary antioxidant activity as they can react with active oxygen radicals, such as hydroxyl radicals, superoxide anion radicals and lipid peroxy radicals and inhibit lipid oxidation at an early stage. It has also been reported that the increase in the phenolic content can be used as a biomarker for screening of air pollutants (Howell 1974; Stankovic et al. 2016). Considerable research has been carried out and established that flavonoids are antioxidants compounds and recognized as valuable nutraceuticals for neutralizing free radical stress (Gunathilake et al. 2018). The antioxidant properties of plant extracts can often be attributed to the presence of substantial amount of phenolics and flavonoids. In the present study, all the extracts from A. solanacea demonstrated excellent anti-oxidant activity and this can be correlated to the presence of more amounts of phenolics and flavonoids and might be employed in the treatment of stress and other related disorders.

The phenolics, flavonoids and other phytochemicals derived from medicinal plants have known to act as xanthine oxidase inhibitory agents (Cho et al. 2008; Shukor et al. 2018). The Plants are well known as a rich source of polyphenols and some of the common species, were previously reported to possess XO inhibitory effects (Cho et al. 2008; Shukor et al. 2018). Moreover, the results in the present study are in agreement with those of previously reported plants (Grevsen et al. 2009; Hudaib et al. 2011). At present, Allopurinol is the drug of choice for gout disease and people are using it more frequently. However, upon prolonged usage, the drug presents various side effects. Therefore, as a part of screening program of medicinal plants of Western Ghats, South India, and also based on the ethnobotanical information, A. solanacea plant was selected for xanthine oxidase inhibitor activity evaluation, wherein, all the extracts have displayed marked inhibitory activity comparable to allopurinol.

The effect of plant-derived compounds and extracts

on protein glycation was evaluated by the inhibition of fructosamine formation. It was found that all the extracts of A. solanacea exhibited varied degree of potential to inhibit initial stages of glycation reaction. The hyperglycemic state that is commonly seen in Diabetes mellitus patients was reported to be associated with cardiovascular complications (Chen et al. 2011) and this evidence implicates the formation and subsequent effects of AGEs as a contributing cause for such a complication. Further, it has been reported recently that there is increased oxidative damage in the vicinity of glycated histone residues (Guedes et al. 2011; Mahomoodally et al. 2019). Advanced glycation end products (AGEs) have been involved in the pathogenesis of diabetes and aging-related complications and therefore, inhibition of glycation should have a broad and beneficial effect in the treatment. However, several traditionally used herbal medicines and essential oils have been shown to possess in vitro anti-glycation effects due to the presence of flavonoids, terpenes and phenols (Mahomoodally et al. 2019). The AgNP extract in the present study displayed excellent ant-glycation activity by inhibiting more than 90% of AGEs formation which can be attributed to the presence of higher concentration phenolics and flavonoids. However, the synergistic effect of all the components in the extract cannot be neglected.

Plants are the major source of valuable biochemicals and bioactive compounds for the development of lead products. The extracts of A. solanacea was reported to exhibit good antioxidant, antimicrobial, thrombolytic, anthelmintic, insect antifeedant and cytotoxic activities (Samal 2013; Amin et al. 2015; Anjum et al. 2019; Islam et al. 2019; Pournami and Pratap Chandran, 2021). But the anti-oxidant and anti-glycation potential of silver nanoparticles of the extract and inhibition of α-amylase and α-glucosidase was not reported. The novelty of the present work lies in the exploration of potential of silver nanoparticles of the extracts of the selected plant to inhibit the formation of AGEs and carbohydrate metabolizing enzymes.

The use of medicinal plants in the management of diabetes has been followed and many therapeutic plants with anti-diabetic activity were reported in the literature (Saeedi et al., 2019; Nipun et al., 2021). Several reports have been focused on the studies of the therapeutic potential of medicinal plants and phytoconstituents in alleviating diabetes by inhibitory effects against α-amylase and α-glucosidase (Loodu & Rupasinghe 2019). The molecules acting as α-amylase and α-glucosidase enzyme inhibitors are recognized and portrayed to delay the breakdown of carbohydrates in the small intestine and decrease the postprandial blood glucose levels (Assefa et al., 2020). This feature is tapped and considered as one of the key strategies for the maintenance of blood glucose levels. The results obtained from this study showed that these extracts possess promising α-amylase and α-glucosidase enzyme inhibition, which are in agreement with the published reports (Assefa et al. 2020). However, identification and evaluation of toxicity of the phytoconstituents and botanical extracts is indispensable before making it a formulation and incorporating them into traditional medicine. The cytotoxicity of extracts was assessed on HepG2 cells and the results reveals that all the samples exhibited less than 40% cell death even at the highest concentration of 200 µg/ml. All the samples displayed a very low level of toxicity in comparison with the plants described and published in the literature which have been presented with > 50% cell death (Kuete et al. 2017). This particular aspect encourages for the use of this plant and extracts in herbal formulations for the treatment of various ailments.

5. CONCLUSION

The current study revealed that silver nanoparticles can be synthesized in a simple method using A. solanacea leaf extract. The TEM analysis showed that the sizes of the synthesized AgNps ranged from 30 to 50 nm. The AgNP and other extracts showed excellent anti-oxidant activity, NO scavenging activity and xanthine oxidase inhibition and this can be attributed to the presence of a substantial amount of phenols, flavonoids, and terpenoids. Advanced glycation end products (AGEs) have been involved in the pathogenesis of diabetes and aging-related complications and therefore, inhibition of glycation should have a broad and beneficial effect in the treatment. The AgNPs and other extracts in the present study displayed excellent ant-glycation activity with >90% inhibition of AGEs. The MTT assay for the cytotoxic studies of extracts on HepG2 cells at varied concentrations was carried out and all the tested extracts displayed low levels of toxicity at all concentrations in a dose-dependent approach. However, the extracts exhibited <50% cell death even at the highest concentration of 200 µg/mL. Therefore, further studies are underway to isolate phytoconstituents of this plant and other biochemical aspects where the data procured might help in the lead products and formulation development for the management of stress-related

disorders and diabetes.

ACKNOWLEDGEMENTS

The authors express their gratitude to Dr. J. Achyutha Devi, Principal, R.B.V.R.R. Women's College, Narayanaguda, Hyderabad, India for providing the necessary facilities to carry out the work and also for her encouragement and support.

DECLARATION OF COMPETING INTEREST

The authors declare that there is no conflict of interest.

Table 1: Phytochemical screening of extracts of A. solanacea

Parts used	Secondary metabolites	Petroleum ether extracts	Ethyl acetate extracts	Methanol extracts	AgNP extract
Leaves	Tannins	-	+	+	+
	Flavonoids	-	-	+	+
	Alkaloids	-	+	++	++
	Terpenoids	+	+	++	++
	Anthaquinones	_	_	-	-
	Carbohydrates	_	+	+	+
	Sterols	++	+	+	+

Data shown as obtained from the analysis (n=5)

Table 2: Total phenolics and flavonoid content in the extracts of A. solanacea

Extract	Total phenolics content (mg of gallic acid/gm)	Total flavonoid content
Methanol extract	33.71±0.77	13.08± 0.59
Ethyl acetate extract	28.62±0.98	10.26± 051
Pet ether extract	22.26±1.06	8.17± 0.99
AgNP of Methanol extract	35.44±1.23	15.77± 1.27

Data presented as Mean ± SEM

Table 3: DPPH anti-oxidant scavenging activity of extracts of A. solanacea

Concentration (µg/ml)	DPPH radical scavenging activity (%)				
	Pet ether extract	Ethyl acetate Extract	Methanol	AgNP Methanol extract	Ascorbic acid
10	6.73 ± 0.61	9.71 ± 0.43	11.12 ± 0.79	14.72 ± 0.98	21.23±0.57
20	12.11 ± 0.84	17.34 ± 0.92	22.25 ± 0.92	27.21 ± 0.89	33.45 ± 0.98
40	23.08 ± 1.06	28.38 ± 1.02	34.18 ± 1.14	40.08 ± 1.01	48.19 ±1.17
60	35.76 ± 1.22	43.67 ± 1.15	46.38 ± 1.62	58.47 ± 1.23	78.26 ± 1.28
80	44.93 ± 1.99	54.18 ± 1.98	64.57 ± 2.26	67.19 ± 2.17	100
100	57.28 ± 2.25	68.26 ± 2.07	78.72 ± 2.48	89.61± 1.24	100

Test extracts: significant from normal control, $P < 0.05$
Values presented as Mean ± SEM

Table 4: H_2O_2 free radical scavenging activity of extracts of A. solanacea

Concentration (µg/mL)	Hydrogen peroxide free radical scavenging activity (%)				
	Pet ether extract	Ethyl acetate Extract	Methanol	AgNP Methanol extract	Ascorbic acid
10	5.35 ± 0.52	9.17 ± 0.37	9.04 ± 0.68	11.22 ± 0.72	24.45±0.71
20	9.11 ± 0.79	18.34 ± 0.82	19.65 ± 0.93	23.16± 0.93	38.51 ± 0.96
40	17.15 ± 1.12	26.26 ± 1.22	30.23 ± 1.23	38.28 ± 1.21	51.32 ±1.08
60	29.51 ± 1.38	40.67 ± 1.35	48.19 ± 1.75	65.81 ± 1.25	88.16 ± 1.37
80	36.34 ± 1.91	51.23 ± 1.78	60.39 ± 2.29	73.37± 1.09	100
100	52.81 ± 2.34	64.16 ± 2.37	72.28 ± 2.37	84.92± 2.19	100

Test extracts: significant from normal control, $P < 0.05$

Values presented as Mean ± SEM

Table 5: β-carotene bleaching activity of extracts of A. solanacea

Sl. No.	Sample/Extract	IC50 (µg/mL)
1.	Pet ether extract	87.28 ± 2.15 (72.288 – 92.193)
2.	Ethyl acetate extract	73.34 ± 1.56 (63.724 – 81.156)
3.	Methanol extract	64.81 ± 1.32 (54.189 – 69.342)
4.	AgNP extract	58.19 ± 1.27 (49.211 – 64.394)

Test extracts: significant from normal control, $P < 0.05$Values presented as Mean ± SEM

Table 6: NO scavenging activity of essential oil, extracts and isolated compounds from leaves of A. solanacea

S. No.	Sample/Extract	IC50 (µg/mL)	Relative Potency
1.	Pet ether extract	76.62 ± 1.58 (69.198 – 92.232)	0.385
2.	Ethyl acetate extract	57.19 ± 1.61 (65.183 – 85.412)	0.516
3.	Methanol extract	48.12 ± 1.42 (56.721 – 72.328)	0.614
4.	AgNP Methanol extract	37.41 ± 1.49 (28.188 – 46.237)	0.789
8.	Gallic acid	29.53 ± 1.31 (20.172 – 30.244)	1

Test extracts: significant from normal control, $P < 0.05$
Values are expressed as Mean ± SE; Relative potency = IC_{50} standard/IC_{50} sample
Numbers in parenthesis represent 95% confidence limits

Table 7: Xanthine oxidase inhibitory potential of extracts of A. solanacea

Compound	IC50 (µg/mL)	Relative Potency
Pet ether extract	72.18 (62.244 – 84.282)	0.252
Ethyl acetate extract	60.08 (57.281 – 66.402)	0.302
Methanol Extract	38.13 (27.228 – 45.417)	0.476
AgNP methanol extract	28.78 (22.627 – 36.608)	0.631
Allopurinol	18.17 (13.621 – 23.893)	1

Test extracts: significant from normal control, $P < 0.05$; All values are expressed as Mean ± SE; Relative potency = IC_{50} standard/IC_{50} sample;
The numbers in parenthesis represents 95% confidence limits

Table 8: Anti-glycation activity of extracts of A. solanacea

Compound	IC50 (µg/mL)	Relative Potency
Pet ether extract	72.29 (66.991 – 89.407)	0.315
Ethyl acetate extract	64.13 (54.812 – 76.245)	0.354
Methanol extract	44.28 (34.138 – 54.188)	0.514
AgNP methanol extract	35.12 (26.231 – 41.463)	0.648
Aminoguanidine	22.76 (18.231 – 27.334)	1

Test extracts: significant from normal control, $P < 0.05$

All values are expressed as Mean ± SE; Relative potency = IC_{50} standard/IC_{50} sample;

The numbers in parenthesis represents 95% confidence limits

Table 9: α-amylase inhibition of extracts from A. solanacea

Compound/Extract	IC50 value (µg/ml)	Relative Potency
Petroleum ether extract	83.32 ± 3.12	0.342
Ethyl acetate extract	66.05 ± 4.01	0.431
Methanol extract	59.23 ± 2.98	0.481
AgNP methanol extract	45.47 ± 2.43	0.627
Acarbose	28.49 ± 0.42	1

Values shown as mean ±SE (P<0.05)

Table 10: α-glucosidase inhibition of extracts from A. solanacea

Compound/Extract	IC50 value (µg/mL)	Relative Potency
Pet ether extract	88.61 ± 2.33	0.366
Ethyl acetate extract	77.27 ± 2.17	0.419
Methanol extract	61.71 ± 2.29	0.525
AgNP methanol extract	56.42 ± 2.12	0.575
Acarbose	33.51 ± 1.18	1

Values presented as mean ±SE (P<0.05)

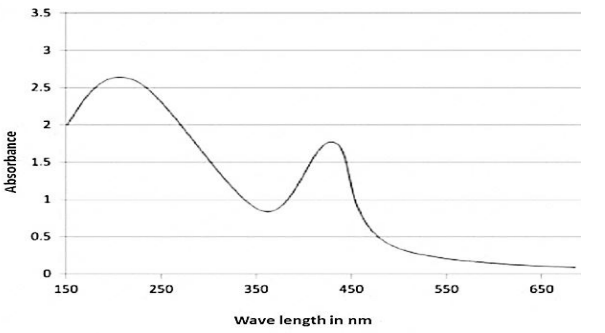

Fig.1: UV Absorption curve of AgNPs of methanol extract

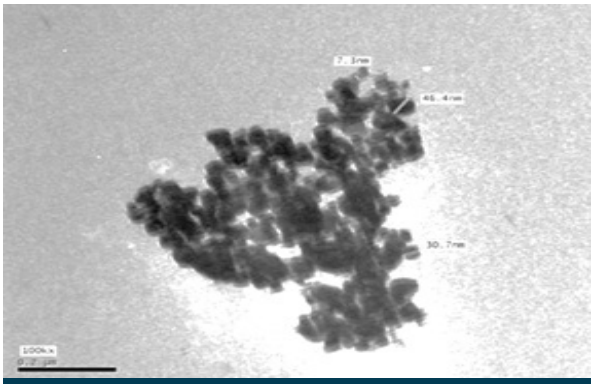

Fig.2: TEM of AgNPs of methanol extract of A. solanacea

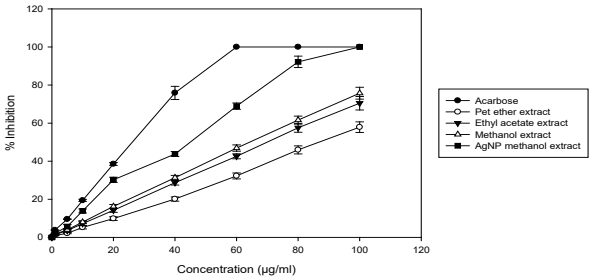

Fig.3: Inhibition (%) of α-amylase activity at varying concentrations of extracts from A. solanacea. Values presented as mean ±SE (P<0.05)

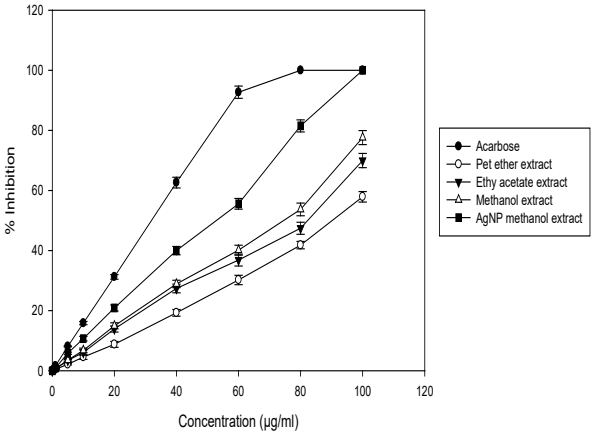

Fig.4: Inhibition (%) of α-glucosidase activity at varying concentrations of extracts from A. solanacea.

Values presented as mean ±SE (P<0.05)

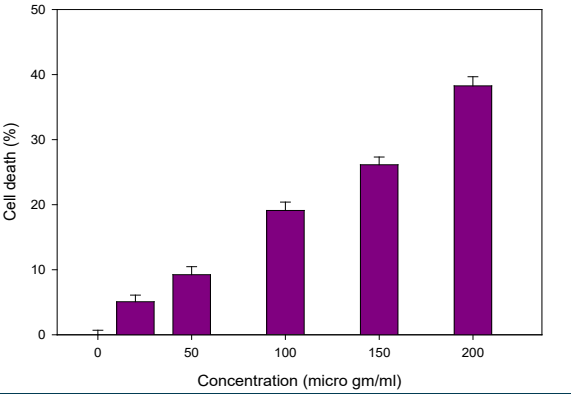

Fig.5: Cytotoxicity assay of the petroleum ether extract of A. solanacea HepG2 liver cells. Data presented as % control ± SE (p<0.05)

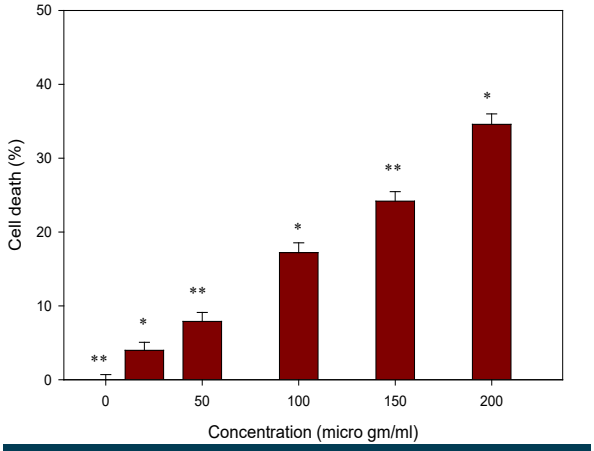

*Fig.6: Cytotoxicity assay of the Ethyl acetate extract of E. monogynum on HepG2 liver cells. Data presented as % control ± SE (*p<0.05; **p<0.01)*

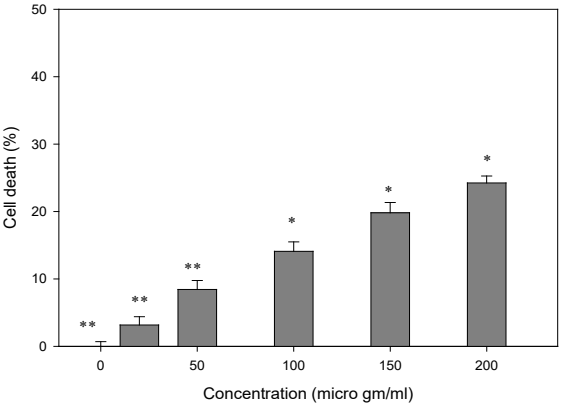

*Fig.7: MTT cytotoxicity of the Methanol extract from leaves of A. solanacea on HepG2 liver cells. Data presented as % control ± SE (*p<0.05; **p<0.01)*

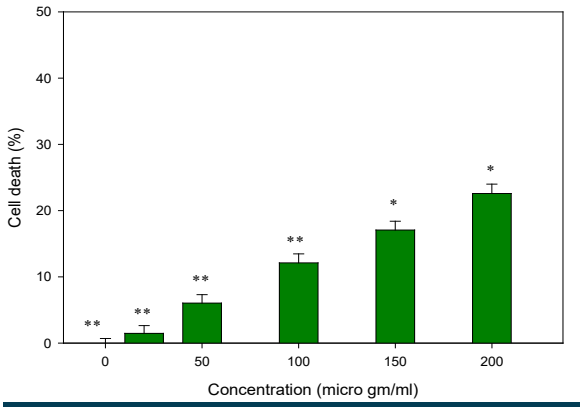

*Fig.8: MTT Cytotoxicity of the AgNP extract from leaves of A. solanacea on HepG2 liver cells. Data presented as % control ± SE (*p<0.05; **p<0.01)*

REFERENCES

Ainsworth, E.A., and K. Gillespie, 2007. Estimation of total phenolic content and other oxidation substrates in plant tissues using Folin-Ciocalteu reagent. *Natural Products* 2:875-877
DOI: 10.1038/nprot.2007.102
PMID: 17446889

Aiyegoro, O.A., and A.I. Okoh, 2010. Preliminary phytochemical screening and in vitro antioxidant activities of the aqueous extract of Helichrysum longifolium DC. *BMC Complementary and Alternative Medicine* 10: 21-28
DOI: 10.1186/1472-6882-10-21
PMID: 20470421 PMCID: PMC2877649

Ames, B.N., M.K. Shigenaga, T.M. Hagen, 1993. Oxidants, antioxidants, and the degenerative diseases of aging. Proceedings of National Academy of Sciences USA 90: 7915-7922.
DOI: 10.1073/pnas.90.17.7915
PMID: 8367443 PMCID: PMC47258

Amin M.N., S. Banik, Md. Ibrahim, M.R. Moghal, M.S. Majumder, R. Siddika, Md.K. Alam, K.M.R.M. Jitu, and S.N. Anonna, 2015. Study on Ardisia solanacea for Evaluation of Phytochemical and Pharmacological Properties. International *Journal of Pharmacognosy and Phytochemistry* 7: 8-15.

Anjum B., R. Kumar, R. Kumar, O. Prakash, R.M. Srivastava, and A.K. Pant, 2019. Phytochemical Analysis, Antioxidant, Anti-Inflammatory and Insect Antifeeding Activity of Ardisia solanacea Roxb. Extracts. *Journal of Biologically Active Products from Nature*, 9: 372-386.
DOI: 10.1080/22311866.2019.1702899

Assefa, S.T., E.Y. Yang, S.Y. Chae, M. Song, J. Lee, M.C. Cho, and S. Jang, 2020. Alpha glucosidase inhibitory activities of plants with focus on common vegetables. Plants 9: 2-17
DOI: 10.3390/plants9010002
PMID: 31861279 PMCID: PMC7020213

Batool, R., M.R. Khan, M. Sajid, S. Ali, and Z. Zahra, 2019. Estimation of phytochemical constituents and in vitro antioxidant potencies of Brachychiton populneus (Schott & Endl.) R.Br. BMC Chemistry 13: 32.
DOI: 10.1186/s13065-019-0549-z
PMID: 31384780 PMCID: PMC6661765

Bhatwadekar, A.D., and V.S. Ghole, 2005. Rapid method for the preparation of an AGE-BSA standard calibrator using thermal glycation. *Journal of Clinical Lab Analysis* 19:11-15.
DOI: 10.1002/jcla.20048
PMID: 15645463 PMCID: PMC6807708

Bindu G., V.R.Ch. Devi, B.S.R. Kumar, and S. R. Kiran, 2020. Chemical composition and in vitro potential activity on glucose metabolism and cytotoxicity of leaves of Erythroxylum monogynum Roxb. *Medicinal Plants* 12: 568-579.
DOI: 10.5958/0975-6892.2020.00069.6

Brusotti, G., I. Cesari, A. Dentamaro, G. Caccialanza, and G. Massolini, 2014. Isolation and characterization of bioactive compounds from plant resources: The role of analysis in the ethno-pharmacological approach. Journal of Pharmaceutical and Biomedical Analysis 87:218-228.
DOI: 10.1016/j.jpba.2013.03.007
PMID: 23591140

Chen, Y.F., H.Y. Roan, C.K. Lii, Y.C. Haung, and T.S. Wang, 2011. Relationship between antioxidant and anti-glycation ability of saponins, polyphenols and polysaccharides in Chinese herbal medicines used to treat diabetes. *Journal of medicinal Plants Research* 5:2322-2331.

Cho, Y.J., I. S. Ju, D.H. Yun, S. S. Chun, B. J. An, and J. H. Kim, 2008. Biological activity of extracts from garden sage (Salvia officinalis L.) *Journal of Applied Biochemistry* 51:296-301.
DOI: 10.3839/jabc.2008.046

Christenhusz, M.J.M., and J. W. Byng, 2016. The number of known plants species in the world and its annual increase. Phytotaxa 261:201-217.
DOI: 10.11646/phytotaxa.261.3.1

Dhakad, A.K., V.V. Pandey, S. Beg, J.M. Rawat, and A. Singh, 2018. Biological, medicinal and toxicological significance of eucalyptus leaf essential oil: a review. *Journal of Science Food and Agriculture* 98:833-848.
DOI: 10.1002/jsfa.8600
PMID: 28758221

Elavazhagan T., and K.D. Arunachalam, 2011. Memecylonedule leaf extract mediated green synthesis of silver and gold nanoparticles. International *Journal of Nanomedicine* 6: 1265-1278.
DOI: 10.2147/IJN.S18347
PMID: 21753878 PMCID: PMC3131193

Ghadermazi, R., F. Khoshjou, S.M. Hossinizijoud, H. Behrooj, N. Kheiripour, and M. Ganji, 2017. Hepatoprotective effect of tempol on oxidative toxic stress in STZ-induced diabetic rats. Toxin Reviews.37:1-5.
DOI: 10.1080/15569543.2017.1313277

Grevsen, K., X.C. Frette, and L.P. Christensen, 2009. Content and composition of volatile terpenes, flavonoids and phenolic acids in Greek oregano (Origanum vulgare L. ssphirtum) at different development stages during cultivation in cool temperate climate. European Journal of Horticultural Science 74:193-203.
DOI: 10.1079/ejhs.2009/1182840

Guedes, S., R. Vitorino, M.R. Domingues, F. Amado, and P. Domingues, 2011. Glycation and oxidation of histones H2B and H1: in vitro study and characterization by mass spectrometry. Analytical and Bioanalytical Chemistry. 399:3529-3539.
DOI: 10.1007/s00216-011-4679-y
PMID: 21274518

Gunathilake, K.D.P.P., K.K.D.S. Ranaweera, and H.P.V. Rupasinghe, 2018. Effect of different Cooking Methods on Polyphenols, Carotenoids and Antioxidant Activities of Selected Edible Leaves. Antioxidants 7: 117.
DOI: 10.3390/antiox7090117
PMID: 30200223 PMCID: PMC6162770

Howell, R.K., 1974 Phenols, ozone and their involvement in the physiology of plant injury. Pages 94-105 in M. Dugger, editor. Air Pollution Related to Plant Growth, A.C.S. Symposium. Series 3.Washington D C,USA.
DOI: 10.1021/bk-1974-0003.ch008

Hudaib Khaled, M.M., A. Tawaha, M.K. Mohammad, A.M. Assaf, A.Y. Issa, F.Q. Alali, T.A. Aburjai, and Y.K. Bustanji, 2011. Xanthine oxidase inhibitory activity of the methanolic extracts of selected Jordanian medicinal plants. Pharmacognosy Magazine 7: 320-324.
DOI: 10.4103/0973-1296.90413
PMID: 22262935 PMCID: PMC3261066

IDF Diabetes Atlas. 2021. 10th Edition, https://diabetesatlas.org/idfawp/resource-files/2021/07/IDF_Atlas_10th_Edition_2021.pdf.

Islam, M.R., J. Naimam N. M. Proma, Md.S. Hussain, S. M. Naimuddin, and M. K. Hossain. 2019. In-vivo and in-vitro evaluation of pharmacological activities of Ardisia solanacea leaf extract. Clinical Phytoscience 5: 32-42. DOI: 10.1186/s40816-019-0128-9

Karadag, A., B. Ozcelik, and S. Saner, 2009. Review of Methods to Determine Antioxidant Capacities. Food Analytical Methods 2:41-60
DOI: 10.1007/s12161-008-9067-7

Khan, W.A., S. Subhan, D.F. Shams, S.G. Afridi, R. Ullah, A.A. Shahat, and A. S. Alqahtani, 2019. Antioxidant Potential, Phytochemicals Composition, and Metal Contents of Datura alba. Biomed Research International 2403718: 1-8.
DOI: 10.1155/2019/2403718
PMID: 31317024 PMCID: PMC6601491

Khatun, A., M. Rahman, S. Kabir, M.N. Akter, and S.A. Chowdhury, 2013. Phytochemical and Pharmacological properties of methanolic extract of Ardisia humilis Vahl. (Myrsinaceae). International Journal of Research in Ayurveda and Pharmacy 4: 38-41
DOI: 10.7897/2277-4343.04120

Kim, Y.M., Y.K. Jeong, M.H. Wang, M.Y. Lee, and H.I. Rhee, 2005. Inhibitory effect of pine extract on -glucosidase activity and postprandial hyperglycemia. Nutrients 21:756-761
DOI: 10.1016/j.nut.2004.10.014
PMID: 15925302

Kuete, V., F.W. Fokou, O. Karaosmanoglu, V.P. Beng, and H. Sivas, 2017. Cytotoxicity of the methanol extracts of Elephantopusmollis, Kalanchoe crenataand other Cameroonian medicinal plants towards human carcinoma cells. BMC Complementary and Alternative Medicine 17:280-289.
DOI: 10.1186/s12906-017-1793-1
PMID: 28545532 PMCID: PMC5445369

Kulkarni, O., 2010. Ambiguity in the authenticity of traded herbal drugs in India: Biochemical evaluation with aspecial reference to Nardostachys jatamansi DC. Journal of herbal medicine and Toxicology 4: 229-235

Loodu, S.S., and H.P.V. Rupasinghe, 2019. Evaluation of anti-oxidant,Anti-diabeticandAnti-obesitypotential of selected traditional medicinal plants. Frontiers in Nutrition 6: 1-11
DOI: 10.3389/fnut.2019.00053
PMID: 31106207 PMCID: PMC6494929

Mahomoodally, F., Z.A. Elalfi, K.N. Venugopala, and M. Hosenally, 2019. Anti-glycation, comparative antioxidant potential, phenolic content and yield variation of essential oils from 19 exotic and endemic medicinal plants. Saudi Journal of Biological Sciences 26:1779-1788
DOI: 10.1016/j.sjbs.2018.05.002
PMID: 31762658 PMCID: PMC6864152

McCue, P., and K. Shetty, 2004. Inhibitory effects of rosmarinic acid extracts on porcine pancreatic amylase in vitro. Asia Pacific Journal of Clinical Nutrition 13:101-106

Mosmann, T., 1983. Rapid colorimetric assay for cellular growth and survival: application to proliferation and cytotoxicity assays. Journal of Immunological Methods. 65:55-63
DOI: 10.1016/0022-1759(83)90303-4
PMID: 6606682

Nipun, T.S., A. Khatib, Q.U. Ahmed, M.H.M. Nasir, F. Supandi, M. Taher, and M.Z. Saiman, 2021. Preliminary phytochemical screening, in vitro anti-diabetic, anti-oxidant activities, and toxicity of leaf extracts of Psychotriamalayana Jack. Plants 10: 1-23
DOI: 10.3390/plants10122688
PMID: 34961160 PMCID: PMC8707723

Parashar, V., R.Parashar, B. Sharma, and A.C. Pandey, 2009. Parthenium leaf extract mediated synthesis of silver nanoparticle: a novel approach for weed utilization. Digest J*ournal of Nanomaterials and Biostructures* 4: 45-50.

Pérez-Torres, I., V. Castrejón-Téllez, M.E. Soto, M.E. Rubio-Ruiz, L. Manzano-Pech, and V. Guarner-Lans, 2021 Oxidative Stress, Plant Natural Antioxidants, and Obesity. International *Journal of Molecular Sciences* 22:1786
DOI: 10.3390/ijms22041786
PMID: 33670130 PMCID: PMC7916866

Pournami T.S., and R. P. Chandran, 2021. Evaluation of phytochemical and antimicrobial properties of leaf extracts of Ardisia solanacea Roxb. collected from Pathiramanal Island, Alappuzha District, Kerala State, India. Arabian *Journal of Medicinal and Aromatic Plants* 7: 175-191.

Ruch, R.J., S.J. Cheng, and J.E. Klaunig, 1989. Prevention of cytotoxicity and inhibition of intercellular communication by antioxidant catechins isolated from Chinese green tea. Carcinogenesis 10:1003-1008
DOI: 10.1093/carcin/10.6.1003
PMID: 2470525

Saeedi, P., I. Petersohn, P. Salpea, B. Malanda, S. Karuranga, N. Unwin, S. Colagiuri, L. Guariguata, A.A. Motala, and K. Ogurtsova, 2019. Global and regional diabetes prevalence estimates for 2019 and projections for 2030 and 2045: Results from the International Diabetes Federation Diabetes Atlas, 9th ed. *Diabetes Research and Clinical Practice* 157: 107843
DOI: 10.1016/j.diabres.2019.107843
PMID: 31518657

Samal, P.K, 2013. Evaluation of Antioxidant activity of Ardisia solanacea in albino rats. *Research Journal of Pharmacy and Technology* 6: 585-588.

Shukor, N.A.A., A. Ablat, N.A. Muhamad, and J. Mohamad, 2018. In vitro antioxidant and in vivo xanthine oxidase inhibitory activities of Pandanus amaryllifolius in potassium oxonate-induced hyperuricemic rats. *International Journal of Food Science & Technology* 53:1476-1485
DOI: 10.1111/ijfs.13728

Stankovic, N., M.K. Tatjana, Z. Bojan, S.J. Vesna, M. Violeta, J. Jovana, C. Ljiljana, K. Branislava, and B. Nirit, 2016 Antibacterial and antioxidant activity of traditional medicinal plants from the Balkan Peninsula. *NJAS - Wageningen Journal of Life Sciences* 78: 21-28
DOI: 10.1016/j.njas.2015.12.006

Theerthavathy, B.S., S.A. Khanam, B.S. Kumar, and S. R. Kiran, 2019. Anti-oxidant and Anti-microbial Activities of Silver Nanoparticles of Essential Oil Extracts from Leaves of Zanthoxylum ovalifolium. European *Journal of Medicinal Plants* 29: 1-11
DOI: 10.9734/ejmp/2019/v29i330157

Trease, G.E., and W.L. Evans, 2009. Pharmacognosy. 16th ed.; London: BailliereTindall Ltd.

Wettasinghe, M., and I.F. Shahidi, 1999. Evening primrose meal: A source of natural antioxidants and scavenger of hydrogen peroxide and oxygen-derived free radicals. *Journal of Agricultural and Food Chemistry* 47:1801-1812
DOI: 10.1021/jf9810416
PMID: 10552455

WHO., 2016. Global Diabetes Report. Publications of the World Health Organization, http://www.who.int, WHO Press, 20 Avenue Appia, 1211 Geneva 27, Switzerland.

Wild, S., G. Roglic, A. Green, R. Sicree, and H. King, 2004. Global prevalence of diabetes: Estimates for the year 2000 and projections for 2030. Diabetes Care 27:10471053.
DOI: 10.2337/diacare.27.5.1047
PMID: 15111519

Rapid Genetic Purity Test in Rice (*Oryza sativa* L.) Using Novel *Transit Albino* Mutant

R. Thangapandian[1*] and S.R. Shri Rangasami[2]

[1] Cotton Research Station, Srivilliputtur-626 135, Virudhunagar District, TamilNadu, India
[2] Department of Forage Crops, TNAU, Coimbatore -641 003, TamilNadu, India

***CORRESPONDING AUTHOR:**

R. Thangapandian
Email: ricetha@gmail.com

ISSN : 2382-5359(Online), 1994-1412(Print)

DOI:
https://doi.org/10.3126/njst.v22i2.78604

Date of Submission: 8 Feb, 2023

Date of Acceptance: 17 Jun, 2024

ABSTRACT

The objective of this study was to develop the new variability in mega seed rice varieties by establishing the novel phenotypic marker. This new genetic variability could be immediate beneficial to the seed industry. The *green-revertible* albino mutant 'a-16' was developed from the mega rice variety, ASD16 by mutation breeding approach. The albino seedling was turned into normal green seedling at 3-7 leaf stage and this trait is inherited and controlled by Mendelian single recessive gene. The stable *green-revertible* albino trait was evaluated at different stages to screen the large-scale genetic admixtures at nursery level in a short period of time. A lot of measures were taken to assess the genetic purity in the field and laboratory which could reveal the results after harvest. The adoption of *green-revertible* albino mutant could reproduce the precise result at seedling level, hence, application of *green-revertible* albino mutant in seed industry requires technological and policy interventions urgently to verify the rice productivity level in major rice growing areas.

Keywords: Breeding, green-revertible albino, off-type, genetic admixtures

1. INTRODUCTION

Rice is the staple food for more than 60 per cent of the world population. About 90 per cent of all the rice grain in the world is produced and consumed in Asia. In India alone, rice is cultivated on more than 44.6 million hector (ha) with an average productivity of 3.76 tons/hector (t/ha) with the recorded attainable yields of 10 t/ha (Prasad *et al.* 2001), reveals an exploitable yield gap of nearly 6 t/ha. The yield gap could be achieved by utilizing the genetic variability, innovative approaches and engineering of more productive plant architecture in rice. Intensive research has decisively added numerous traits in rice to enhance input use efficiency cum withstand stress conditions but failed to raise

potential yield (Inada & Katsura 1984). Difficulties in using genetic variability and limitations to conventional breeding-selection approaches foil attempts to breach the potential yield of 10 t/ha (Mao *et al*. 1996).

Rapid advances in plant molecular biology leading to sequencing of genome can help mine and use very large number of hitherto unknown genes through functional and applied genomics to overcome the genetic constraints to raising yield threshold. Many consider that the future of crop improvement will depend primarily on how the genomic knowledge is used to locate additional or new variability and move the genes of interest across the barrier of sexual incompatibility. Advances in molecular genetics will greatly help to transfer the new traits from distant sources. It may take as long a time as conventional breeding to breed a variety of choice by genetic engineering and overcome the hurdles in deregulating for commercial planting (Muralidharan *et al.*, 2019). Genes involved in leaf color often have a role in photosynthetic pigment production and chloroplast development. Albino, chlorosis, thermo-color, light green, brown, yellow, stay-green, stripes and zebra, green-revertible albino, dark green, and purple are among the color types resulted from leaf-color mutations (Sheng *et al.* 2014; Cao 1999). Morphological traits are often used by breeders as selection markers in traditional rice breeding

The creation of new variability in rice displayed a novel beneficial albino trait *i.e., green-revertible* albino that could be applied in hybrid rice technology to identify the off-types during the hybrid seed production in China. The male sterility in T/PGMS lines are highly influenced by higher temperatures and long day photoperiod conditions, if a dramatic change in temperature occurs during the male sterility inductive period, the male sterile lines become partially fertile and the hybrid seed would be contaminated. A new T/PGMS line with a leaf color mutation as a screening marker is one economically feasible way to increase dependability of this system in China (Shen *et al.* 1994).

Though the molecular marker technology is used to ascertain the genetic purity of rice variety, it requires high cost besides skilled technicians for assessing the genetic contamination in the random sampling of any paddy variety. In this juncture, alternate techniques might be considered as viable option to assess the genetic purity of any rice variety at farm level. Hence, *green-revertible* albino mutant can also be applied to screen genetic admixtures in a short span of time without involving skilled labour at nursery level. With this view, the study was carried out to assess the genetic purity of the released mega variety with mutation breeding approach to establish the novel *green- revertible* albino trait.

2. MATERIALS AND METHODS

2.1 Seed preparation in mutagen solution

Currently the total annual planting area of rice is more than 1600 thousand hectares in Tamil Nadu. The rice varieties viz., ADT 36, ADT 38, ADT39, ADT 43, ADT 45, BPT 5204 and ASD 16 occupy more than 75 per cent of rice cultivation area in Tamil Nadu due to its stability in yield potential and consumer preferences. Every year genetic admixture in seed production plot become menace to both public and private seed producers, ultimately the farmers are suffered. To get rid of this problem, mutation breeding was initiated at Tamil Nadu Rice Research Institute, Audthurai. Filter sterilized solution of NaN_3 (1.5 Molar Sodium Azide) was prepared in deionized water and diluted with sterile 0.1 Molar phosphate buffer (pH 3) to prepare 0.001 Molar, 0.002 Molar, 0.003 Molar, 0.004 Molar and 0.005 Molar working solution to treat the seeds of these varieties. The seeds were first placed in sterile deionized water for 30 minutes to imbibe seeds and then submerged in mutagen solution for 60 minutes. Seeds submerged in deionized water for the same period of time served as control.

2.2. M1 plants and seed harvest

However, there was good reason not to use the highest mutagen dose because that leads to unwanted mutations at some of the loci resulting in lethality with poor or no germination. This made relatively low doses attractive to reduce the amount of work in screening of M_1 plants. The treated seeds were sown in the field as per the dose level. At maturity, seeds were bulk harvested from each M_1 plant.

2.3 Production of homozygous stable *green-revertible* albino seedlings

The M_2 seeds were directly planted at South Farm, Tamil Nadu Rice Research Institute, Aduthurai during 2010. The variants with apparent leaf color changes were isolated and labeled at the 1-3 leaf stage (7 days after sowing). Seedlings that survived chlorophyll

deficiency were transplanted into a paddy field. The mature mutants with similar agronomic characters to the original parent were harvested to produce M_3 plant lines. Seeds of M_3 plant lines were separated for field evaluation. The field evaluation carried out by planting the M_4 to M_8 generations plant lines. The homozygous stable *green-revertible* albino plants were obtained from the treated rice variety, ASD 16. The novel mutant 'a-16' with transit (*green-revertible*) albino marker was found to express albino leaves at the 3-7 leaf stage (7-21 days) and reverted back to normal green color periodically before transplanting. The mature mutant plant possessed mostly similar agronomic traits as the original plant of rice variety, ASD16 evaluated in progeny row and replicated row trial. The mature mutant plant expressed uniform transit albino traits and the survival rate of albino seedlings were significantly on par with original parent.

2.4 Selection of economically important agronomic traits

The selected mutant 'a-16' with *green-revertible* albino trait was reciprocally crossed with the original parent, ASD16. The F_1 plants were self-pollinated to obtain F_2 progenies. Leaf color phenotype of F_1 and F_2 plants was recorded at the 1-3 leaf stage. The seedlings were planted with the original parent, and seedling heights of the mutant 'a-16' were recorded at 6-leaf stage (18 days after sowing). The rooting pattern of the mutant along with original parent was recorded at the 3-leaf stage (7 days after sowing). The economically important agronomic traits *viz*., plant height, tiller numbers, panicle length, florets per panicle, 1000-grain weight, seed setting rate and single plant yield were also recorded in mature plants of both mutant and original plant. The important grain quality properties *viz*., amylose content, gel consistency and starch content were recorded to assess the changes in physico-chemical properties of the derived mutant from the original parent.

3. RESULTS AND DISCUSSION

3.1 Chlorophyll deficient mutations and their behavior in M_2 and subsequent generations

In the M_2 generation, about 1,54,760 seedlings were grown for isolating chlorophyll-deficient mutations. Four mutant phenotypes, *i.e.*, albino, light yellow, light green, and striped albino were identified from the normal green population. On a per plant basis, the total frequency of chlorophyll-deficient mutations reached 0.036%. Out of 58 albino mutants' only nine albino mutants were survived due to green reversibility, other mutants were neglected since they not exhibited scope for improvement of economically important traits (Inada and Katsura, 1984). The surviving mutant had albino leaves between 1- and 7-leaf stages (up to 21 days), later turned into green (revertible) color from leaf base to leaf tip. The albino trait slowly turned into green color (revertible) at 15 days old seedlings and this conversion process continued up to 21 days old seedlings and finally appeared as normal green color. The economic important agronomic traits between the mature mutant and its original parent are similar and no significant variation was recorded (Table 1). Although it had albino traits up to 6-7 leaf stage, the rooting pattern between the albino and normal green seedlings had significant variation, the albino seedlings showed longer root length than normal green seedlings. Similarly, the leaf blade width of green-revertible albino mutant was decreased than the original parent, ASD16; hence leaf area index (LAI) in mutant plant showed no conducive for the leaf folder incidence. Those were considered an important trait for practical breeding approach to develop the resistance mechanism against key pest since no adverse effect was noticed.

3.2 Stability of albino mutation under the field condition

In M_3 generation (Kharif and Rabi season, 2010), the mutant 'a-16' exhibited the green revertible albino phenotype (Fig. 1 a-d) as recorded in M_2 generation, indicating that the *green-revertible* albino mutation is fixed and heritable. Subsequent generations M_3-M_8 were evaluated (Kharif season, 2011-16) in field trials, further confirmed that the green revertible mutant 'a-16' retained the trait due to inheritance. Therefore, in terms of stability of the green-revertible albino trait, the inheritance pattern of novel trait was carried out subsequently. The *green-revertible* albino mutant (transit albino) can be used as a phenotypic marker for rapid removal of off–types or genetic admixtures in the seed production plot and the genetic purity of the variety could be fixed at seedling stage. It gives the feasibility to determine the genetic purity of the variety at nursery level before conducting grow-out test (GOT). A lot of measures were taken to assess the genetic purity in the field and this could be ensured in grow-out test (GOT) after harvest (Vigneshwari *et al.*

2014). The adoption of *green-revertible* albino mutant in seed industry requires technological and policy interventions urgently to verify the rice productivity level in major rice growing areas. Due to lack of skilled labour for rouging operation, genetic admixtures could definitely be appeared and its genetic contamination reduces the productivity level in rice. According to the research forecast; 1% impurity in seed lot may decrease the potential yield of varieties and hybrids by about 100 kg/ha; which is accounted for huge yield losses to the farmers (Mao et al. 1996).

3.3 Inheritance of *green-revertible* albino trait

The green revertible albino mutant plants were crossed with the original parent, ASD6 and reciprocal cross combination was also made between them during 2016. All F_1 plants from the reciprocal crosses had normal green leaves. A total of 512 albino plants and 563 albino plants were identified from the a-16/ASD16 population (2083 F_2 plants) and ASD16/a-16 population (2126 F_2 plants). The ratios of green plants to albino plants in the two populations were 3.017:0.983 or 2.941:1.059 respectively, fitting to the expected 3:1 ratios (Table 2). F_3 seedling observations found that the progenies derived from the F_2 albino plants were uniform for albino leaves, however, two-third of F_2 green plant derived progenies segregated in leaf color and the ratio of green plant to albino plants fitted well to the expected 3:1 ratios. This indicated that the albino trait was controlled by a single recessive gene. A novel thermo/photoperiod-sensitive genic male sterile rice mutant with green-revertible albino leaf color marker was employed in two line hybrid rice technology in China (Wu *et al.* 2001; Wu *et al.* 2003). The green-revertible albino trait was controlled by single recessive gene in this study.

At present, the study of leaf coloring mechanism in rice is mainly through the identification of leaf color mutants, senescence-associated mutants and the functional analysis of senescence. Although some genes related to aging and leaf color have been cloned successfully, it is still unclear whether and how some important metabolic pathways (such as photosynthesis, photorespiration, cytoplasmic receptor kinase pathways, anthocyanin biosynthesis pathway, etc.) are involved and regulated in rice leaf color variations (W. Li *et al.* 2022). Future studies in this area will help to further understand the molecular mechanisms of rice leaf coloring and provide in-depth theoretical basis for this morphological trait to be a more dependable marker in the breeding program of rice.

3.4 Economically important characters

There were very slight variations in seedling heights at the 3-5 leaf stage (14 days) between the albino mutant 'a-16' and the original parent because the nutrition for seedling development at that stage is mainly provided by the rice endosperm. The rooting pattern of green revertible albino mutant is more vigorous (Fig. 2) than normal green seedlings besides other chlorophyll deficient albino seedlings are shown poor root growth and it died before attaining at the 1-3 leaf stage. Due to poor photosynthesis caused by chlorophyll deficiency, the mutant seedling became significantly stunned at the 3-5 leaf stage (Fig. 3a & 3b). Then seedling growth was normal after turning into green (Fig. 4a & 4b) color at 5-6 leaf stage. Further observation indicated that the chlorophyll deficiency at the seedling stage did not influence subsequent development. There is more similarity in various agronomic characters between the *green-revertible* albino mutant and its parent (Fig. 5); which showed no adverse effect on economically important characters. Hence, the mutant could directly become beneficial to the farmers and seed producers respectively, provided large scale demonstration will be evaluated further to ascertain the off-type elimination during the seed production of mega rice variety. There were no differences in grain quality traits *viz.*, kernel length, kernel breadth, kernel length: breadth ratio, linear elongation ratio, and volume expansion ratio between the green-revertible mutant and original parent (Table 3). Similarly, no major changes were noticed in their chemical properties *i.e.*, alkali spreading value and amylose content (Fig. 6). This is an important observation from the practical breeding point of view. Since the mutated trait is not linked to any adverse effect on other traits, it can be used directly in rice breeding programme and seed industry.

Genes involved in leaf color often have a role in photosynthetic pigment production and chloroplast development. Albino, chlorosis, thermo-color, light green, brown, yellow, stay-green, stripes and zebra, green-revertible albino, dark green, and purple are among the color types resulted from leaf-color mutations (P. Sheng *et al.* 2014; L.Q.Q. Cao. 1999). Morphological traits are often used by breeders as selection markers in traditional rice breeding and molecular implications in useful gene identification. To help identifying hybrids, certain leaf color features,

such as purple or pale green, have been introduced into sterile or restorer lines (Peng *et al.* 2012). In recent years, breeders have paid an increasing attention to the value of altered leaf color phenotypes.

4. CONCLUSION

Application of transit (*green-revertible*) albino mutant in rice mega varieties diminishes all the problems existed during the quality rice seed production, and it gives platform for seed producers to remove the genetic admixture at seedling stage (nursery level). A farmer can also be involved to remove the genetic admixture seedlings by identification of leaf color (Peng et al. 2012). The *green-revertible* albino mutant development in mega rice variety could be become beneficial to screen the large-scale genetic admixtures at nursery level and cultivation area could definitely be increased by supplying quality seeds to the farmers. The adoption of *green-revertible* albino mutant in seed industry requires technological and policy interventions urgently to verify the rice productivity level in major rice growing areas. This precise phenotyping will remain as the foundation of future crop improvement. A genomic breeding approach is used to locate the new variability and find the gene of interest (*green-revertible*) trait in the mutant background. This work provided feasibility to obtain desired yield improvement by supplying quality seeds to the farmers with assured genetic purity. Rapid advances in plant molecular biology leading to sequencing of genome can help mine and use very large number of unknown gene sources through functional and applied genomics to overcome the genetic constraints to raising yield threshold.

ACKNOWLEDGEMENTS

We thank the Director, Tamil Nadu Rice Research Institute, Aduthurai for support and facilities. We also thank Dr. K. Chozhan, Professor (Entomology) for encouraging the corresponding author to pursue this research and we also extend our gratitude to Dr. K. Thiyagarajan, Professor (Plant Breeding) for critical comments.

Table 1: Economically important traits between the mutant and parent

Genotype	Days to 50% flowering	Plant height (cm)	No. of productive tillers per plant	Panicle length (cm)	No.of filled grains per panicle	1000 grain weight (gm)	Single plant yield (gm)
Green-revertible albino mutant	80.6	93.40	12.9	23.46	152.73	24.84	52.84
ASD 16 (parent)	81.5	95.60	13.4	23.68	154.32	25.43	57.25

(Note: data in the table is mean value; which is derived from the 50 plants randomly recorded)

Table 2: Inheritance pattern of green-revertible albino mutant 'a-16' in reciprocal crosses

Seedling color					
Genotype	Normal green	Green revertible albino	Expected ratio	Chi square value χ^2	Observed ratio
F_1 ASD16 / a-16	56	0			
F_2	1571	512	3:1	0.20	3.017: 0.983
F_1 a-16 /ASD16	43	0			
F_2	1563	563	3:1	2.489	2.941:1.059

Table 3: Grain quality traits between the mutant and parent

Genotype	Kernel length (mm)	Kernel breadth (mm)	Kernel length: breadth ratio	Linear elongation ratio	Volume expansion ratio	Alkali spreading value	Amylose content (%)
Green-revertible albino mutant	5.32	2.02	2.63	1.28	4.21	3.24	20.23
ASD 16 (parent)	5.38	2.02	2.66	1.24	4.10	3.33	20.11

(Note: data in the table is mean value; which is derived from the 50 grains randomly recorded)

Fig.1a: Albino seedling at 3-leaf stage

Fig.1b: Albino seedling at 3-leaf stage

Fig.1c: Green-revertion starts at 4-leaf stage

Fig.1d: Green-revertion starts at 4-leaf stage

Fig.2: Green-revertible albino mutant line - M3

Fig.3a: Green-revertible albino turns into normal seedling at 5-6 leaf stage

Fig.3b: Green-revertible albino turns into normal seedling at 5-6 leaf stage

Fig.4: Root growth differences between green-revertible albino and normal seedling

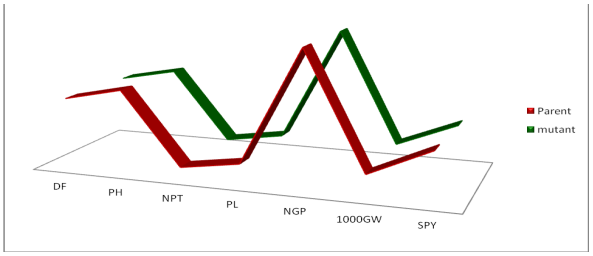

Fig.5: Comparison of agronomic traits between mutant and parent

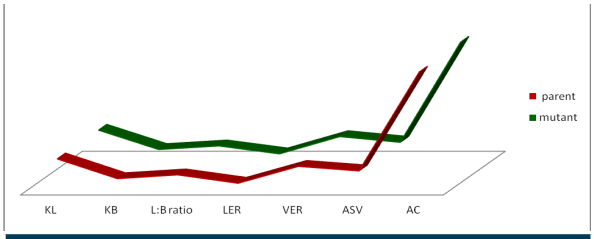

Fig.6: Comparison of grain quality traits between mutant and parent

REFERENCES

Cao, L., LiYong, C., Qian Qian, Q. Q., Zhu XuDong, Z. X., Zhen DaLi, Z. D., Min ShaoKai, M. S.,and Xiong ZhenMin, X. Z..1999. Breeding of a photo-thermo sensitive genic male sterile indica rice Zhongzi S with a purple-leaf marker and the hoterosis of its hybrid rice produced with it, Acta Agron. Sin. 25: 44-49.

Inada, K.and N. Katsura, 1984. A rice mutant entirely lacking chlorophyll b. Japan *Journal of Crop Science* 53: 445-449
DOI: 10.1626/jcs.53.445

Mao, C.X., S.S. Virmani, and I. Kumar, 1996. Technological innovations to lower the costs of hybrid rice seed production. In:Virmani,SS. *et al.*, (eds). Advances in hybrid rice technology. Proceedings of Third International Symposium on Hybrid Rice, Directorate of Rice Research, Hyderabad, India

Muralidharan, K., G.S.V. Prasad, C.S. Rao, and E.A. Siddiq, 2019.Genetic gain for yield in rice breeding and rice production in India to meet with the demand from increased human population. Current Science 116: 544-560.
DOI: 10.18520/cs/v116/i4/544-560

Prasad, G.S.V., K. Muralidharan, and C.S. Rao, 2001. Stability and yield performance of genotypes, A proposal for re-grouping world rice area into mega environments. Current Science 81: 1337-1346.

Peng, Y., Y. Zhang, J. Lv, J. Zhang, P. Li, X. Shi, Y. Wang, H. Zhang, Z. He, and S. Teng, 2012. Characterization and fine mapping of a novel rice albino mutant low temperature albino 1, J. Genetics Genomics 39: 385-396.
DOI: 10.1016/j.jgg.2012.05.001
PMID: 22884095

Shen, Y.W., M.W. Gao, and Q.H. Gai, 1994. A novel environment-induced genic male sterile (EGMS) mutant in indica rice. Euphytica 76: 8-96.
DOI: 10.1007/BF00024024

Sheng, P., J. Tan, M. Jin, F. Wu, K. Zhou, and W. Ma, 2014. Albino midrib 1 , encoding a putative potassium efflux antiporter , affects chloroplast development and drought tolerance in rice, Plant Cell Rep. 1581-1594.
DOI: 10.1007/s00299-014-1639-y
PMID: 24917171

Vigneshwari, R., A. Vijayakumar, and M. Bhaskaran, 2014. Morphological characterization of major paddy cultivars in seed chain of TamilNadu. *International Journal of Agricultural Sciences* 1: 280-285.

Weiran Li, Z. Yuchan, Md. A. R. Mazumder, R. Pan and D. Akhter. 2022. Research Progresses on rice leaf color mutants. Crop Design. Vol. 1:2. 100015
DOI: 10.1016/j.cropd.2022.100015

Wu, D.X, S. Q.Shen, H. Cui, Y.W. Xia, and Q. Y. Shu, 2003. A novel thermo/photoperiod-sensitive genic male-sterile (T/PGMS) rice mutant with green-revertible albino leaf color marker induced by gamma irradiation. Field Crops Res., 81: 141-147.
DOI: 10.1016/S0378-4290(02)00218-6

Wu, D.X., Q.Y. Shu, and Y.W. Xia, 2001. A novel male sterile line suitable for ensuring and measuring the purity of hybrid rice seed. Seed Science and Technology 29: 129-133.

Structural Characterisation and Docking Studies of Copper Homocysteine Complex with Cytochrome c Oxidase, Glutathione Peroxidase, Superoxide Dismutase for Evaluation of Metal Mediated Homocysteine Toxicity

P. Jhansi Lakshmi[1*]

[1]*Department of chemistry, R.B.V.R.R Women's college, Hyderabad, Narayanaguda, Hyderabad, Telangana, India*

***CORRESPONDING AUTHOR:**

P. Jhansi Lakshmi
Email: jhansipadithem@gmail.com

ISSN : 2382-5359(Online), 1994-1412(Print)

DOI:
https://doi.org/10.3126/njst.v22i2.78605

Date of Submission: 8 Feb, 2023

Date of Acceptance: 2 Jun, 2024

ABSTRACT

An emerging understanding of the role and regulation of homocysteine metal ion interactions during oxidative injury which leads to vascular pathogenesis underlines metal ion importance and need for more research on this aspect. In the present work metal ion interactions in solution and as well as solid state were carried out. Synthesized Cu (II), Ni (II) and Zn (II) complexes with homocysteine. The complexes were further characterized spectrally with IR, UV, Mass, ESR, X-ray photoelectron spectroscopy and TGA techniques. The possible geometries of metal complexes were evaluated using the molecular mechanics calculations. The refined structures were screened based on lowest strain energies calculated by applying MM3 force field. The molecular docking study of copper complex was performed by using Autodock4.2 software against Cytochrome C oxidase, Glutathione peroxidase 1 and Superoxide Dismutase 1 enzymes. Based on analytical, conductance, magnetic and electronic spectral data the Cu (II) and Zn (II) complexes are assigned tetrahedral geometry and Ni (II) complex is assigned square planar geometry. These complexes are formulated as [M(L)H2O]. The formation constants for the interaction of metal ions with homocysteine under physiological conditions as well as the structure and composition of metal complexes synthesized provide some evidence to earlier biochemical studies on animal models. The docking values obtained in the present study may provide supporting information for the biochemical studies related to homocysteine toxicity in presence of metal ions. The binding interactions at these enzymes active site revealed that copper homocysteine complex interaction led to Inhibition of COX, SOD and Glutathione peroxidase enzymes activity, a possible mechanism for therapeutic intervention to treat diseases caused by homocysteine toxicity.

Keywords: Copper homocysteine complex , Cytochrome C oxidase , docking studies, Formation constants, Glutathione peroxidase 1 , Homocysteine toxicity Superoxide Dismutase

1. INTRODUCTION

The transition metal ions inevitably exist as metal complexes in biological systems by interaction with the numerous biomolecules possessing functional groups capable of complexation or chelation G.L. Eichorn (1973), H. Sigel, Marcell Dekker (1998), M. N. Hughes (1981). In all metallobiomolecules the essential metal ions such as Cu, Zn, Cr, Fe, Mn, and Co exist as binary, and ternary chelates of amino acids, carboxylic acids and proteins. Without these interactions, life could not exist or even come into being without the mediating action of metal ions. This is evident by the role of metal ions in many biological processes such as: catalytic activity of metalloenzymes, regulation of nucleic acids replication, pharmacological activity of many metal complexes, etc. Bertini, I.; Gray, H.B (2007), Ferré-D'Amaré AR, Winkler WC. (2011), Kaluđerović GN, et al. (2012), Katherine J. Franz and Nils Metzler-Nolte (2019). In all metalloenzymes the metal ion is usually coordinated with nitrogen, oxygen or sulfur atoms belonging to amino acids in the polypeptide chain incorporated into the protein.

The interactions between the amino acid and the metal ions are thus considered as models of the processes which take place at the molecular level in the metal protein system. Although studies of the systems of metals with various amino acids have been carried out (Farkas, E. & Sovago, I., 2007; Z. Ozturk et al. 2014; Ahmed, Mahmood & Qadir, Muhammad. 2014; Arunadevi, Alagarraj, and Natarajan Raman (2020) detailed information on the mode of coordination of homocysteine (hCy) with metal ions at biological conditions in solution are not available. In order to get a better understanding of the toxic effects of homocysteine, studies are carried out in solution and solid state of various metal ion interactions with homocysteine at physiological conditions ($t=37^0$, $\mu=0.15M$). The homocysteine molecule is potentially a tridentate ligand and may chelate with the metallic cations using the carboxylate oxygen, amino nitrogen, and thiolate sulphur as the donor atoms. In the blood, homocysteine being very active can form binary complexes, the physiological action of homocysteine is connected with its ability to form complexes with metal ions (Dong D et al. 2013; Keskitalo, Salla et al. 2014; Ledda C et al. 2019) including Cu^{2+}, Zn^{2+}, Ni^{2+}, Co^{2+}, Cd^{2+} and Pb^{2+}. Determining the stability of the metal complexes and their structures will be helpful in understanding the physiological function of this amino acid . In the present study, copper homocysteine complex synthesized was docked with COX1, SOD1 and Glutathione peroxidase enzymes to understand the copper mediated catalytic activity of these enzymes and to provide possible mechanism for copper mediated homocysteine toxicity (Hultberg et al. 1997; Fan, X et al. 2020).

2. MATERIALS AND METHODS

2.1 pH METRIC STUDIES

Evaluation of formation constants for binary metal complexes ML containing hCy with transition metal ions like Cu (II) Co(II), Ni(II), Zn(II), Cd(II) and Pb(II) were studied potentiometrically. Further detailed physico chemical studies of the mixed ligand complexes (ML_nA_n ; where n=1) containing the following L and A ligands has been carried out. Ligand L : Homocysteine (primary ligand) **:** Ligands A (Secondary ligands) : $N\text{-}O^-$ donors: α –alanine, β- alanine, N-N donors: 2,2' –bipyridyl, 1,10-phenanthroline $^-O\text{-}O^-$donors: Oxalic acid, malonic acid, pyrocatechol. The formation constants are evaluated at the physiologically relevant temperature (37.0 ^{0}C) and ionic strength (μ = 0.15M) by a pH – metric method involving the titration of solutions containing 1:1 molar ratio of metal ion and ligands L for binary systems with standard carbonate free sodium hydroxide. In the present investigation the computer program "Stability constants of Generalized Species" [SCOGS] Sayce IG (1968) was used to calculate the protonation constants of the free ligands and formation constants of the protonated, mono binary, bis binary metal complexes. SCOGS can be used to analyze appropriate pH titration data to yield protonation constants, metal ion hydrolysis constants, stability constants of simple complexes (ML, ML_2, etc.), stability constants of polynuclear species (M_2L_3 , M_2L_4 , M_2L_2OH etc.) . In addition to this, distributions and concentrations of various species present as a function of pH were also computed from known constants and are presented in the form of pH species distribution profiles by using the computer programme SPE (Smith, Robert M et al. (1985), Rajarajan, Govindasamy et al. 2021) such profiles are very useful in visualizing the nature and concentrations of various species present in solution, under a given set of conditions.

2.2 Synthesis, Spectral Characterisation Of Homocysteine Binary Metal Complexes

In the present work we have synthesized the complexes of homocysteine with Cu(II), Ni(II) and Zn(II) and had attempted to understand the mechanism of copper mediated homocysteine induced vascular pathogenesis and Alzheimer's disease. In blood, homocysteine molecules possess the ability to form chelate complexes with metallic cations through coordinate covalent bonds with the negatively charged carboxylate oxygen, the amino group nitrogen and the thiolate group sulphur.

2.2.1 Synthesis of Cu(II) & Ni(II) homocysteine complexes:

The Cu(II) complex was obtained as follows: 0.0676g hCy (Sigma-Aldrich) in 5ml aqueous Cu(II) solution containing 0.0852 g $CuCl_2.2H_2O$ at a 1:1 molar ratio Cu:hCys. This resulted in formation of a solid blue Cu (II) complex, that precipitated after 24 hrs. The crystalline powder was filtered and collected under vacuum. The Ni(II) complex was obtained as follows: 0.0676g hCy (Sigma-Aldrich) in 5ml aqueous Ni(II) solution containing 0.0952 g $NiNO_3$ at a 1:1 molar ratio Ni:hCy. This resulted in formation of a brown solid complex that precipitated after 24 hrs.

2.2.2 Ir And Esr Studies

Infrared spectra were obtained on a FTIR instrument in the range of 4000- 400cm^{-1}. The electronic paramagnetic resonance spectra (EPR) of the copper complex were recorded on Varian-E-112 at room temperature.

2.2.3 X-Ray Photoelectron Spectral Studies (Xps)

The XPS spectra are recorded on a VG Escalab 200 MK spectrometer equipped with an Al-Kα source and a hemispherical analyzer connected to a five-channel detector. The spectra are recorded with constant pass energy of 20 eV. Binding energies were determined by computer fitting of the measured spectra . Powder samples are mounted for analysis. The most widely used method is dusting the powder onto a polymer-based adhesive tape with a camel-hair brush.

2.2.4 Mass Spectra

The EI mass spectra were recorded on a VG micromass 7070-H instrument, ESIMS spectra were recorded on VG AUTOSPEC mass spectrometer.

2.2.5 Electronic Spectra

Electronic spectra of metal complexes in DMSO were recorded on Schimadzu UV-VIS 1601 spectrophotometer.

2.2.6 Magnetic studies

Magnetic susceptibilities of the complexes were determined on Gouy balance model 7550 using Hg [Co $(NCS)_4$] as standard. The diamagnetic corrections of the complexes were computed using Pascals constants.

2.2.7 Thermal studies

TGA of metal complexes were carried on Mettler Toledo Star system in the temperature range of 0-1000^0 C.

3. MOLECULAR MECHANICS AND DOCKING STUDIES OF HOMOCYSTEINE BINARY METAL COMPLEXES

The possible geometries of metal complexes were evaluated using the Molecular mechanics calculations with Hyperchem and Mopac packages. Initially the atomic charges of each complex were calculated by a semi-empirical method (ZNDO). The structures using the standard force field included in the package, further refinement was done for the complexes . The refined structures were screened on the basis of the lowest strain energies. The energies of the resulting systems were calculated using the MM3 forcefield. Copper homocysteine metal complex docking studies were carried out into Cytochrome C oxidase1, Glutathione peroxidase 1 and Superoxide Dismutase 1 enzymes (Zong, S et al. 2018; Manjula, R et al. 2018) using Autodock4.2 software (Morris GM, 2009). Docking of Copper homocysteine metal complex was carried out on crystal structures of Cytochrome C oxidase (PDB_ ID: 5Z62), Glutathione peroxidase 1(PDB_ID: 2F8A), and Superoxide Dismutase 1 (PDB_ID: 5YTO). These PDB structures were retrieved from protein data bank. During the docking for Cytochrome C oxidase we have used 0.375Å grid box parameters as centre: x = 326.731, y = 340.743, z = 247.895 and grid box size: x=40, y=42, z=40. For Glutathione peroxidase 1 we have used 0.375Å grid box parameters as centre: x = -0.939, y = 22.701, z = 27.518 and grid box size: x=42, y=42, z=52 and for Superoxide Dismutase 1 we have used 0.375Å grid box parameters as centre: x = 51.881, y = 62.96, z = -17.525 and grid box size:

x=40, y=42, z=48. While docking 10 conformations were generated for each ligand by using default genetic algorithm. In this study, input preparation carried out using MGLtools-1.5.6 and final docking performed in Autodock 4.2. The interaction of the metal complexes with DNA was also studied by molecular modelling with special reference to docking.

4. RESULTS AND DISCUSSION

4.1 Acid Dissociation Constants For Free Ligand (L)

The pH titration curve shown in **Fig-1** was obtained by adding increasing amounts of alkali to free ligand containing hCys in (H_3L) form. The pH titration curve in the presence of three protons shows a steep inflection at a=1(a= moles of base added per mole of ligand) followed by a buffer region ending a=3 with a small inflection at a=2. The titration curve at low pH region showed the dissociation of –COOH group and at high pH the simultaneous dissociation of $–NH_3^+$ and –SH groups was observed. From the potentiometric titration data for the ligand hCys the dissociation constants were computed from the computer programme SCOGS by taking into consideration the relevant species H^+, H_3L, H_2L, HL and L. The dissociation constants thus obtained for hCy at 37^0 C and μ = 0.15M (KNO_3) ionic strength were listed in **Table-1** and a schematic representation of the ligand dissociation is given in **Fig-2.** The pK_{1a} value is assigned to dissociation of a proton from the carboxylate oxygen. The pK_{2a} and pK_{3a} values are in very close proximity and hence the dissociation of both the amino and thiol protons may be taking place simultaneously in the buffer region of a=1 to a=3. A pH ligand species profile for hCys is represented graphically in **Fig-3**. The maximum concentrations of the various species and the corresponding pH values are H_2L =90.91% at pH=2.0, HL = 98.24% at pH 7.0 and L=99.30% at pH=12.

4.2 Binary Metal Complxes Of Homocysteine (L)

The formation constants of metal complexes formed by interaction of M(II) {Cu(II), Ni(II), Ca(II), Mg(II), Pb(II), Cd(II), Co(II) and Zn(II)} with hCy were studied. The potentiometric titration curves for the interaction of various metal ions with homocysteine in presence of three moles of acid taken in a 1:1 molar ratio are shown in **Fig-4**. For binary systems involving the metal ion Cd (II) hydrolysis and precipitation was observed from the beginning of the titration. For Ca (II) and Mg(II) , the free ligand curve and the metal ligand curve overlapped with each other over the entire pH range, indicating lack of metal complex formation. The formation constants for the binary metal complexes were calculated from the potentiometric data with the computer programme SCOGS by taking into consideration the species H_3L, H_2L, HL, L, and ML. The formation constants for the following equilibrium $M + L \leftrightarrow ML$

are listed in **Table-2**. From data in **Table-2** order of stability of metal complexes is Cu(II)>Pb(II)>Ni(II)>Zn(II)>Co(II). Cu (II) complexes are more stable because of Jahn Teller distortion of the metal ion which provide strong four equatorial sites and weak two axial sites. The Pb (II) complexes are considerably stable because of the high affinity between the soft 'S' donor site on the ligand and soft Pb (II) metal.

All the complexes are stable at room temperature and are non hygroscopic. On heating they decompose without melting. The complexes are insoluble in water and are soluble in DMSO and DMF.

Elemental Analysis: The analytical data of the complexes are presented in **Table-3**. It is clear from the table that the theoretical values calculated for the composition shown for each of the complexes are in good agreement with the experimental values. The composition assigned to the complexes may therefore be justified.

4.3 IR Data

The spectra of metal complexes were compared with spectra of pure ligand hCys (B.B Ivanova et al. 2004). Homocysteine showed absorption bands in the range 2300-2800cm^{-1} corresponding to $\nu(NH_3^+)$, a band at 2610cm^{-1} assigned to ν (SH) and two bands at 1680+1620 cm^{-1} ,corresponding to $\delta(NH_2)+ \nu(COO^-)$. The stretching frequencies were compared and illustrated in the **Table-4** for various metal ions. The IR data for the blue copper complex **Fig-5** was compared with free homocysteine spectra. The complexation with Cu (II) ions led to disappearance of the band in the 2300-2800cm^{-1} due to NH_3^+ deprotonation and NH_2 coordination to Cu(II). Coordination to the NH_2 and COO^- groups followed from shift of the bands at 1680 and 1620 cm^{-1} to 1640 and 1610cm^{-1}. The complexation with SH group was observed from the disappearance of

the 2610 cm^{-1} band. The bands ν(Cu-S) at 646cm^{-1} , ν(Cu-N) at 561cm^{-1}, showed the metal coordination in blue complex. ν(Cu-O) bands usually were observed around 340cm^{-1} which we could not record with our instrument. The spectra recorded for nickel complex showed **Fig-6** major absorption bands in the range 1342-1095cm^{-1} corresponding to ν(C-O),a band at 2610cm^{-1} was missing assigned to ν(S-H), predicting the possibility for thiol group coordination with Ni, which is evident for the presence of band ν(Ni-S) at 648cm^{-1} .The decrease in stretching frequency of carbonyl group observed at 1653 cm^{-1} in free hCys to 1575 cm^{-1} in the complex shows that COO^- is coordinated with Ni. The band ν (Ni-N) at 536 cm^{-1}, showed the metal coordination with $–NH_2$ group. In accordance with the literature data these facts indicate a tridentate coordination of hCys to metal Ions. The IR data for the complex [Ni(hCy) (H_2O)] was compared with other spectral techniques (Kazuo Nakamoto ,1978),

4.4 Esr & Mass Spectral Data

The room temperature ESR spectra of blue copper complex in methanol solution showed a single signal **Fig-7**. The three g_x= 2.072, g_y= 2.126, and g_z= 2.188 are similar and show the presence of Cu(II) in an isotropic environment. ESR spectra for the Cu(II) complex could not be obtained at lower temperatures. Further, we were not able to obtain monocrystals of proper size for X-Ray investigation. The EI spectra of [Cu(hCy)(H_2O)] **Fig-8** exhibits molecular ion peak for the mononuclear complex [Cu(hCy)(H_2O)] at m/z=218. (M+He), peaks at m/z=222 is due to Sulphur isotopes

4.5 Electronic spectra

The electronic spectra of [Cu(hCy)(H_2O)] and [Ni(hCy) (H_2O)] are shown in **Fig-9,10**. [Cu(hCy)(H_2O)] showed three peaks around 15,500; 17,710 and 22,200 cm-1 **Table-5** that have been assigned respectively to the transitions $^2B_{1g} \rightarrow {}^2A_{1g}$; $^2B_{1g} \rightarrow {}^2A_{1g}$ and $^2B_{1g} \rightarrow {}^2E_g$ (S. N. Bolotin et al. 2009). The Ni(II) complex of hCy showed two peaks one at 18,900 and the other at 27,350 cm-1. The complex was found to be diamagnetic (Vijayalakshmi M. / IJPS 2019; 15 (3):29-40). Further, it is reported that the diamagnetic square planar Ni(II) complexes do show an absorption band of medium intensity in the region 16,662 - 22,220 cm-1. In view of these observations the peak appearing around 18,900 cm-1 in the present complex has been assigned to $^1A_{1g} \rightarrow {}^1A_{2g}$. One of the transitions proposed for square planar Ni(II) complex(W. Roy Mason, and Harry B. Gray (1968) and the other peak appears at 27,350 cm-1 may be due to charge transfer. The three transitions obtained for [Cu(hCy)(H_2O)] and two transitions for [Ni(hCy)(H_2O)] are compatible with tetrahedral and square planar geometries.

4.6 X-Ray Photoelectron Spectral Data

4.6.1 XPS DATA of Cu(II) complex: The whole spectrum of the complex recorded **Fig-11(a-f)** and list of binding energies are given in **Table-6** showed the photoelectron lines for Cu ($2p_{3/2}$ and $2p_{1/2}$), C (1s), O (1s), N (1s), and S (2p). The binding energy values of Cu $2p_{3/2}$ observed at 934.6eV and 953eV, predicts copper in Cu(II) state, the higher in shift compared to the literature data is due to oxygen environment and the Cu-O bond present in the complex which is stronger increasing the Cu binding energy values. Two peaks for O1s B.E are observed at 531.925eV and 533.801eV. The more intense peak at 531.925eV can be correlated with oxygen B.E in a metal environment.. This is in agreement with Cu peaks observed at 934.6eV. Thus the B.E values for Cu are effected by O environment. The O 1s peak at 533.801eV correlates with literature data of O in H_2O molecule. The three main peaks of 1s of C are observed at a binding energy values of 284.638 eV, 286.706 eV and another one around 289.130 eV. The B.E 284.638 eV is due to C-C bond, the B.E 286.706 eV is due to C-S bond and the peak at 289.130 eV is due to C-N bond present in the complex. The peak for carbonate moiety is less intense and the difference in B.E values for C-N and -CO_2 being less are obtained as broad peak in the overall spectrum recorded for C in the complex. The main peak of 2p of S is observed at 168.517ev. The shift in value of 3 eV is compared with respect to sulphur B.E value 165.110eV of free Cysteinemonohydrochloride compound. The increase in binding energy value can be attributed to Cu coordination with sulphur of homocysteine and thus Cu-S bond formation can be predicted in the complex of [Cu(hCy)(H_2O) complex. The B.E value of N 1s in free cysteinemonohydrochloride is observed at 401 eV, the similar peak in Cu-hCy complex is observed at 399.946 eV, the shift of ~1.0 eV to the lower side can be explained due to decrease in electron density on nitrogen atom and this decrease can be explained due to formation of coordinate bond between Cu and N in formation of Cu-hCy complex. (Appendix)

4.6.2 XPS DATA OF Ni(II) complex: Surface characterization of [Ni(hCy)(H_2O) complex recorded obtained the photoelectron lines as shown in **Fig-12a-f**

for Ni ($2p_{3/2}$ and $2p_{5/2}$), C (1s), O (1s), N (1s), and S (2p). The two major peaks at 855.901 eV and 873.443 eV are identified for Ni atom B.E. The correlation table for Ni B.E values listed in the Appendix had one line at 855.1 eV for Ni-S environment which is in accordance with 855.901eV observed for the complex recorded. The peaks for C 1s based on the literature available are assigned as 1s B.E 284.582 eV for C-C bond, 1s B.E 287.281 eV for C-S bond, 1s B.E 289.271 eV for C-N bond and a small intense peak of 1s B.E 291.282 eV for carbonate anion. The peak for carbonate anion is more evident in this complex when compared to copper complex showing slight difference in the environment of carboxylate anion in the copper complex to the nickel compound. The B.E energy value is at higher side because of possibility of hydrogen bonding with aquo group attached to Ni and carboxylate oxygen of hCy moiety bonded with Ni with tridentate manner as shown in molecular modelling generated structure of Nickel complex. The tridentate geometry is further confirmed by the peaks observed for N1s at 402eV due to Ni-N bond formation and S2p B.E at 165.110eV due to Ni-S bond formation. The B.E values for S 2p and N1s are compared with cysteine monohydrochloride, expected to present at 163.1eV(S 2s) and 401 eV (N 1s). The major shift in the above B.E values from expected shows the possibility of coordination with metal atom. The B.E of free S in cysteinemonohydrochloride is less. But when sulphur is bound to Nickel ion a strong bond is formed which is evident by high B.E of 165.110eV. The same can be explained with N 1s B.E value. The major peaks in overall spectrum of nickel complex thus showed peaks for Ni-O, Ni-N, Ni-S and Ni-OH_2. (Appendix)

4.7 Thermogravimetric data :

TGA of metal chelates are used to get information about the thermal stability of complexes and decide whether the water molecules (if present) are inside or outside the coordination sphere. Lattice water is lost at lower temperature regions between 60-100^{o}C whereas the loss of coordinated water requires temperature above 100^{o}C. In other words, depending upon the value of the temperature at which water is lost, it can be identified as one of these two kinds i.e. lattice or coordinated water. TGA involves a change in the weight of a compound with an increase in temperature and the data is represented in the form of thermogram which is a plot of weight Vs temperature. DTA involves the measurement of a change in heat content as a function of difference in temperature between the sample and reference compound. The DTA data is represented in the form of endothermic/exothermic peaks. In the present investigation heating rates were suitably controlled at 10 ^{o}C min^{-1} under nitrogen atmosphere, and the weight loss was measured from the ambient temperature upto 1000^{o}C. The TGA curves of [Cu(hCys)(H_2O)] show that the initial mass loss occurring within 100-120^{o}C range is interpreted as loss of one coordinated water molecule. The thermo gram above this temperature (>500 ^{0}C) is horizontal and the final product of decomposition at this temperature region corresponds to their metal oxides (] S. Chandralekha et al. 2014). The Thermogram of [Cu(hCys)(H_2O)] is given in **Fig-13.** Presence of water molecule is further confirmed by the endothermic bands observed in the respective DTA curve in the temperature region where the TGA curves showed loss in weight. In addition to the endothermic bands, the DTA curves of complex also show exothermic bands. These bands appeared at higher temperatures which represent phase transition, oxidation and/or decomposition of the compound. López-Gastélum, K. et al. **2021**.

4.8 Molecular Modelling studies

Metal complexes will adopt the geometry which is having the least energy. Hence Molecular Mechanics calculations were calculated for various possible geometries for the metal complex of homocysteine with a given metal ion. The optimization of geometry and energy values were calculated by molecular mechanics software (System Type- Molecular Mechanical Hamiltonian UFF). For Cu (II) distorted octahedral, square planar or tetrahedral geometry are possible, however Molecular Mechanics calculations showed that for homocysteine Cu (II) complexes tetrahedral geometry is having the least energy **Fig-14**. For Ni (II) octahedral, square planar or tetrahedral geometry are possible. However, the modeling calculations showed that homocysteine complex with nickel showed a square planar geometry which has the lowest energy state **Fig-15**

4.8.1 Molecular docking studies Analysis- Docking interactions of (Cu(hCys)(H_2O) with Cytochrome C oxidase 1 enzyme

Investigations of homocysteine neurotoxicity in rat dopaminergic pheochromocytoma cells, human neuroblastoma cells and primary rat cerebellar granule neurons (Linnebank M et al. 2006) revealed binding of copper to homocysteine for COX deficiency. In

the present work ,the binding affinity of Copper homocysteine metal complex with COX enzyme surrounded by the protein residues were analysed using molecular docking studies. The binding affinity of the copper homocysteine metal complex showed good interaction energies with the proteins active sites and the results were shown in the **Table-7**. The structure of the Copper homocysteine metal complex docked in the active site of Cytochrome C oxidase (PDB_ ID: 5Z62) has been consider for the docking analysis **Fig16a,b**. The Copper homocysteine metal complex is stabilized by hydrophobic and Pi-sigma interactions. The homocysteine molecule is showing alkyl and Pi-alky interactions with Val-373, Leu-358 and His-291 residues respectively. The His-291 residue forms a hydrogen bonding interaction with oxygen atom. The sulphur atom formed Pi-sulphur interaction with His-290 residue. It also shows hydrophobic interaction with Asp-364 residue in the active site. The Cu(2+) chelating action of homocysteine and impairement of COX activity represent novel mechanisms of HCys neurotoxicity is evident from our strong binding values obtained by docking studies supports earlier observations (Xiao, Zuo & Dong et al. 2013). The higher stability constant ($logK_{ML}^{M}$= 15.13) from solution studies shows that copper complexes are more stable with hCy when compared to other similar amino acids The synthesis of copper complexes and spectral studies in present work provided the geometry and chemical structure of Cu(II)& Ni(II) complexes. These studies throw an insight into the active site of metalloenzymes involved in pathological action of oxidative stress mediated by Cu(II). Based on the formation constant data and spectral characterization of copper complexes we propose the possible explanation for hCy induced Alzheimer's disease in **Fig-17**. When copper hCy complex is formed it leads to deactivation of COX enzyme and thus the membrane potential of mitochondria is lost leading to mitochondrial dysfunction and immediate release of cytochrome c from mitochondria, which then triggers the apoptotic pathway Michael etal (2006). In this process Caspase-3 protein is excessively activated and thus leads to DNA fragmentation and cell death. If this process takes place in neurons it leads to Alzheimer's disease. Thus based on the above hypothesis we propose that hCy induces apoptosis by COX inactivation followed by excess activation of Caspase-3 protein and neuronal cell death.

4.8.2 Docking interactions of (Cu(hCys)(H_2O) with Glutathione peroxidase 1

Copper homocysteine complex docked in the active site of Glutathione peroxidase 1 (PDB_ID: 2F8A) . The Copper complex is stabilized by hydrogen bonding, hydrophobic and Pi-sulphur interactions **Fig18a&b**. Homocysteine molecule showed Pi-sulphur interactions with Trp-160 residue. The Arg-179, Arg-180 and Gly-48 residues showed hydrogen bonding interactions with homocysteine molecule. Docking values showed interaction of metal complex with Glutathione Peroxidase 1 enzyme. Our results support that Cu-hCys complexes affect the metabolism of extracellular thiols more than homocysteine alone and inhibited glutathione peroxidase-1 activity and mRNA abundance made (Apostolova MD et al. 2003).

4.8.3 Docking interactions of (Cu(hCys)(H_2O) with SOD1

The primary form of superoxide dismutase is Cu,Zn superoxide dismutase, which is referred to as SOD1. SOD1 is primarily found in the cytoplasm of cells but a small portion is found in the intermembrane space of the mitochondria. A key feature of SOD1 is that it possesses a copper cofactor, which is used to catalyze the superoxide dismutation reaction. The SOD1 protein is a dimer composed of two identical subunits ,these two subunits are oriented so the two active sites are facing away from each other. Each subunit is composed of 151 amino acid residues. These amino acids are arranged in eight β-sheets and three exterior loops. Each subunit contains a copper ion and a zinc ion at the active site. The copper ion acts as an electron transfer center in this catalyst, while the zinc ion serves as a structural scaffold and a contributes to the positive charge of the active site, which attracts the negatively charged superoxide anion. The placement of the active site of this complex as well as the geometry surrounding the copper metal centers are critical for this reaction to occur. The active site of this complex is at the bottom of a channel. The copper ion is exposed at the bottom of this channel to allow binding of superoxide to the copper ion, while the zinc ion is buried within the protein. This funnel shape leading to the active site is very important to the superoxide dismutase function. Superoxide dismutase has a very small active site compared to the entire size of the enzyme. The small funnel shape is selective towards small molecules such as superoxide. In the funnel shaped channel are copper and zinc cations as well as two positively charged hydrophilic amino acids, histidine and arginine. The strong positive charge provided by these amino acids and metal ions attracts

the negatively charged superoxide to the active site where the superoxide can be converted into less toxic substances. (Bakavayev, S et al. (2019); S. Dayal G et al.(2017).

The structure of the Copper homocysteine metal complex docked in the active site of Superoxide Dismutase 1 (PDB_ID: 5YTO) has been consider for the docking analysis.As in Fig19a&b docking interactions show that the Copper homocysteine metal complex is stabilized by hydrogen bonding, hydrophobic and Pi-alkyl interactions. The homocysteine molecule is showing alkyl interaction with His-80 residue. The His-63, Lys-136 residues formed hydrogen bonding interactions with oxygen atoms. The sulphur atom formed interaction with Lys-136 residue. This complex also shows hydrophobic interaction with Asn-65 residue in the active site. From dock results it is clearly evident that copper complex with homocysteine effectively inhibiting the enzyme activity of above enzymes, due to higher levels of homocysteine in blood causing copper to bind with homocysteine at the active site of enzymes leading to inhibition of SOD1& Glutathione peroxidase enzyme activity, increasing homocysteine toxicity by initiating free radical formation Starkebaum G, et al., (1986) and M.C. Mele and E. Meucci (1996).

4.8.4 Docking interactions at DNA

The docking calculations observed that free homocysteine with DNA got less binding score value (5.13) compared to copper homocysteine with higher dock score=(6.13). Homocysteine and its copper complex can bind to DNA via non covalent interactions by intercalative binding ,groove binding or external electrostatic binding. Among these interactions we observed intercalation mode of binding to DNA with homocysteine and as well as copper homocysteine complex **Fig20a&b** Molecular docking results suggested that the interaction between DNA and Copper homocysteine complex is more stable leading to cellular degradation, the DNA binding values may further give supporting evidence for cytotoxicity of homocysteine (Catalina Carrasco Pozo et al. 2006).

5. CONCLUSION

The potentiometric data determined can be useful in understanding the chelating ability of homocysteine with various metal ions. Cu(II)&Ni(II) complexes of homocysteine have been structurally characterized by different physico-chemical techniques. The metal: ligand stoichiometry in all the complexes was found to be 1:1. All complexes of homocysteine are being associated with one water molecule. The complexes are non-electrolytes in DMF. The coordinating behavior of the ligand homocysteine towards the metals was binegative, tridentate, coordinating thorough oxygen of carboxyl group, nitrogen of amino group and sulfur of thiol group. Ni (II) complex of homocysteine is diamagnetic while Cu(II) complex of homocysteine is paramagnetic to the extent of one unpaired electron. The electronic spectral information of Ni(II) exhibits square planar and the Cu(II) complex tetrahedral in geometry. The higher stability constant ($\log K_{ML}^{M}$= 15) of binary copper –homocysteine complex, shows that copper complexes are more stable with homocysteine when compared to other similar biomolecules like cysteine and penicillamine. The formation constant data and spectral characterization of metal complexes throw an insight into the active site of metalloenzymes involved in pathological action of oxidative stress mediated by Cu(II), due to strong chelating ability of copper with homocysteine and inhibiting enzyme activity of SOD1, COX1 and Glutathione peroxidase enzymes. Docking studies support the physiological action of copper mediated homocysteine toxicity leading to unprogrammed cell death i.e., apoptosis and neuronal cell damage. The redox behavior of homocysteine in presence of copper results in oxidative stress leading to cell death.

ACKNOWLEDGEMENTS

I am grateful to the assistance of IICT, Hyderabad. Thanks for technical support for providing spectral data using Mass, TGA and XPES.

Table 1: Dissociation constants of ligand (l) and secondary ligands(a), temp=37.0° c ; μ=0.15 m kno_3

Ligand L or A	pKa	pK2a	pK3a
DL-Homocysteine(O,S,N)	3.63	8.75	9.67
α- Alanine(N,O)	2.38	9.26	--
2-2'-Bipyridyl(N,N)	1.52	5.88	--
1-10 phenanthroline(N,N)	C.D	4.87	--
Oxalic acid(O,O)	C.D	3.74	--
Malonic acid(O,O)	2.67	5.22	--
Pyrochatechol(O,O)	8.96	11.36	--

*** Constants accurate upto ± 0.02 C.D - Completely Dissociated**

Table 2: Formation Constants For Binary Metal Complexes With Ligand (L)-Homocysteine , Temp=37.0o C ; M=0.15 M Kno3

Metal Ion	logKMML
Cu(II)	15.13
Ni(II)	9.17
Zn(II)	8.72
Pb(II)	10.07
Cd(II)	----
Co(II)	6.42

Constants accurate upto ± 0.02

Table 3: Analytical Data Of The Ligand (Hcy) And Metal Complexes

Compound	M.wt	Colour	C Calc	C Exptl	H Calc	H Exptl	N Calc	N Exptl	M Calc	M Exptl
Homocysteine(hCy)	135.19	White	35.54	35.51	6.71	6.69	10.36	10.38	-----	
[Cu(hCy)(H_2O)]	217.76	Blue	22.06	22.05	5.55	5.53	6.43	6.45	29.18	29.15
[Ni(hCy)(H_2O)]	212.92	Brown	22.56	22.55	5.68	5.66	6.58	6.60	27.57	27.55

Calc- Calculated , Exptl- Experimental

Table 4: The Major Bands Assignments Of Ir Spectra Of Dl-Homocysteine And Its Metal Complexes (Cm-1)

	ν (N-H)	ν (S-H)	ν(-CH_2-)	ν (C-S)	ν (C-O)	ν (C=O)	ν (M-S)	ν (M-N)
hCy	3147	2610	2930	744	1325-1250	1653	------	-------
Cu+hCy (Blue)	3244	-----	916	808	1332-1109	1614	646	561
Ni+hCy (Brown	**3**317	-------	2920	800	1342-1095	1575	648	536
Zn+hCy (White)	3275	-------	2916	900	1338-1114	1577	650	569

Table 5: Electronic Spectral Data Of Complexes

Compound	Frequency (cm^{-1})	μeff B.M
[Cu(hCy)(H_2O)]	15,500(v_1); 17,710(v_2); 22,200(v_3)	1.81
[Ni(hCy)(H_2O)]	18,900(v_1); 27,350(v_2)	-----

Table 6: The Binding Energy Values Of Dl-Homocysteine And The Metal Complexes Of Homocysteine (Ev)

	S 2SeV	O1SeV	C1SeV	N1SeV	Cu 2P3/2,2P5/2eV	Ni 2P3/2,2P5/2eV
hCy	163.2 163.1				------	------
Cu+hCy (Blue)	168.517	531.925 533.801	284.638 286.706 289.130	399.946	934.665 954.387	------
Ni+hCy (Brown	165.110	530.076 532.128 533.351	284.582 287.281 289.279 291.282	402.000	------	855.901 873.443

Table 7:_ Docking Results Of Copperhomocysteine Complex At The Enzyme Sites

S.no.	Protein name	Docking score (in kcal/mol)
1	Cytochrome C oxidase	-4.55
2	Glutathione peroxidase 1	-3.10
3	Superoxide Dismutase 1	-3.62

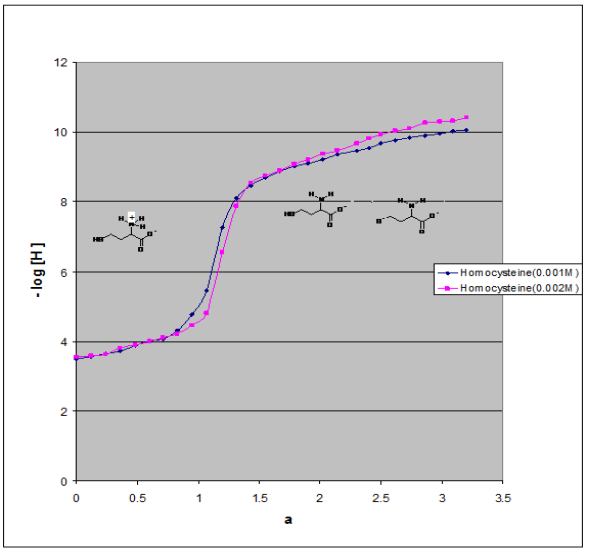

Fig .1: Potentiometric Titration Curve For Free Homocysteine TL = 0.001M; T= 370 C; μ = 0.15 mol dm-3 (KNO3), a = moles of base added per mole of the ligand.

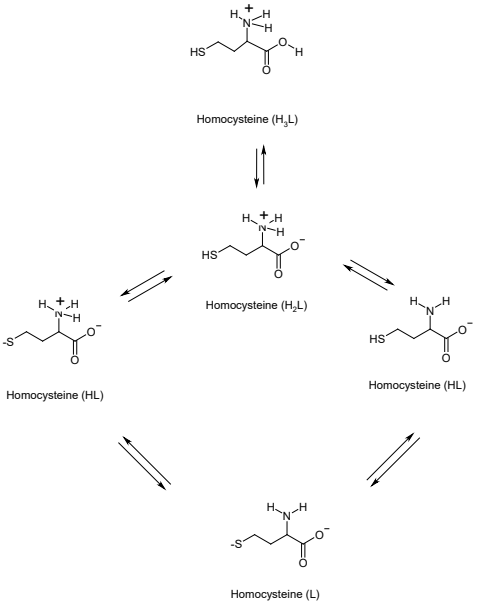

Fig.2: Schematic Representation Of Dissociation Of Homocysteine

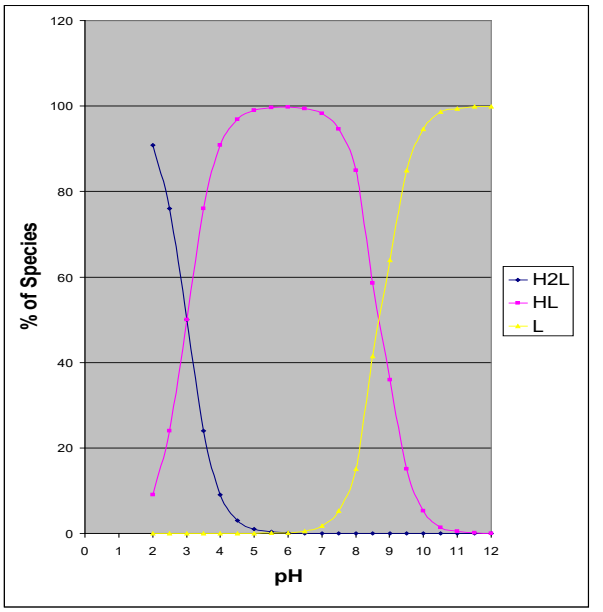

Fig.3: Ph-Species Distribution Profile For Free Homocysteine. Ordinate Represents The Percentage Of A Given Ligand Species As A Function Of The Total Concentration Tl = 0.002 Mol Dm-3 T = 37.00c ; M = 0.15 Mol Dm-3 (Kno3)

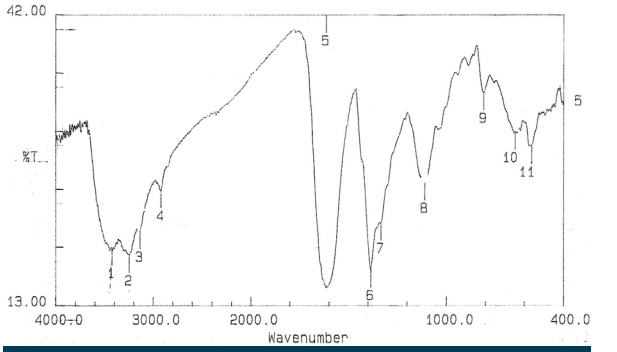

Fig.5: IR- Spectra of [Cu(hCy)(H2O)] Complex

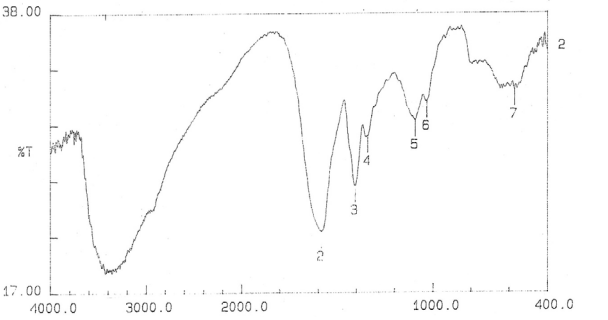

Fig.6: IR- Spectra of [Ni(hCy)(H2O)] Complex

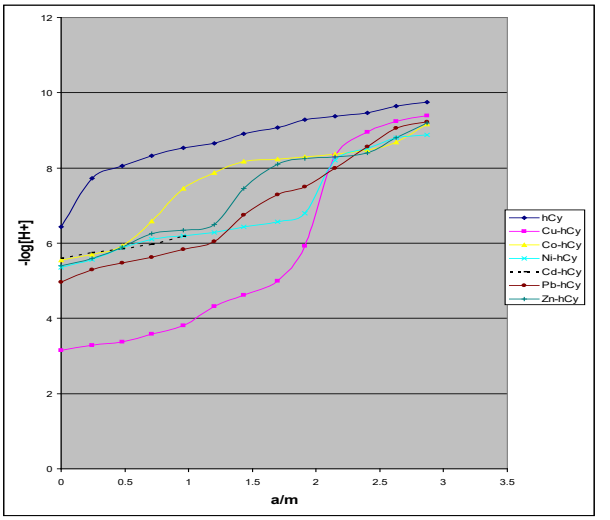

Fig.4: Potentiometric Titration Curves For Free Homocysteine And Metal {Cu (Ii), Ni (Ii), Pb (Ii) , Cd (Ii), And Co (Ii)} In A 1:1molar Ratio Tl = 0.0005 Mol Dm-3 ; Tm = 0.0005 Mol Dm-3 T = 37.00c ; M = 0.15 Mol Dm-3 (Kno3) A = Moles Of Base Added Per Mole Of The Ligand

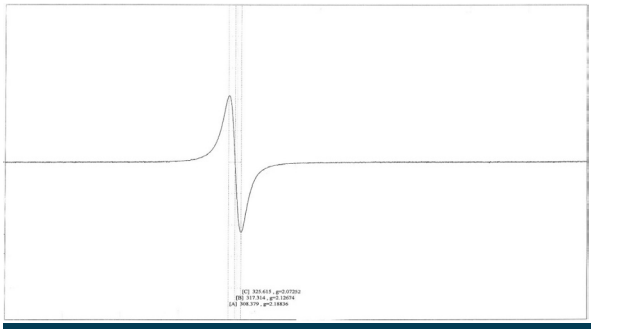

Fig.7: ESR Spectra of [Cu(hCy)(H2O)] complex

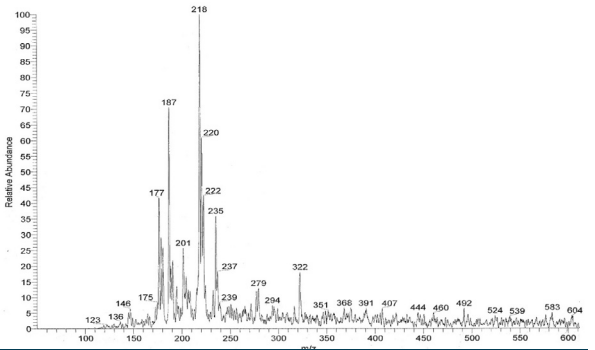

Fig.8: Mass Spectra Of [Cu(Hcy)(H2o)] Complex

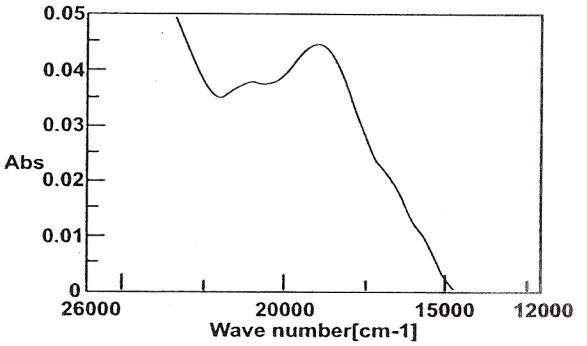

Fig.9: Electronic spectra of [Cu(hCy)(H2O)] complex

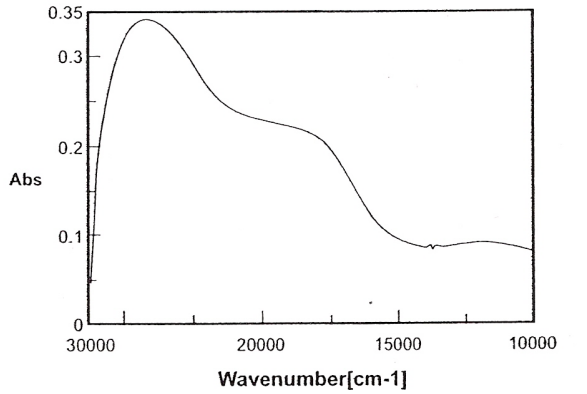

Fig.10: Electronic spectra of [Ni(hCy)(H2O)] complex

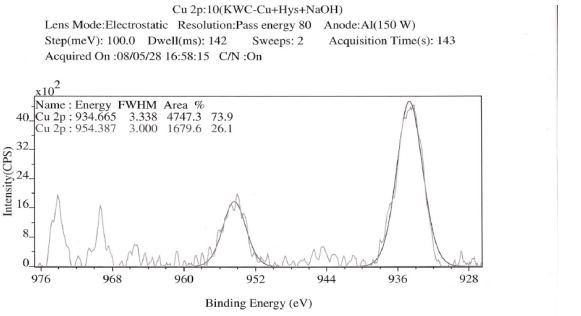

Fig.11a: Xps Spectra For [Cu(Hcy)(H2o)] Complex, B.e Values For Cu (2p) Atom In Copper Homocysteine Complex

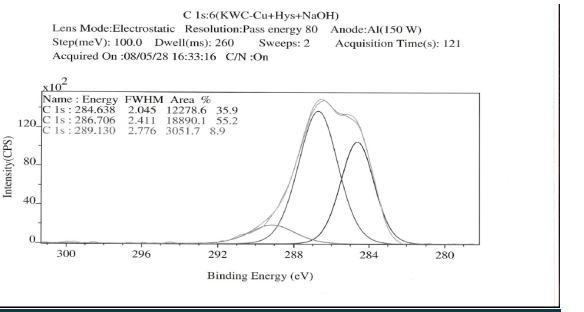

Fig.11b: XPS Spectra for [Cu(hCy)(H2O)] complex , B.E values for C (1s) atom in copper homocysteine complex

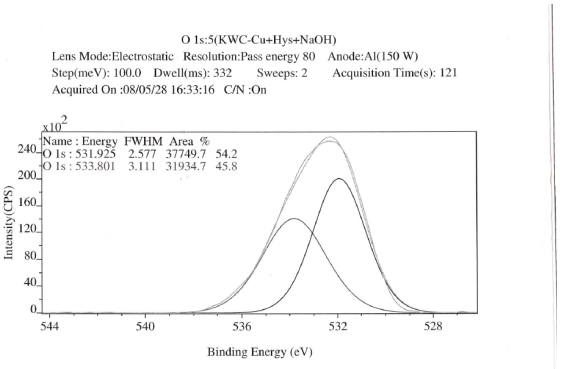

Fig.11c: XPS Spectra for[Cu(hCy)(H2O)] complex, B.E values for O (1s) atom in copper homocysteine

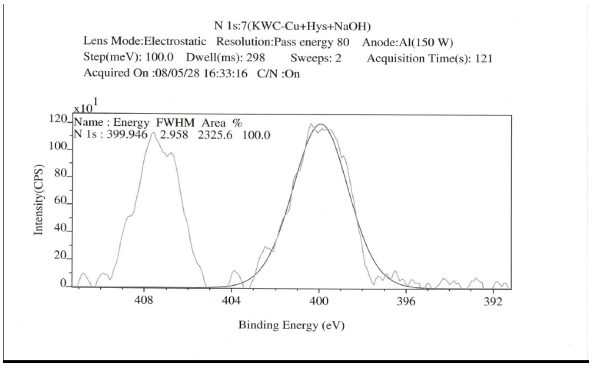

Fig.11d: XPS Spectra for [Cu(hCy)(H2O)] complex, B.E values for N (1s) atom in copper homocysteine complex

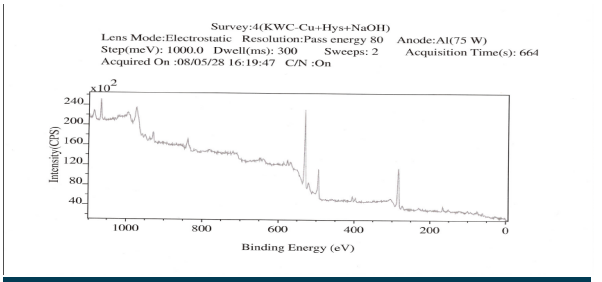

Fig.11e: XPS Spectra for [Cu(hCy)(H2O)] complex, Overall spectra of B.E values of Cu, C, O, N, & S atoms in copper homocysteine complex

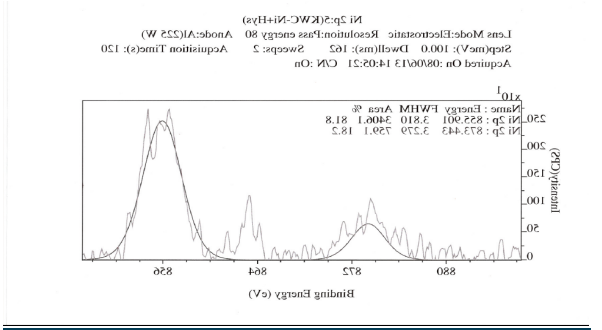

Fig.11f: XPS Spectra for [Cu(hCy)(H2O)] complex, Overall spectra of B.E values of Cu, C, O, N, & S atoms in copper homocysteine complex

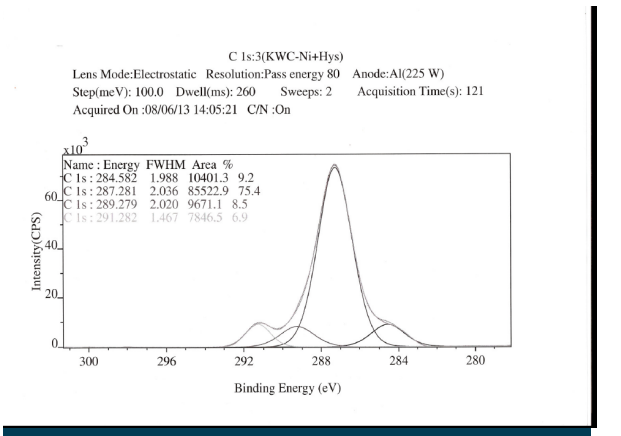

Fig.12a: B.E values for C (1s) atom in Nickel homocysteine complex

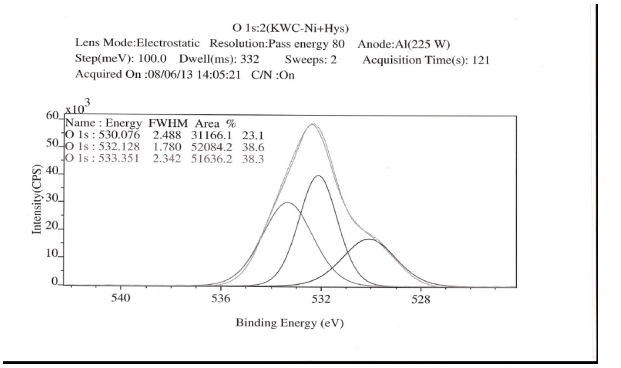

Fig.12b: XPS Spectra for [Ni(hCy)(H2O)] complex, B.E values for O (1s) atom in Nickel homocysteine complex

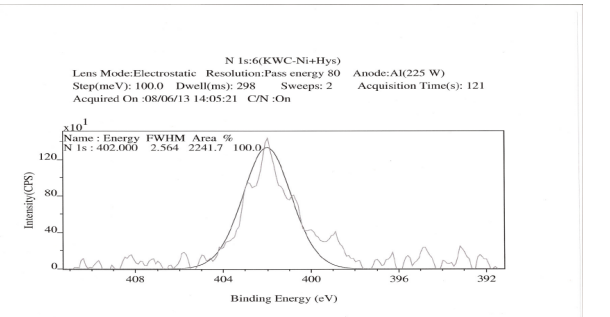

Fig.12c: XPS Spectra for [Ni(hCy)(H2O)] complex, B.E values for N (1s) atom in Nickel homocysteine complex

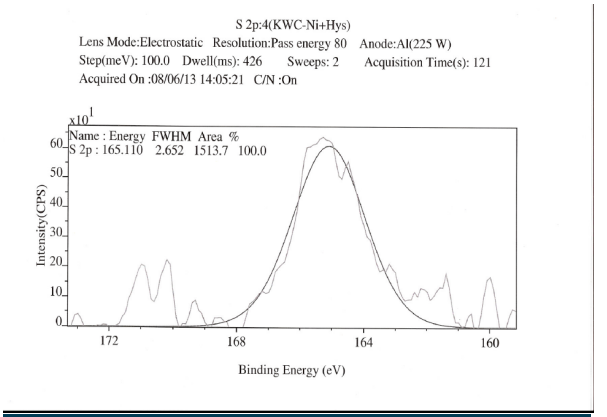

Fig.12d: XPS Spectra for [Ni(hCy)(H2O)] complex, B.E values for S (1s) atom in Nickel homocysteine complex

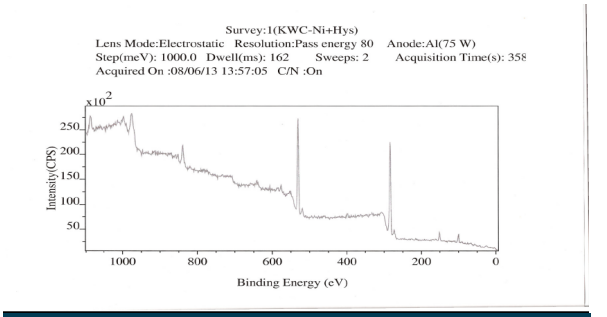

Fig.12e: Overall spectra of B.E values of Cu, C, O, N, & S atoms in Nickel homocysteine complex

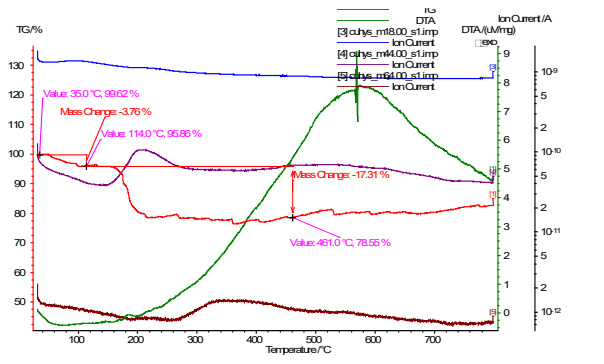

Fig.13: TGA diagram of (Cu(hCy)(H2O)

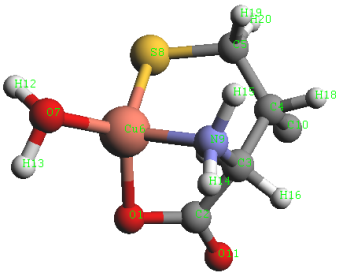

Fig.14: Molecular Modelling structure for copper complex (Cu(hCy)(H2O). The optimization of geometry and energy values were calculated by molecular mechanics software (System Type-Molecular Mechanical Hamiltonian UFF)

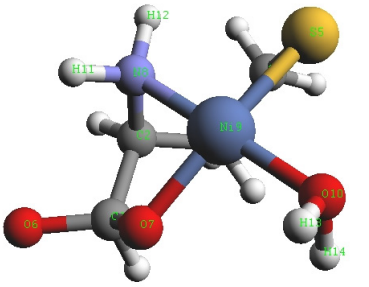

Fig.15: Molecular Modelling structure for nickel complex (Ni(hCy)(H2O). The optimization of geometry and energy values were calculated by molecular mechanics software (System Type-Molecular Mechanical Hamiltonian UFF)

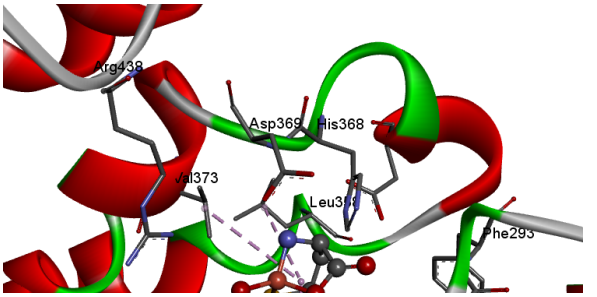

Fig.16a: The Copper homocysteine metal complex docked in the active site of Cytochrome C oxidase. Inhibitor molecule shown in stick style, amino acid side chains are shown in line style and protein shown in cartoon style.

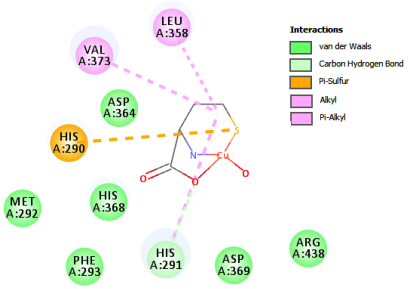

Fig.16b: The Copper homocysteine metal complex docked in the active site of Cytochrome C oxidase. The interactions between ligand and amino residues are shown here.

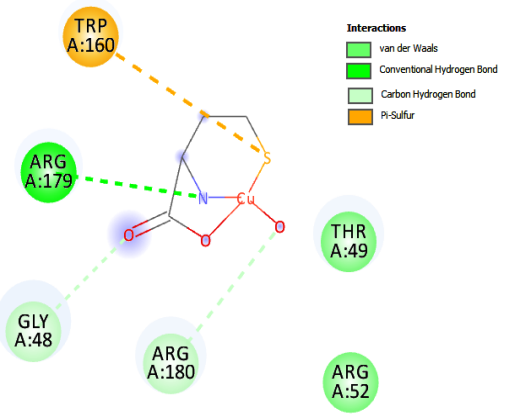

Fig.18b: The Copper homocysteine metal complex docked in the active site of Glutathione peroxidase 1. The interactions between ligand and amino residues are shown here.

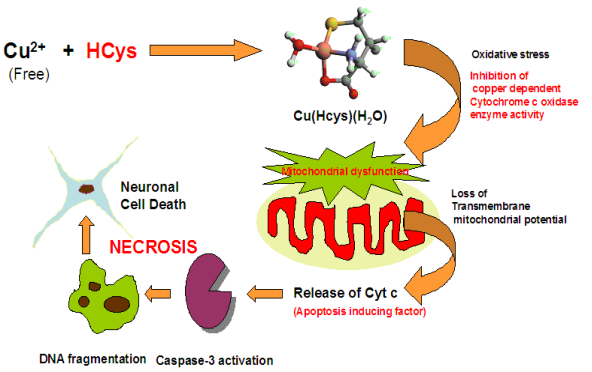

Fig.17: proposed mechanism for Copperhomocysteine complex toxicity

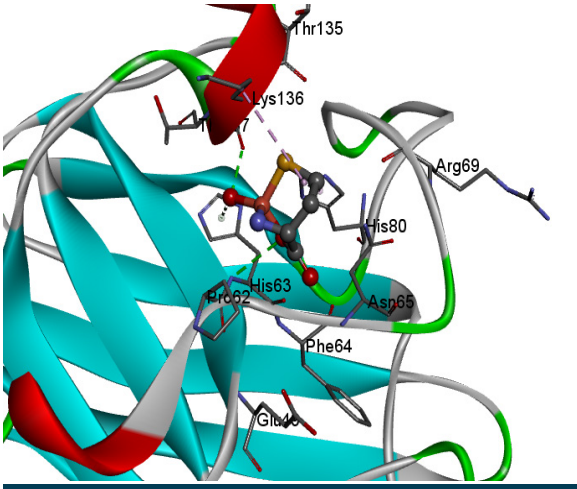

Fig.19a: The Copper homocysteine metal complex docked in the active site of Superoxide Dismutase 1. Inhibitor molecule shown in stick style, amino acid side chains are shown in line style and protein shown in cartoon style.

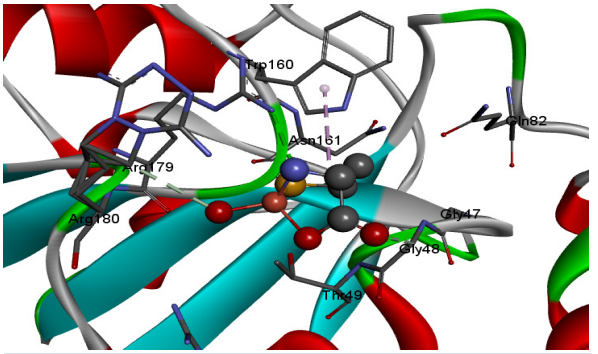

Fig.18a: The Copper homocysteine metal complex docked in the active site of Glutathione peroxidase 1. Inhibitor molecule shown in stick style, amino acid side chains are shown in line style and protein shown in cartoon style.

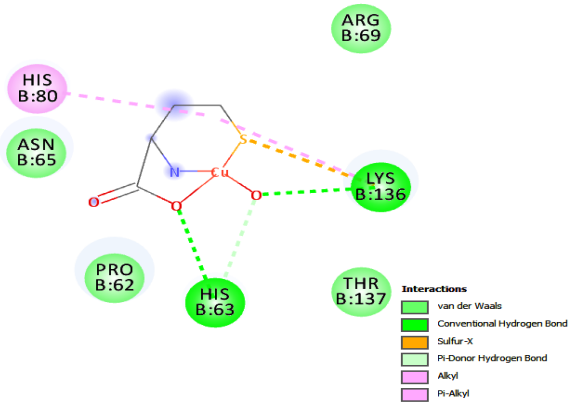

Fig.19b: The Copper homocysteine metal complex docked in the active site of Superoxide Dismutase 1. The interactions between ligand and amino residues are shown here.

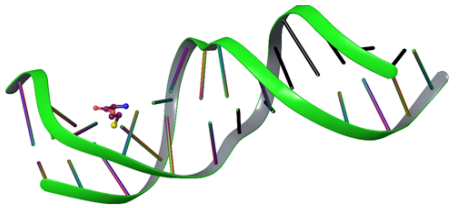

Binding mode of free homocysteine with DNA (Dock score=5.13)

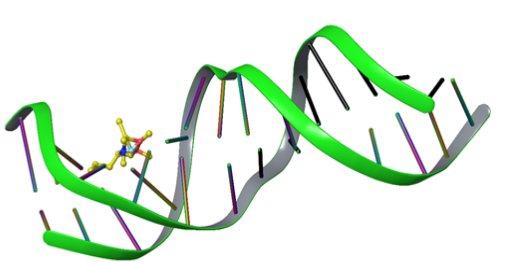

Binding mode of copper homocysteine complex with DNA (Dock score=6.13)

Fig.20a&b: Binding of Copperhomocysteine complex with DNA

REFERENCES

Ahmed, Mahmood & Qadir, Muhammad. 2014. Synthesis of Metal Complexes with Amino Acids for Animal Nutrition. Global Veterinaria. 12. 858-861.

Apostolova M.D., P. R Bontchev , B. B. Ivanova , W. R .Russell , D. R. Mehandjiev , J. H. Beattie, C. K., Nachev. 2003 .Copper-homocysteine complexes and potential physiological actions. J Inorg Biochem. Jul 1;95(4):321-33.
DOI: 10.1016/S0162-0134(03)00133-8
PMID: 12818803

Arunadevi, Alagarraj, and Natarajan Raman. 2020. "Biological response of Schiff base metal complexes incorporating amino acids-a short review." Journal of Coordination Chemistry 73.15 : 2095-2116.
DOI: 10.1080/00958972.2020.1824293

Bakavayev, S., N. Chetrit, T. Zvagelsky Mansour R.,Vyazmensky M., Barak Z., Israelson A., Engel S. 2019. Cu/Zn-superoxide dismutase and wild-type like fALS SOD1 mutants produce cytotoxic quantities of H2O2 via cysteine-dependent redox short-circuit. Sci Rep 9, 10826.
DOI: 10.1038/s41598-019-47326-x
PMID: 31346243 PMCID: PMC6658568

Bertini, I., H. B. Gray, E. L. Stiefel, J. S. Valentine, 2007 J.S. Biological Inorganic Chemistry. Structure and Reactivity; University Science Books: Mill Valley, CA, USA.

Bolotin S. N., E. L. Isaeva, M. H. Shamsutdinova, K. S. Pushkareva, and N. N. Bukov, 2009. Structure of Copper(II) Complexes with 2-[2-Hydroxy-Phenil]-4,4-Diphenyl-1,2-Dihydro4H-3,1-Benzoxazine in Chloroform, Advances in Physical Chemistry Volume , Article ID 365949.
DOI: 10.1155/2009/365949

Catalina Carrasco Pozo,, Alejandro a' lvarez-lueje, claudio olea-azar, camilo lo' pez-alarco' n, and herna' n speisky,2006. in vitro interaction between homocysteine and copper ions: potential redox implications, exp biol med 231:1569-1575.
DOI: 10.1177/153537020623100918
PMID: 17018882

Chandralekha S., G. Chandramohan. 2014. Synthesis, characterization and thermal analysis of the copper (II) complexes with 2,2'-bipyridyl and 1,10-phenanthroline , African Journal of Pure and Applied Chemistry, Vol. 8(10), pp. 162-175.
DOI: 10.5897/AJPAC2014.0592

Dayal S., G. L. Baumbach, E. Arning , T. Bottiglieri , F. M. Faraci , S. R. Lentz.2017. Deficiency of superoxide dismutase promotes cerebral vascular hypertrophy and vascular dysfunction in hyperhomocysteinemia. PLoS One. 2017 Apr 17;12(4):e0175732.
DOI: 10.1371/journal.pone.0175732
PMID: 28414812 PMCID: PMC5393600

Dong D., B. Wang , W. Yin , X. Ding , J. Yu , James Kang Y. 2013 Disturbance of Copper Homeostasis Is a Mechanism for Homocysteine-Induced Vascular Endothelial Cell Injury. PLoS ONE 8(10): e76209.
DOI: 10.1371/journal.pone.0076209
PMID: 24204604 PMCID: PMC3799909

Eichorn G. L., 1973. "Inorganic Biochemistry", Vols. 1 and 2, Ed., Elsevier, New York.

Fan, X., L. Zhang, H. Li, G. Chen, , G. Qi, X. Ma. and Y. Jin, 2020, Role of homocysteine in the development and progression of Parkinson's disease. Ann Clin Transl Neurol, 7: 2332-2338.
DOI: 10.1002/acn3.51227
PMID: 33085841 PMCID: PMC7664283

Farkas, E. & I. Sovago, 2007. Metal Complexes of Amino Acids and Peptides. ChemInform. 38.
DOI: 10.1002/chin.200742251

Ferré-D'., A.R. Amaré, W.C. Winkler 2011. The roles of metal ions in regulation by riboswitches. Met Ions Life Sci.;9:141-73.
DOI: 10.1039/9781849732512-00141
PMID: 22010271 PMCID: PMC3454353

Hughes M.N., 1981."Inorganic Chemistry of Biological processes", wiley,2 nd edition.,

Hultberg, Björn, Anders Andersson, and Anders Isaksson.1997 "The effects of homocysteine and copper ions on the concentration and redox status of thiols in cell line cultures." Clinica chimica acta 262.1-2 : 39-51.
DOI: 10.1016/S0009-8981(97)06531-5
PMID: 9204208

Ivanova B. B., M. G. Arnaudov, P. R. Bontchev, 2004.Linear-dichroic infrared spectral analysis of Cu(I)-homocysteine complex, Spectrochimica Acta Part A: Molecular and Biomolecular Spectroscopy, Volume 60, Issue 4, Pages 855-862.
DOI: 10.1016/S1386-1425(03)00310-X
PMID: 15036096

Kaluđerović G. N., S. Gómez-Ruiz, D. Maksimović-Ivanić, R. Paschke, S. Mijatović. 2012. Metals in medicine. Bioinorg Chem Appl.:705907.
DOI: 10.1155/2012/705907
PMID: 22956920 PMCID: PMC3432323

Katherine J. Franz and Nils Metzler-Nolte 2019 Chemical Reviews 119 (2), 727-729
DOI: 10.1021/acs.chemrev.8b00685
PMID: 30990707

Kazuo Nakamoto , 1978 Infrared and Raman Spectra of Inorganic and Coordination Compounds, Part B

Keskitalo, Salla & Farkas, Melinda & Hanenberg, Michael & Szodorai, Anita & Kulic, Luka & Semmler, Alexander & Weller, Michael & Nitsch, Roger & Linnebank, Michael. 2014. Reciprocal modulation of AÎ²42 aggregation by copper and homocysteine. Frontiers in aging neuroscience. 6. 237.
DOI: 10.3389/fnagi.2014.00237
PMID: 25249976 PMCID: PMC4157544

Ledda C, E. Cannizzaro, P. Lovreglio, E. Vitale, A. Stufano, A. Montana, G. Li Volti, V. Rapisarda. 2019. Exposure to Toxic Heavy Metals Can Influence Homocysteine Metabolism? Antioxidants (Basel). Dec 28;9(1):30.
DOI: 10.3390/antiox9010030
PMID: 31905706 PMCID: PMC7022705

Linnebank M., H. Lutz , E. Jarre , S. Vielhaber , C. Noelker , E. Struys , C. Jakobs , T. Klockgether, B. O. Evert, W. S. Kunz, U. Wüllner. 2006. Binding of copper is a mechanism of homocysteine toxicity leading to COX deficiency and apoptosis in primary neurons, PC12 and SHSY-5Y cells. Neurobiol Dis. Sep;23(3):725-30.
DOI: 10.1016/j.nbd.2006.06.010
PMID: 16876425

López-Gastélum, K.-A.; Velázquez-Contreras, E.F.; García, J.J.; Flores-Alamo, M.; Aguirre, G.; Chávez-Velasco, D.; Narayanan, J.; Rocha-Alonzo, F. Mononuclear and Tetranuclear Copper(II) Complexes Bearing Amino Acid Schiff Base Ligands: Structural Characterization and Catalytic Applications. Molecules 2021, *26*, 7301
DOI: 10.3390/molecules26237301
PMID: 34885882 PMCID: PMC8658810

Manjula, R., G. S. A. Wright, R. W. Strange and B. Padmanabhan. 2018, Assessment of ligand binding at a site relevant to SOD1 oxidation and aggregation. FEBS Lett, 592: 1725-1737.
DOI: 10.1002/1873-3468.13055
PMID: 29679384

Michael Linnebank, Holger Lutz, Eva Jarre, Stefan Vielhaber, Carmen Noelker, Eduard Struys, Cornelis Jakobs, Thomas Klockgether, Bernd O. Evert, Wolfram S. Kunz, Ullrich Wüllner, 2006, Binding of copper is a mechanism of homocysteine toxicity leading to COX deficiency and apoptosis in primary neurons, PC12 and SHSY-5Y cells,Neurobiology of Disease, Volume 23, Issue 3,725-730.
DOI: 10.1016/j.nbd.2006.06.010
PMID: 16876425

M.C. Mele., and Meucci E., (1996) *Amino Acids*, 11, 99-104
DOI: 10.1007/BF00805725
PMID: 24178642

Morris G. M, R. Huey, W, Lindstrom, M. F. Sanner,R. K. Belew, D. S. Goodsell, A. J. Olson. 2009. AutoDock4 and AutoDockTools4: Automated docking with selective receptor flexibility, J. Comput. Chem., 30, 2785-2791.
DOI: 10.1002/jcc.21256
PMID: 19399780 PMCID: PMC2760638

Ozturk Z., D. A. Kose, A. Asan et al.,2014. "Porous metal-organic Cu(II) complex of L-Arginine; 2synthesis, characterization, hydrogen storage properties and molecular simulation calculations," Hittite Journal of Science and Engineering, vol. 1, no. 1, pp. 1-5.
DOI: 10.17350/HJSE19030000001

Rajarajan, Govindasamy & Ezhumalai, Dhineshkumar & Amala, Syawaludin & M. Seenivasan, & A. Paramasivan. 2021. Determination of Stability constants Nickel binary and ternary complexes in aquesous DMSO by Pontentiometric method. Journal of Physics: Conference Series. 1724.
DOI: 10.1088/1742-6596/1724/1/012005

Roy Mason W., and B. Harry. 1968 Electronic Structures of Square-Planar Complexes Gray' Contribution No. 3664 from the Gates and Crellin Laboratories of Chemistry, California Institute of Technology, Pasadena, California 91 109.

Sayce IG. 1968.Computer calculation of equilibrium constants of species present in mixtures of metal ions and complexing agents. Talanta. Dec;15(12):1397-411.
DOI: 10.1016/0039-9140(68)80200-0
PMID: 18960446

Sigel H., Marcell Dekker, 1998. "Metal ions in Biological systems", Ed. Vols. 1 to 25, New York.

Smith, Robert M., J. Ramunas Motekaitis, and E. Arthur Martell. 1985 "Prediction of stability constants. II. Metal chelates of natural alkyl amino acids and their synthetic analogs." Inorganica chimica acta 103.1: 73-82.
DOI: 10.1016/S0020-1693(00)85215-9

Starkebaum, G., and Harlan, (1986) J. M. J. Clin. Ivest., 77, 1370-1376
DOI: 10.1172/JCI112442
PMID: 3514679 PMCID: PMC424498

Vijayalakshmi M, 2019 Synthesis and Characterization of Some Transition Metal Complexes of Schiff Base Derived From 2, 4 - Dihydroxybenzaldehyde; Iranian Journal of Pharmaceutical Sciences, 15 (3):29-40.

Xiao, Zuo & Dong, Daoyin & Sun, Miao & Xie, Huiqi & Kang, Y. James. 2013. Homocysteine Restricts Copper Availability Leading to Suppression of Cytochrome C Oxidase Activity in Phenylephrine-Treated Cardiomyocytes. PloS one. 8.
DOI: 10.1371/journal.pone.0067549
PMID: 23818984 PMCID: PMC3688604

Zong, S., M. Wu, J. Gu, Liu T., Guo R., Yang M. 2018. Structure of the intact 14-subunit human cytochrome c oxidase. Cell Res 28, 1026-1034.
DOI: 10.1038/s41422-018-0071-1
PMID: 30030519 PMCID: PMC6170408

A Survey on Machine Learning Based Keyphrase Generation in Natural Language Processing

Jimmy Jose[1*] and P. Beaulah Soundarabai[1]

[1] CHRIST (Deemed to be University), Department of Computer Science, Bengaluru - 560029, India

***CORRESPONDING AUTHOR:**

Jimmy Jose
Email: jimmy.jose@res.christuniversity.in

ISSN : 2382-5359(Online), 1994-1412(Print)

DOI:
https://doi.org/10.3126/njst.v22i2.85238

Date of Submission: 8 Feb, 2023

Date of Acceptance: 17 Mar, 2024

ABSTRACT

With the exponential increase of available textual data, transforming the natural language content into potential information becomes crucial to assist the prominent application domains. In Natural Language Processing (NLP) applications, keyphrase generation has recently become an increasingly prominent research topic. Even though numerous advancements are realized in the current keyphrase generation models, the proliferation of neural network models profoundly impacted natural language generation to a new era. Over the past several years, various studies on keyphrase extraction and generation have been developed that deliver significant contributions to the current state of keyphrase generation research. The researchers confront understanding the deep insights for further developments from the conventional keyphrase generation research while adopting the deep neural network models. Hence, this work notably focuses on studying the keyphrase generations with the impact of the exploding deep learning methods. This survey briefly introduces keyphrase generation in NLP and reviews the recent abstractive methods using deep learning for meaningful keyphrase generation that achieves state-of-the-art performance. By determining and discussing the shortcomings in the previous machine learning and deep learning-based keyphrase generation, this work facilitates strong groundwork for understanding the recent developments in keyphrase generation. Also, it discusses the research challenges in keyphrase generation from the perspective of both text mining and deep learning models. Thus, this study lays the foundation for the researchers to develop potential solutions to resolve the research constraints in keyphrase generation.

Keywords: Natural Language Generation, Machine Learning, Keyphrase Extraction, Keyphrase Generation, Deep Learning.

1. INTRODUCTION

In recent years, the rapid growth of textual data and the use of deep learning has propelled the field of Natural Language Processing (NLP). NLP is considered a potential field of Artificial Intelligence (AI) to solve computational models and processes to analyze natural languages for real-world problems automatically (Lauriola et al., 2022, Landolt et al., 2021). To be concise, NLP is a technology concerned with interactions between natural human languages and computing devices. Owing to the ubiquitous human-computer interaction, NLP spread its applications as given by Kalyanathaya et al., 2019 in various fields ranging from text summarization and text mining to web search engines, voice assistants, machine translation, robotics, and speech recognition (El-Kassas et al., 2021).

Text generation, formally categorized as Natural Language Generation (NLG), has become a challenging task in NLP that produces a natural language text from the non-linguistic representation of information (Gatt and Krahmer, 2018).Keyphrases are phrases that provide highly-condensed information, which facilitates improving the utilization efficiency in a document. There are two main methods involved in automatic keyphrase generation methods: extraction and abstraction.Several researchers have proposed various keyphrase generation methods and keyphrase extraction methods for the implementation of various NLP tasks (Parida et al., 2021).

Deep learning has significantly impressed numerous areas of NLP involving Recurrent Neural Networks (RNNs), Convolutional Neural Networks (CNNs) proposed by Michelucci, 2022, and several other potential deep neural network architectures (Patel, 2020). Different from these conventional models, deep neural architectures are Generative Adversarial Networks (GAN) and Variational Encoder, which are also used for text generation models, but these models possess a different way of training the network (Lu et al., 2018). Researchers have developed text generation models using Pre-trained Language Models (PLM) to learn semantics and contextual representations of universal languages, which are trained on the large-scale text corpus and tuned for various downstream NLP applications (Li et al., 2021).

Several papers presented keyphrase generation models in NLP. This paper presents a survey of NLP with the aim of deep insights into keyphrase generation using deep learning approaches to assist the researchers in further improving the performance of the keyphrase generation methods. The organization of this paper is as follows. The summary of NLP and its significance with various categories of applications are discussed in Section 2. Section 3 describes the role of keyphrase extraction and Keyphrase generation in NLP and the different keyphrase extraction methods and keyphrase generation. Section 4 reviews various machine learning and potential deep learning-based keyphrase generation methods. Section 5 presents research challenges in keyphrase generation, and Section 6 concludes this work.

2. NATURAL LANGUAGE PROCESSING

The powerful NLP is one aspect of Artificial Intelligence that empowers machines to analyze and comprehend natural language based on computer algorithms and programs. With the advent of natural language content through online and offline processes, NLP plays a crucial role in various application areas by designing different information extraction processes with text mining procedures. It is a potential tool for many organizations to identify powerful insights from comprehending human-generated large data corpus.

2.1 Significance of NLP Approaches

With the emergence of web-based technologies, textual data has had tremendous growth in the form of unstructured or semi-structured data (Hariri et al., 2019). This unstructured or semi-structured data makes searching and analyzing key content information more complex. Thus, it demands automatic information filtering and summarization and the field of NLP has made great progress to resolve this problem (Khurana et al., 2022). NLP components include Natural Language Understanding (NLU), NLG, Speech Processing, Text Mining, and Text Analytics. Among the NLP tasks, Text mining, and Text Analytics, have seen unprecedented growth. Text Mining has gained significant attention in NLP applications, which deal with discovering and extracting a pattern from unstructured natural language text data, and it facilitates classifying documents or clustering the documents into categories (Sebastião et

al., 2022).

2.2 Tasks of NLP

Generally, a sentence in natural language is based on rules, syntax, and semantics, whereas symbols are used to convey the information contained in the text sentence. NLP concerns the machine's ability to understand and generate natural language. NLP methods strongly rely on language linguistics, which studies language, including meaning, grammar, structure, and phrases. Part-of-speech tagging (POS), Stemming, Lemmatization, and Stopword Removal are the generally applied NLP tasks (Lourdusamy and Abraham, 2018).

2.3 Categories of NLP

The broad categorization of NLP includes NLU and NLG, which evolves the task of generating and classifying the text.

2.3.1 The Natural Language Understanding

Natural Language Understanding (NLU) tries to interpret meaning by dealing with common human errors, including mispronunciations or transported letters or words (Otter et al., 2020). To understand and represent the natural language in potential representation, NLP applies different levels of linguistic analysis that assist people in extracting meaning from text or spoken language. The different stages of analysis in processing natural language involve Morphological analysis, Lexical analysis, Syntactic analysis, Semantic analysis, Discourse analysis, and Pragmatic analysis.

2.3.2 Natural Language Generation

Natural Language Generation (NLG) is categorized as a sub-field of NLP aiming at generating a text understandable to human language (Dong et al., 2021). It involves the analysis of the versatility of the language constructs. Based on the context, NLG systems decide to generate the natural language. The instances of NLG are text-to-text generation and data-to-text generation. Text abbreviation, Text translation, and Text expansion are the categorization of text-to-text generation. The task of generating text based on image or video is an application of data-to-text generation. Because of its extremely challenging and promising application prospects, NLG has recently gained more attention among researchers.

3. ROLE OF KEYPHRASE EXTRACTION AND GENERATION IN NLP

Due to the increasing usage of keyphrases, Keyphrase extraction and Keyphrase generation play a significant role in the field of NLP. For a single document, keyphrases serve as a condensed summary, such as an article, enabling the reader to decide quickly whether the article is interesting. The keyphrase prediction model recommends an automatically generated set of representative phrases related to the main topics inherent in a document. Keyphrase prediction is broadly categorized into extraction and generation methods (Nasar et al., 2019).

3.1 Methods in Keyphrase Extraction

Keyphrase extraction is a fundamental step for various tasks of NLP, including document classification, document clustering, and text summarization. Automatic Keyphrase extraction methods determine a group of phrases, also known as 'candidate phrases which are scored and ranked (Alami, et al., 2020). By employing the keyphrase extraction method, the best phrases are selected as a document's keyphrases. Ranked extracted keyphrases are presented in two sets: Single document keyphrases or document collection keyphrases. Keyphrases extraction methods are widely used in NLP, text mining, document mining, information retrieval, and document collection.

3.2 Methods in Keyphrase Generation

Keyphrase generation gives a set of keyphrases in a document, which is an important task in NLP. The main task is to predict keyphrases from the source text automatically. The automatic keyphrase generation model combines the keyphrase extraction and keyphrase generation processes. The domain-independent keyphrase generation approach incorporates the unsupervised keyphrase extraction phase and the keyphrase inference phase to describe and classify the text (DeNart et al., 2014). Several automatic keyphrase extraction methods focused on extracting present keyphrases, the phrases appearing exactly in the

source text. Ignoring the semantics and the underlying context of the content is an issue and cannot generate absent keyphrases that do not appear in the source text (Almutiry, 2020). Several researchers have presented sequential keyphrase generation models to resolve this constraint and generate both the present and absent keyphrases. Supervised and unsupervised methods are the categorization of Keyphrase Generation methods.

Supervised Method: Supervised Keyphrase Generation approaches consider keyphrase generation as a classification problem (Meng et al., 2020). The supervised approach is a learning model trained based on potential features of labelled keyphrases and classifies a candidate keyphrase and not a candidate keyphrase. Moreover, it transforms the keyphrase extraction task into a classification or regression problem.

Unsupervised Method: Domain-independent algorithm, also called an unsupervised algorithm, applies to documents in different domains without needing controlled vocabularies or prior knowledge. In contrast to the supervised approaches, the unsupervised approaches consider keyphrase extraction as a ranking that employs techniques such as clustering as proposed by Nair et al., 2021 or graph-based ranking to determine the keyphrases in the document.

4. IMPACT OF MACHINE LEARNING AND DEEP LEARNING MODELS IN NLP

NLP offers potential means of gaining access to information and facilitates many natural language applications and information retrieval tasks, including text summarization, opinion mining, text categorization, and document clustering (Ibrahim et al. 2019). The major process of machine learning and deep learning models in NLP is categorized into text preprocessing, text representation, model training, and model evaluation. Due to the increased amount of textual information on the web, summarizing the entire information or document along with the main points in the NLP task is critical, so keyphrase extraction and generation methods are essential.

4.1 Review on Machine Learning Approaches in Keyphrase Generation

Different Machine learning approaches include supervised, unsupervised, and reinforcement learning in Keyphrase Generation. The ranking-based keyphrase generation approaches develop machine learning models that determine the keyphrases based on the previously generated key phrases which are relevant and then rank them. The ranking phrase candidates often utilized supervised and unsupervised machine learning features with manually defined features, including **TF-IDF** and **PageRank**. However, these manually annotated features do not determine the significance of each word in the document, leading to inaccurate prediction of the semantics relation among the words underlying the document content. **Naive Bayes**, a supervised machine learning model, employs TF-IDF measurement to predict and classify whether or not the candidate key phrase is the best phrase. Traditional word representation methods, such as a bag of words and one-hot encoding, do not contain semantic information.

To resolve this constraint, the word distribution method as proposed by Le et al., 2014 employs a neural network and maps each word vector to a shorter word vector using the word embedding method. The sentence embedding method is **Sent2Vec**, and the word embedding method is **Word2Vec**. The two classical embedding methods in which Word2Vec maps the entire document and Sent2Vec maps the sentences to vectors that utilize n-gram features to generate the sentence embeddings.

By employing the labelled training knowledge, Supervised machine learning models can automatically generate this mapping process and generates the target text. Hence, supervised classifiers are trained on documents annotated with keyphrases which are useful for determining whether a candidate phrase is a key phrase. **Naive Bayes, bagged C4.5, SVM**, and **maximum entropy** are the different supervised machine learning models widely used to predict and generate keyphrases. Unsupervised machine learning approaches consider keyphrases as a ranking problem, and it performs keyphrase extraction and generation without prior knowledge.

4.2 Review on Deep Learning Approaches in Keyphrase Generation

This section reviews several existing keyphrase generation approaches using different deep learning

models. Most of the existing machine learning-based keyphrase generation methods fail to predict the absent keyphrases and fail to capture the text's semantic meaning.

The research work by Meng et al., 2017proposed the deep keyphrase generation model, **CopyRNN**, by utilizing RNN with copy mechanism and predicting the keyphrases without considering the presence or absence of the keyphrases in the text. Initially, it extracts the semantic and syntactic features using an encoder model with an RNN model for semantic understanding. In subsequence, the copy mechanism in the RNN model predicts the significant word based on the attention of positional and syntactic information in the context, and consequently, it enables the RNN to predict the *OutOfVocabulary* words in the source text. Finally, the decoder model in the RNN learns the significant features obtained from the copy mechanism and effectively generates target keyphrases in a text. Even though this work considers the semantic meaning, it fails to predict correlation among the target keyphrases.

The **Title-Guided Network (TG-Net)** model by Chen et al., 2019 utilizes the input as source context with title and generates the keyphrases based on the analysis of the title-influenced words in the document using the encoder-decoder architecture. It provides equal importance to the document's title while extracting the keyphrases from its main body. Initially, the encoder model in the TG-Net learns the input as source context input and title input and generates the title-guided context representation through the sequence of three embedding layers. Then, the attention-based decoder model in the TG-Net learns the highly summarized information extracted from the encoder module and effectively generates the target keyphrases of the text. Even though seq2seq models have achieved superior performance on keyphrase generation task, seq2seq models are inappropriate for large-scale unlabeled samples with the lack of labeled information or training knowledge.

To address this issue, the researchers suggested a semi-supervised learning approach by Ye et al., 2018 that utilizes labelled and unlabeled data to generate the keyphrases. It initially tags the synthetic keyphrases extracted from the unsupervised keyphrase extraction methods with the unlabeled documents and combines the tagged unlabeled samples with the labelled samples. Then, by jointly learning, keyphrases and titles of the document are generated. The seq2seq model fails to predict the Out Of Vocabulary (OOV) words without considering the correlation among the generated keyphrases.

To handle this, the **seq2seq RNN** model incorporates a copy mechanism, attention mechanism, and coverage mechanismas proposed by Zhang et al., 2018for predicting the key phrases and generating the highly correlated keyphrases based on semantic information. The proposed model constrains the OOV issue through the copy mechanism and generates the highly correlated keyphrases based on the analysis of the relation between the generated keyphrases with the assistance of the coverage mechanism in the model.

To resolve the constraint of generating too few keyphrases, researchers presented a **reinforcement learning approach** by Chan et al., 2019, to generate adequatekey phrases from the basis of the adaptive reward function. It incorporates a Wikipedia knowledge base to detect name variations of the keyphrases and generates accurate keyphrases.

To automatically extract multiple keyphrases from Twitter-like sites, the research work by Zhang et al., 2016 proposed a **joint-layer RNN** model which combines keyword ranking, keyphrase generation, and keyphrase ranking. The joint-layer RNN model comprises two hidden layers and two output layers for processing the keyword ranking and keyphrase generation task.

The research work by Zhao et al., 2019 presented a parallel Seq2Seq model called **ParaNet** with the coverage attention mechanism to address the generation of overlapping keyphrases issue. It employs a word encoder and tag encoder in the ParaNet on the source side and a multi-task learning with POS tags for words on the target side to generate key phrases. The encoder in the ParaNet learns the semantic representation of the words in the source text. While the decoder in the ParaNet model comprises a keyphrase decoder that generates the keyphrases, and the POS tag decoder predicts the POS tags of words in keyphrases. Moreover, this work enhances the keyphrase generation performance through linguistic constraints of keyphrases in the Seq2Seq network and multi-task learning framework.

The **Sentence Selective Network (SenSeNet)** model by Luo et al., 2020 avoids the constraints of generating keyphrases from unimportant sentences using end-to-end training through the straight-through estimator and sentence selection module through weak supervision. Initially, it extracts the features by employing the bi-GRU model and subsequently selects the significant sentences through CNN in the sentence selection module, which learns the significant features and generates the sentence representation. Finally, the work generates the keyphrases based on estimated sentences related to keyphrases obtained from the selection model.

The research by Zhu et al., 2020 employed an encoder-decoder model with a copy mechanism called **CopyNet** to generate keyphrases byanalyzing semantic and significant information in the source text. Initially, this work automatically builds the keyphrase semantic web to extract more related information for source text and to improve the keyphrase generation performance. Based on the attention mechanism, it extracted the source text's potential information with the semantic web's assistance and effectively generated the keyphrases of the source document.

Table 1 compares the conventional keyphrase generation approaches with their advantages and limitations.

Table 1: Comparison of the Conventional Keyphrase Generation Approaches

Author Name and Year	Learning Model	Objective	Algorithm	Advantages	Limitations
Le et al. (2014)	Machine learning	To produce the distributed representation of the input sequence with variable length	Unsupervised model, Paragraph Vector	A neural network maps the word vector to a shorter word vector from training.	Lacks to support the generation of the keyphrases with parsing on complex sentences.
Menget al. (2017)	Deep learning	To analyze the semantic meaning of the keyphrase generation using a copy attention mechanism	Recurrent Neural Network and Copy RNN	It predicts the absent keyphrases	Needs to focus on discontinuity in the sentences
Chen, et al. (2019)	Deep learning - Title Guided Network	To generate keyphrases in a document through title-influenced words.	Encoder-Decoder architecture	It provides the importance of the document's title while extracting keyphrases from the source document.	Fail to rely on simple statistics or rules to yield good results.
Ye et.al (2018)	Deep learning	This model uses labeled and unlabeled data for generating the keyphrases.	Semi-supervised learning	It generates keyphrases for new data.	Lack of nonlinear uncertainties problem
Zhang and Xiao (2018)	Deep learning	To generate OOV words and highly correlated keyphrases throughpotential information of the document.	Seq2Seq model	It enhances the information with the help of GRU	Gold-standard keyphrases are inadequate to validate the keyphrase generation
Chan et al. (2019)	Deep learning	To generate accurate and adequate keyphrases from large text documents.	Reinforcement learning	It resolves the generation of too few key phrases	Lack of keyphrase boundary leads to ineffective adaptive modeling
Zhang et al. (2016)	Deep learning	To generate accurate keyphrases from a large collection of documents such as twitter sites.	Recurrent Neural Network	It combines keyword and context information.	Fails to focus on the dependencies in the labels

Zhao and Zhang(2019)	Deep learning	To resolve the overlapping keyphrase generation.	Parallel seq2seq network (paraNet)	It utilizes syntactic constraints to prevent overlapping keyphrase generation.	Lack of determining the number of keyphrases leads to the over-generate of keyphrases
Luo, et al.(2020)	Deep learning	To generate the efficient metadata sentence from the documents.	seq2seq network	It resolves the discontinuity problem during keyphrase generation	Fails to predict the absent keyphrase
Zhuet al.(2020)	Deep Learning	To generate keyphrases with an attention mechanism	Encoder-decoder framework	It handles Out-Of-Vocabulary(OOV) problems through semantic web	Lack of keyphrase boundary leads to inaccurate keyphrase generation

5. RESEARCH CHALLENGES IN KEYPHRASE GENERATION

In the NLP, keyphrase generation models have several research gaps, which are presented as follows.

- Lack of analyzing the document's semantic meaning while applying the machine learning methods alone for keyphrase generation results in inaccurate key phrases.
- Supervised and unsupervised machine learning methods fail to predict the absent key phrases during the keyphrase generation process.
- A unique challenge in keyphrase generation is generating multiple target keyphrases during the keyphrase prediction process.
- Models predict inaccurate or incomplete keyphrases if the input sequence data is inaccurate or incomplete.
- Existing Keyphrase generation methods neglect correlation among multiple keyphrases, thus resulting in duplication and coverage issues.
- Overlapping keyphrases have been occurring while applying existing deep learning models, resulting in inaccurate key phrases.
- The neural seq2seq model fails to generate the keyphrases for new data when learning the patterns from the labelled data
- Without adaptively tuning the deep learning model and utilizing the external knowledge source, the keyphrase generation method confronts the generation of the absent keyphrases and the generation of present keyphrases.
- Existing generative models predict multiple keyphrases and the number of keyphrases from the input document but fail to generate accurate and too few keyphrases.

6. CONCLUSION

This survey presented the keyphrase generation methods and techniques for large-size documents in various NLP applications. It enhanced the automatic keyphrase generation methods using prior knowledge and data to predict semantic meaning and absent keyphrases. Keyphrase generation also applied semi-supervised learning algorithms to predict the present and absent keyphrases simultaneously. In addition, it utilized deep reinforcement learning with an adaptive reward to predict the semantic meaning of the absent keyphrases. By discussing the pros and cons, this work enables better directions for future research work in keyphrase generation models.

REFERENCES

AlamiMerrouni, Zakariae, BouchraFrikh, and BrahimOuhbi., 2020. Automatic keyphrase extraction: a survey and trends. Journal of Intelligent Information Systems, Vol. 54, No. 2, pp.391-424. DOI: 10.1007/s10844-019-00558-9

Almutiry,Omar.,2021.AutomaticKeyPhraseExtraction. IEEE, International Conference on Engineering and Emerging Technologies (ICEET), pp. 1-7. DOI: 10.1109/ICEET53442.2021.9659724 PMID: 34512113 PMCID: PMC8421017

Chen, Wang, Yifan Gao, Jiani Zhang, Irwin King, and Michael R. Lyu., 2019. Title-Guided Encoding for Keyphrase Generation. In Proceedings of the AAAI Conference on Artificial Intelligence, Vol. 33, No. 01, pp. 6268-6275. DOI: 10.1609/aaai.v33i01.33016268

Chan, Hou Pong, Wang Chen, Lu Wang, and Irwin King., 2019. Neural keyphrase generation via reinforcement learning with adaptive rewards. arXiv preprint arXiv, pp. 1906.04106. DOI: 10.18653/v1/P19-1208

DeNart, Dario, and Carlo Tasso., 2014. A Domain Independent Double Layered Approach to Keyphrase Generation, In WEBIST (2), pp. 305-312. DOI: 10.5220/0004855303050312

Dong, Chenhe, Yinghui Li, Haifan Gong, Miaoxin Chen, Junxin Li, Ying Shen, and Min Yang., 2021. A Survey of Natural Language Generation. arXiv preprint arXiv:2112.11739.

El-Kassas, Wafaa S., Cherif R. Salama, Ahmed A. Rafea, and Hoda K. Mohamed., 2021. Automatic text summarization: A comprehensive survey. Expert Systems with Applications. Vol. 165,pp.113679. DOI: 10.1016/j.eswa.2020.113679

Gatt, Albert, and Emiel Krahmer., 2018. Survey of the state of the art in natural language generation: Core tasks, applications and evaluation. Journal of Artificial Intelligence Research, Vol. 61, pp. 65-170. DOI: 10.1613/jair.5477

Hariri, Reihaneh H., Erik M. Fredericks, and Kate M. Bowers., 2019. Uncertainty in big data analytics: survey, opportunities, and challenges. Journal of Big Data, Vol.6, No. 1, pp. 1-16. DOI: 10.1186/s40537-019-0206-3

Ibrahim, R., S. Zeebaree, and K. Jacksi., 2019. Survey on Semantic Similarity Based on Document Clustering. Adv. sci. technol. eng. syst. No. 5, pp.115-122. DOI: 10.25046/aj040515

Kalyanathaya, Krishna Prakash, D. Akila, and P. Rajesh., 2019. Advances in natural language processing-a survey of current research trends, development tools and Industry applications. International Journal of Recent Technology and Engineering, Vol. 7, No. 5C, pp. 199-202.

Khurana, Diksha, Aditya Koli, Kiran Khatter, and Sukhdev Singh., 2022. Natural language processing: State of the art, current trends and challenges. Multimedia Tools and Applications, pp. 1-32. DOI: 10.1007/s11042-022-13428-4 PMID: 35855771 PMCID: PMC9281254

Lauriola, Ivano, Alberto Lavelli, and Fabio Aiolli., 2022. An introduction to deep learning in natural language processing: Models, techniques, and tools. Neurocomputing, Vol.470, pp. 443-456. DOI: 10.1016/j.neucom.2021.05.103

Landolt, Severin, Thiemo Wambsganss, and Matthias Söllner., 2021. A taxonomy for deep learning in natural language processing. Hawaii International Conference on System Sciences. DOI: 10.24251/HICSS.2021.129

Le, Quoc, and Tomas Mikolov., 2014. Distributed representations of sentences and documents. In International conference on machine learning, pp. 1188-1196.

Li, Junyi, Tianyi Tang, Wayne Xin Zhao, and Ji-Rong Wen., 2021. Pretrained language models for text generation: A survey", arXiv preprint arXiv:2105.10311. DOI: 10.24963/ijcai.2021/612

Lourdusamy, Ravi, and Stanislaus Abraham., 2018. A survey on text preprocessing techniques and tools. International Journal of Computer Sciences and Engineering, Vol. 6, No. 03, pp. 148-157. DOI: 10.26438/ijcse/v6si3.148157

Lu, Sidi, Yaoming Zhu, Weinan Zhang, Jun Wang, and Yong Yu., 2018. Neural text generation: Past, present and beyond. arXiv preprint arXiv:1803.07133.

Luo, Yichao, Zhengyan Li, Bingning Wang, Xiaoyu Xing, Qi Zhang, and Xuanjing Huang., 2020. SenSeNet: Neural Keyphrase Generation with Document Structure.arXiv preprint arXiv, pp. 2012.06754.

Meng, Rui, Sanqiang Zhao, Shuguang Han, Daqing He, Peter Brusilovsky, and Yu Chi., 2017. Deepkeyphrase generation.arXiv preprint arXiv, pp. 1704.06879. DOI: 10.18653/v1/P17-1054

Meng, Rui, Xingdi Yuan, Tong Wang, Sanqiang Zhao, Adam Trischler, and Daqing He., 2020. An empirical study on neural keyphrase generation. arXiv preprint arXiv:2009.10229. DOI: 10.18653/v1/2021.naacl-main.396 PMID: 34494393

Michelucci, Umberto, 2022. A Brief Introduction to Recurrent Neural Networks. In Applied Deep Learning with TensorFlow, Apress, Berkeley, CA, Vol. 2, pp. 245-255. DOI: 10.1007/978-1-4842-8020-1_8

Nair, Srikesh Rajesh, G. Gokul, AkshayAntoVadakkan, Aditya G. Pillai, and M. G. Thushara., 2021. Clustering of Research Documents-A Survey on Semantic Analysis and Keyword Extraction. In 2021 6th International Conference for Convergence in Technology (I2CT), pp. 1-6. DOI: 10.1109/I2CT51068.2021.9418197

Nasar, Zara, Syed Waqar Jaffry, and Muhammad Kamran Malik., 2019. Textual keyword extraction and summarization: State-of-the-art. Information Processing&Management,Vol.56,No.6,pp.102088. DOI: 10.1016/j.ipm.2019.102088

Otter, Daniel W., Julian R. Medina, and Jugal K. Kalita., 2020. A survey of the usages of deep learning for natural language processing. IEEE transactions on neural networks and learning systems, Vol. 32, No. 2, pp. 604-624. DOI: 10.1109/TNNLS.2020.2979670 PMID: 32324570

Parida, Upasana, Mamata Nayak, and Ajit Ku Nayak., 2021. Insight into diverse keyphrase extraction techniques from text documents. Intelligent and cloud computing, pp. 405-413. DOI: 10.1007/978-981-15-5971-6_44

Patel, Sanskruti., 2020. A comprehensive analysis of Convolutional Neural Network models. International Journal of Advanced Science and Technology, Vol. 29, No. 4, pp.771-777.

Sebastião, Pais, Cordeiro João, and Jamil M. Luqman., 2022. NLP-based platform as a service: a brief review. Journal of Big Data, Vol. 9, No. 1. DOI: 10.1186/s40537-022-00603-5

Ye, Hai, and Lu Wang., 2018. Semi-supervised learning for neural keyphrase generation. arXiv preprint arXiv, pp. 1808.06773. DOI: 10.18653/v1/D18-1447

Zhao, Jing, and YuxiangZhang., 2019. Incorporating linguistic constraints into keyphrase generation. In Proceedings of the 57th Annual Meeting of the Association for Computational Linguistics, pp. 5224-5233. DOI: 10.18653/v1/P19-1515 PMID: 31854592

Zhang, Qi, Yang Wang, Yeyun Gong, and Xuan-Jing Huang., 2016. Keyphrase extraction using deep recurrent neural networks on Twitter. In Proceedings of the 2016 conference on empirical methods in natural language processing, pp. 836-845. DOI: 10.18653/v1/D16-1080

Zhang, Y. and Xiao, W., 2018. Keyphrase generation based on deep seq2seq model. IEEE Access, Vol.6, pp.46047-46057. DOI: 10.1109/ACCESS.2018.2865589

Zhu, Xun, Chen Lyu, and Donghong Ji., 2020. Keyphrase Generation WithCopyNet and Semantic Web. IEEE Access, Vol. 8, pp. 44202-44210. DOI: 10.1109/ACCESS.2020.2977508

Field Based Seed Germination Technologies for Domestication of Chiraito *(Swertia chirayita)* in Nepal

Tanka Prasad Barakoti[1*], Churamani Bhusal[1] and Jaya Kumar Yadav[1]

[1]Agricultural Research Station (ARS) Pakhribas, Dhankuta, Nepal Agricultural Research Council (NARC)

***CORRESPONDING AUTHOR:**
Tanka Prasad Barakoti
Email: tpbarakoti@yahoo.com

ISSN : 2382-5359(Online), 1994-1412(Print)

DOI:
https://doi.org/10.3126/njst.v22i2.85239

Date of Submission: 1 Oct, 2023

Date of Acceptance: 8 Aug, 2025

ABSTRACT

On-station and on-farm multi-location experiments were conducted at Agricultural Research Station, Pakhribas and its outreach sites on the high value wild medicinal herb Chiraito (*Swertia chirayita* (Roxb. ex Fleming) Karsten in order to develop seed germination technologies for the hill regions of Nepal. Germination researches were conducted at 4 sites located at 1800-2200 m above mean sea level for 3 years under various growing environments: treating with acid, warm and normal water, mixing with dung slurry and moist soil under nursery, cultivated and virgin land, and meadow and terrace riser conditions. Minute seeds of Chiraito 1g m-2 after treatment were mixed into 1 tea glass of sand/soil and sown/broadcast on nursery bed. Five experiments were laid out in randomized complete block and one in Latin square design with 3 to 6 treatments and 2 to 5 replicates. Plot size was 1m x 1m for each treatment. Germination started after 2 weeks, and proceeded very slowly (continued upto 2-3 months to germinate most seeds). Growth of seedlings was also slow and took 4-5 months (May-August) to reach transplantable 6-8 leaved stage. Varied numbers of emerged seedlings: 250-2000 (grand mean 850) in 1 square meter bed were counted from different trials/ treatments based on locations. Germination achieved higher by soaking seed with water for 24 hours. Improved nursery raising techniques, growing media, cultural practices and direct seeding were tested, verified and found recommendable to the growers for the first time at Agricultural Research Station Pakhribas.

Keyords: *Swertia chirayita*, Propagation, Nursery raising, Seedling technology, Seed germination

1. INTRODUCTION

Nepal is rich in plant resources. Over 5,309 species of flora are identified under 1,515 genera and 193 families (Rajbhandari et al. 2017). Of them 1624 species (> 30%) belong to medicinal and aromatic plants (MAPs) only. These include a 1515 species of angiosperms, species of gymnosperms 19, 56 species of pteridophytes, 5 species of bryophytes, 18 species of lichens and 1 species of fungi (Shrestha et al. 2000). Genus *Swertia* only enumerates 31 species of which *Swertia chirayita* (Roxb.) ex H.Karst. *syn.* S. *chirata* Buch.-Ham. ex Wall. is the medically and economically most important species. It is commonly known as Chiraito in Nepal however the name varies based on locations and ethnicities as Pothi chiraito, Kali chiraito, Lekh tite, Chireto etc. (Barakoti 2004a). Another species (*Swertia angustifolia* Buch.-Ham. *ex* D.Don) called *Bhale chiraito* is less bitter. Chiraito is called Kirata/Chirata in Sanskrit, in Hindi Chirayata and in Tibetan Tikta. It has historical, ethno-botanical, commercial and environmental values (Barakoti 2013) for Nepal.

Swertia chirayita grows naturally in the humid mountain region. Endemic to the high hill-alpine region, it is commonly found in between 1500 to 3200 m above mean sea level (amsl), however Bhandari et al. (2019) and Niraula and Kumari (2012) mention 1200 to 3600 m amsl. The more suitable growing condition and elevation for S. *chirayita* found 1800-2700 m amsl in eastern region (Parajuli *et al*. 1998; Barakoti, 2002). This species flourishes well in the areas with high humidity, long monsoon period, less sunshine, more cloudy period. It grows well under drained fertile humus, sandy to silt-loamy acidic soil having PH 4.7-5.8. It prefers slopy, moist place, found growing in the partial shade forest, marginal and pastureland. It grows in all 57 hill districts of Nepal having desirable altitude and favorable agro-eco-climatic conditions (Barakoti 2004).

Swertia chirayita growing abundantly in Nepal hill regions gradually declined in its natural habitat. Khadka *et al.* (1994) firstly reported the situation in the eastern region. Premature harvesting was the main reason behind such decline in natural populations (Parajuli et al. 1998). Therefore IUCN (2000) categorized this species under vulnerable plants group. Animal grazing, forest fire, lack of conservation and cultivation practices were other reasons (Barakoti 2000a; Shrestha *et al.* 2000). Researchers found that there was an increasing interest among farmers and forest users to cultivate Chiraito for increased production and income. But literature on propagation and cultivation was scanty as no research was done elsewhere. Seed germination in the field had been a major constraint felt by stakeholders (Barakoti 1999).

Nepal is rich in *Swertia* species. Of the 150 species recorded globally (Joshi & Joshi, 2008), 31 species are identified in Nepal's hills and mountains where is favorable environment for *Swertia* species (Barakoti 2008), hence high diversity. Chiratas were found and used in Nepal since time unmemorable as mentioned in ancient scriptures. As Nepal's mountain region could be the center of origin of *S. chirayita*, *S. angustifolia* and other *Swertia* species, research should focus on this line to confirm this possibility. Those might be native/endemic to Nepal as there are strong historical evidences: Firstly, its Latinized scientific name *Chirata* came from Sanskrit word *Kirata*. Chi is also pronounced as Ki in English. Nepal's Eastern region was known as Kirata Pradesh (province) before as 29 kings (Yalamber to Gasti) ruled Nepal. The alpine tribe Kiratas have been dwelling in the region since generations. Kirata dynasties ruled Nepal from 900 BC-300 AD (Mahishpal to Lichchhabi) during Sindh civilization. The most valid evidence is the word Chirata (Kirata) which is a generic term in Sanskrit for the people who had territory in mountains, particularly eastern Nepal (Wikipedia: Kirata). In this context, researches should be done on ancient history and nomenclature of S. *chirayita* to validate information.

The definition of Kirata/Chirata is given in Sanskrit, mother language of Nepali, Hindi and others. Kirata and Kiratatikta are mentioned in sacred Vedas, Puranas, Ayurveda, Samhitas, Ramayana etc. In *Bhavaprakashanighantu-Haritakydinighantu* (1926, Herbs Compendium), Chiraito is defined in Sanskrit as: "Kiratatiktah kairato katutiktah kiratakah ..156.., Kandatiktoanaryatikto bhunimbo ramasenakah . Kiratakonyo Naipalah swardhatikto jwarantakah ..157.., Kirata sarako rukshya shitalastiktako-laghuh ." The meanings: The Kiratah's (plant Chiraito) is highly bitter. Its stem is bitter like non-arya's bitter plant. (Its different names are given). It's also like Neem used by Ram's army. Nepal's another semi-bitter Chiraito (*Swertia anguistifolia*) is also fever relieving. Chiraito

is ardent, cool and short time bitter (Barakoti 1999 & 2004).

Economical and Medicinal Importance

Chiraito is an economically important herb of Nepal. It is a good source of cash income for traders, farmers-collectors in the hills where they traded this herb since generations (Barakoti 2000a; Barakoti 2008). However its rampant collection from the natural habitats (forests) as free gift of nature by the increasing human population during past decade, population of Swertia chirayita has been drastically declined (Khadka *et al.*1994; Barakoti 2001). Therefore conservation practices in *citu* and commercial cultivation in the farmland both approach need to follow effectively. Hence awareness creation activities with the participant farmers was also started in the project locations (Barakoti 1999).

Chiraito ranks top five amongst exporting medicinal plants of the country. Nepal's production 350 to 500 metric tons per annum (Barakoti 2001; Hamro Ban 2010) fulfills about 45% of the world's consumption of dry plant per year. Major quantity (about 80%) is exported to India to fulfill demands of Ayurvedic and allopathic drugs manufacturing companies. About 15% is exported to two dozens of Asian, European and American countries, chiefly China, Singapore, Pakistan, Russia, Germany, Kenya etc. Local consumption is less than 5%. Its harvest and export is higher (>70%) from eastern and central regions. Together with *S. chirayita*, little quantity of *S. angustifolia, S. alata, S. ciliata, S. dilatata, S. multicaulis, S. nervosa*, *S. racemosa* and *S. tetragona* species are also traded (Hamro Ban 2010). Edwards (1993) reported that Chiraito traded from Hile and Basantapur alone (Koshi zone) accounted for about 14 million Rupees.

Swertia chirayita has important medicinal properties. Its anthelmintic, hypoglycemic and antipyretic properties are attributed to amarogentin, swerechirin, swertiamarin and other active bitter principles. Chemical constituents of the plant- chiratin, swertirin, gentiopichrin, ophelic acid are not toxic and are water soluble. Bitter principle ranges 1-2.5 %. Many researchers (Joshi & Dhawan, 2005; Bhandari *et al.* 2019) have described its properties. Whole plant is bitter, possesses broad-spectrum Ayurvedic and allopathic medicinal properties (Barakoti 2004a).

Chiraito is used in crude and processed form. It is effective to cure a number of diseases, disorders and ailments: fevers, jaundice, gastritis, de-worming, influenza, headache, diabetes, urinary disorder, skin diseases, malaria, enlarged spleen and liver, catarrh, intestinal spasm, anemia, indigestion. It is gentian substitute, antibiotic, appetizer, bitter tonic (Barakoti 2004; Joshi & Dhawan 2005). Most properties are mentioned in Sanskrit verse (*Bhabaprakash Nighantu* 1926) as: "*Sannipatajwaraswasakaphapittashradahanut* ..158.., Kasashothatrishakushthajwaravrana-krimipranut ." (Mishra 1926). Meanings: Chirata is useful for typhoid fever, asthma, influenza-cough, gallstones, idem-cough, gastritis, swelling, diabetes, leprosy, fevers, skin diseases, wounds and de-worming (Joshi & Dhawan 2005; Barakoti *et al.* 2012).

2. MATERIALS AND METHODS

Numbers of seed germination experiments in Chiraito were conducted employing innovative seed treatment and nursery raising techniques designed by the main researcher (Barakoti 1999, 2000). Research trials and treatments were designed aiming higher germination. Experimental plots were laid out during April to May. On-farm experiments were carried out collaborating with participant farmers. Germination of seed was evaluated and calculated on the basis of emerged seedlings, not on numbers of seeds sown (ca. 30,000 per gram). Emerged seedlings were counted at weekly, fortnightly, and monthly intervals due to slow emergence of seed, but all data are not presented here. Statistical analysis of the recorded data was performed as per one-way analysis of variance (Fisher 1918).

Location: The experiments were conducted at Pakhribas station and its outreach sites in three districts. The details are presented in tabulated form below (Table 1)

Table 1: Details of locations, treatments, sowing dates, elevation of the experiments

Location/ Site	Year	Treatment of Seed	Replicates	Sowing date	Elevation	Design
ARS Pakhribas Nursery, Dhankuta	1999-2000	Soaked into warm water for 24 hrs*	3	April last week.	1850 m	RCBD**
	Soaked into tap water for 24 hrs					
	Refrigerated at 5^0C for 24 hrs					
	Treated by 5% HCl (aq) for 1 hr.					
	Control					
Basantapur outreach site, Terhathum	1999-2000	Soaked into warm water for 24 hrs	3	May 2nd week.	2000 m	RCBD
	Soaked into tap water for 24 hrs					
	Control					
Okhre community forest, Sankhuwasabha	1999-2000	Soaked into warm water for 24 hrs	4	April 20	1950 m	RCBD
	Soaked into tap water for 24 hrs					
	Control					
Chaite community Forest, Basantapur Meadow, Terhathum	2000-2001	Seed sown on tilled land	5	May 3rd week.	2100 m	Latin Square
	Seed soaked into warm water for 24 hrs, Pakhribas practice					
	Seed sown on forest soil					
	Seed sown on barren (virgin) land					
	Control					
Basantapur outreach site, Terhathum	2000-2001	Seed sown on slice-burn terrace-riser with moist soil	2	May 18	2000 m	RCBD
	Seed sown on grass cut terrace-riser with moist soil					
	Seed sown on grass uprooted terrace-riser with moist soil					
	Seed sown on slice-burn terrace-riser with dung slurry					
	Seed sown on grass cut terrace-riser with dung slurry					
	Seed sown on grass uprooted terrace-riser with dung slurry					
Basantapur outreach site, Terhathum	1999-2001	Seed sown in rows on 1 inch (grass root) sliced terrace-riser	3	May 1st wk.	2050 m	RCBD
	Seed broadcast on 1 inch (grass root) sliced terrace-riser					
	Seed broadcast over grass cut terrace-riser					
	Seed broadcast over grass terrace-riser (Control)					

Design: Five field experiments were laid out in randomized complete block design (RCBD) and one experiment at Chaite community forest (CF) was in Latin square design with 5 blocks. The experiments were comprised of 3 to 6 treatments and 2 to 5 replications. Plot size was 1 m x 1 m (1 sq. m) for each treatment.

Nursery establishment: After selecting suitable site, surface soil of 4-5 cm with weeds of the nursery bed was removed (nursery trial in Pakhribas and Basantapur). The beds were filled with virgin sub-surface soil and covered with bamboo planks 10-12 cm wide. Roofing was made with thatch/ plastic sheets to protect the beds from rain and hailstones at all locations except in terrace riser trials. Roofs were removed after 4-6 months when most seeds gave rise seedlings.

Substrate: The substrate of nursery bed was fertile forest soil under Alder/ Uttis (*Alnus nepalensis)* forest, well decomposed farmyard manure and sand. These collected substrates were sieved through a mesh (<5 mm) and mixed at 1:1:1 ratio, then filled with thin (2-3 cm) layer on the top of the bed of nurseries. The substrates were not needed for the terrace riser trials and also in special treatment beds.

Seed rate and sowing: Chiraito seed rate for field germination test was estimated to be appropriate 1 gram per 1 m2 bed/ treatment plot. The seeds were mixed with fine sand to ease sowing/ broadcasting and evenly covering the bed. The mixed proportion of seed and sand was 1g seed in one tea glass sand (approximately 1:100 ratios) for each experimental plot. Then sowing was done on the surface evenly. Both line sowing and broadcasting method used. In an experiment at Basantapur seeds were dressed with moist soil and dung slurry for comparison. Sowing was done during April to May.

Mulching: After seeding mulching of bed with thin layer of local mulch: thatch, wheat/rice straw was done to protect bed, conserve moisture and control weed. Mulch was removed when germination seen after 5-7 weeks. No mulching was done in the terrace riser and in Chaite forest (CF) trial.

Watering: Moisture was found to be a crucial factor for Chiraito. Lack or excess of water in soil affected germination and vigor. Therefore, irrigation was done at 1-2 days interval regularly. Sprayer was used for evenly watering without stirring soil surface.

Weeding: In the initial stage (1-2 months), weed infestation was higher. Weeding was a compulsory practice as weeds grow very fast, can suppress slow growing small Chiraito seedlings. Therefore uprooting weeds by hand pulling was done at weekly interval.

Seed Soaking: Normal tap water was boiled and kept till mild warm while touching. The weighed seeds, 1 g for each plot was put into small pieces of white cloth for each experiment and kept inside room for 24 hours before sowing.

Bed Condition: Nursery in Okhre was established in open and protected forest land. Trial in Chaite was done on the grazing meadow. Here bamboo cottage with plastic roofing was constructed to protect seed-beds (Photo 4). Trials in terrace riser were laid out in the equally heighted risers. Seeds were mixed with moist soil and fresh cow-dung 200 g per 1 g of seed and broadcasted. In other treatments 100 ml of water per plot was added to the dung, stirred properly and the slurry sprayed with bamboo *Pachaka*/broom evenly.

3. RESULTS AND DISCUSSION

3.1 Germination/ Emergence of Chiraito Seed

Germination of Chiraito (*Swertia chirayita*) seeds tested for first time at various locations in eastern hills of Nepal gave encouraging and promising results. The germination was based on emerged numbers of seedlings. Despite fast germination in the lab (within two weeks), seeds in the field condition germinated very slow, continued 3 to 6 months. It might be due to temperature fluctuation at day and night, lack of moisture, soil cover over seed, unevenly matured seeds etc. (Barakoti 2008).

No literature and field experience of *Swertia chirayita* growing was found as no research conducted globally. Our Himalayan range might be the only favorable growing environment for this species. Then technical personnel of forestry and NGOs had opined that Chiraito seeds might not germinate in the field. But present researches proved, it can germinate under on-farm condition. In spite of big variation in germination percentage with locations and treatments, it was encouraging for the farmers to grow chiraito in the hill region (1800 to 2200 m amsl).

Chiraito seeds started to germinate/ emerge after 2-3 weeks of sowing, however the seedling number was few and size was too small. It was confirmed by chewing and testing bitterness. At the age of 1-2 month, 2-leaved, 1-2 cm high tiny seedling were seen and it took more than 3 months to reach transplantable size.

Therefore observations were started after 2 months (Barakoti 2000a). Basnet (2001) had also reported similar pattern of seedlings growth.

3.2 Result of ARS Pakhribas Nursery Trial

The emergence of Chiraito seeds at Pakhribas were counted at weekly intervals after one month. However due to low number, emergence counted at 3 months is presented. It gave 610 to 761 seedlings from 1 g seed sown in 1 square meter (Table 2). Seeds soaked in warmed and normal tap water for 24 hr. had the higher numbers of emergence (740-761) followed by control (712). The lower germination (610-660) was seen in the refrigerated and acid treated seeds. The reason of low germination from refrigerated seed might be less heat and hardening the seed coat by chilling temperature. In case of acid treated seed, acid scarification might have affected embryo to rise up. It was happened in the lab and field condition in the previous research also (Barakoti, 2000). One-way analysis of variance (ANOVA) data showed insignificant results. The overall result indicated that soaking seed in the water is preferable (Barakoti 2008). Representing photos are presented (Photo 1 and 2).

Table 2: Germination of Chiraito seeds at Pakhribas nursery trial, Dhankuta

Treatments	Counted on July 1st week (3 months after sowing)			Mean No.
	Rep I	Rep II	Rep III	
Seeds soaked in warm water for 24 hrs.	567	640	820	740
Seeds soaked in cold water for 24 hrs.	669	789	825	761
Seeds refrigerated at 5^0C for 24 hrs.	560	632	790	660
Seeds treated with 5% HCl for 0.5 hr.	538	613	679	610
Seed not treated (Control)	662	757	718	712
ANOVA result	F-statistic value 1.07		P -value 0.42	

Photo 1: Observing seedling of Chiraito

Photo 2: Nursery raised seedlings of Chiraito transplanted into poly-bag, AARS Pakhribas

3.3. Result of Basantapur Nursery Trial

Counting of emerged seedlings was done four times (July to May). The results showed markedly lower emergence than in Pakhribas for all treatments. Its main reason might be shade of terrace riser and moist bed. The mean germination increased (348-397) in September (Fig. 1) and decreased slightly in November possibly due to chilling weather. Later in May of succeeding year, there was some increment in seed germination for all treatments (446-450 seedlings) at final count. Rise in emergence was possibly due to onset of warm weather and rain after March. Water soaked treatments favored retain more seedlings. The grand means presented (Fig. 1) clearly shows the differences between the dates and treatments. However ANOVA has been missing technically.

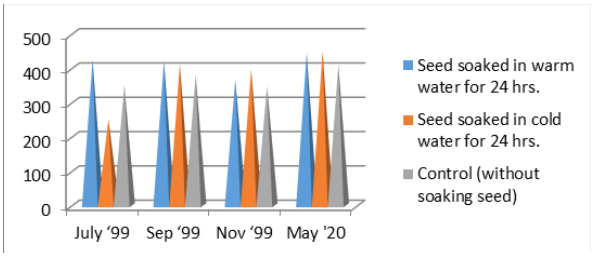

Fig.1: Mean No. of germinated seedlings of Chiraito at Basantapur

3.4 Result of Germination at Okhre community forest (CF) Site Trial

The germination results (Table 3) of Okhre showed longevity in emergence and high differences between initial (July) and final (October) count. Overall treatment means of July was 92 whereas that of October was 716 seedlings. Warm water soaked seed out-emerged (830) over cold water soaked (645) and control (675). The means revealed that soaking seed with warm water for 24 hours had highest emergence (740) as compared to soaking seeds with cold water (566-570) and control treatments (570). The data revealed that special treatment for Chiraito seeds is unnecessary. ANOVA data gave insignificant results. One year old seedlings in the nursery trial is presented (Photo 3)

Table 3: Germination of Chiraito seeds at Okhre CF nursery, Sankhuwasabha

Treatment	Rep-I		Rep-II		Rep-III		Rep-IV	
	Initial Nos. Jul	Final Nos. Oct	Initial Nos. Jul	Final Nos. Oct	Initial Nos. Jul	Final Nos. Oct	Initial Nos. Jul	Final Nos. Oct
Seed soaked in warm water for 24 hrs.	123	617	163	767	191	830	149	745
Seed soaked in cold water for 24 hrs.	81	443	113	567	159	645	122	610
Seed not treated (Control)	72	358	118	588	152	675	144	658
Mean	92	473	131	641	167	716	138	671

Photo 3: Mature seedlings of Chiraito grown at Okhre nursery

3.5 Result of Chiraito germination in Chaite Community Forest Nursery Trial

Emergence of seeds initiated after one month of sowing, counting started after 3 months. Data monitoring was done at monthly interval from July 1 to March 2. Emergence numbers were highest (2119) in August and in March 2 (1556) of the following year from seeds treated with warm water. ,. Emergence was found higher up to November, and then declined gradually (1313-1348) (Table 3). This phenomenon was possibly due to lower temperature during winter months. Grand means of treatments showed 462 seedlings less at final count than first count. There was higher emergence of seeds in all treatments compared to other experiments however no definite trend was followed among the treatments. The final number of retained/ survived seedlings was highest in seeds treated with warm water (1556) followed by those sown on tilled land (1390) and control (1345). The results were encouraging in all treatments (Barakoti 2004a). ANOVA results for Latin Square design are presented (Table 4).

Table 4: Germination of Chiraito seeds at Chaite CF Basantapur site, Terhathum

Treatment	Germinated seedlings counted at monthly interval								
	2000 July 1	2000Aug 2	2000Sep 1	2000Oct 1	2000Nov 2	2000Dec 1	2001 Jan 2	2001 Feb 1	2001 Mar 2
Seed sown in tilled land	1736	1827	1778	1721	1529	1314	1204	1277	1390
Seed soaked with warm water	1982	2119	1987	2058	1957	1557	1326	1304	1556
Seed sown on forest soil	1878	2009	1874	1980	1622	1524	1484	1284	1241
Seed sown on virgin land	1514	1618	1708	1806	1737	1694	1463	1382	1208
Seed not treated (Control)	1743	1745	1802	1858	1639	1537	1447	1321	1345

ANOVA result df=4	MS=5435	F test 0.27 (ns)	Rows=2.95	Columns=13.3
	Colm/Row=1614	Error=20296	F-statistic=1.34	P-value=0.26

Photo 4: Nursery trial at Chaite CF meadow nursery, Basantapur

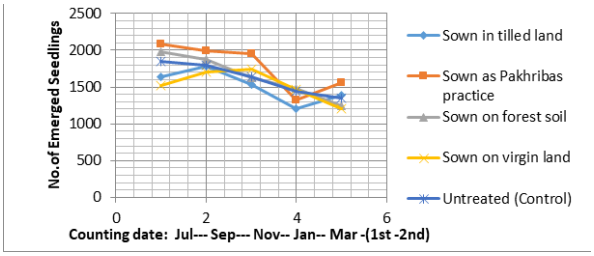

Fig.2: Chiraito germination (bi-monthly) in nursery trial at Chaite CF at Basantapur, Terhathum

The germination data of Basantapur community forest nursery are presented in Fig. 2 below. Emerged seedlings bi-monthly that varied 1204 to 2119. The emergence increased up to third count in November first (1500-2000), then few seedlings died during winter. The number of emerged seedlings rose again in March. Higher number of seedlings survived in the tilled land also (Barakoti 2003).

1. Seed sown in tilled land (green), 2. Seed soaked with warm water (red), 3. Seed sown on forest soil (brown), 4. Seed sown on virgin land (blue) and 5. Seed untreated (Control, yellow)

3.6(a) Result of Terrace-riser Trial at Basantapur Site

Germination of Chiraito seeds tested sowing directly on the terrace riser of cropping land (first year 2 and second year 1) are presented in Table 5. As usual emergence of seed was low at first count in all treatments, it increased in second after 2 months, then at third count the germinated numbers again decreased while passing winter (Barakoti 2003). The means of three dates as grand means varied as: highest (274 seedlings) in the slash-burn plot seed mixing with cow-dung slurry and seed mixing with moist soil (228 seedlings). There was big variation between the treatments although One-way ANOVA gave non-significant result. The emergence data are clearly shown in Fig. 3 as well.

Table 5: Germination of Chiraito at Basantapur, Terhathum

Treatments	Observation dates			Grand mean
	'20.7.2	'20.9.3	'01.4.1	
Slash-burn terrace-riser; seed mixing with moist soil	149	246	113	169
Grass cut terrace-riser; seed mixing with moist soil	232	313	138	228
Grass uprooted terrace-riser; seed mixing with moist soil	162	176	144	161
Slash-burn terrace-riser; seed mixing with dung slurry	248	381	192	274
Grass cut terrace-riser; seed mixing with dung slurry	188	209	121	173
Grass uprooted terrace-riser; seed mixing with dung slurry	219	303	135	219
One-way ANOVA result	F-statistic value 0.66		P-Value 0.63	

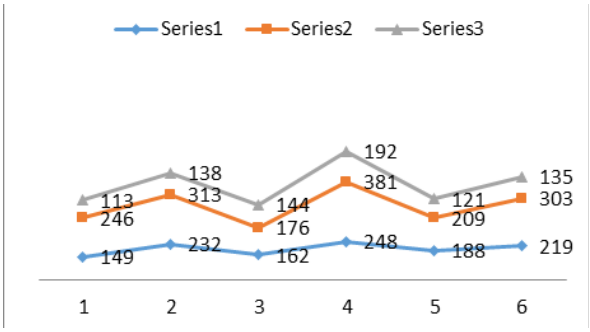

Fig.3: Germination of Chiraito seeds on terrace-riser, Basantapur

Legends: Upper line (green)- Emerged seeds at third count (1.4.2001)

Middle line (red)- Emerged seeds at second count (3.9.2000)

Lower line (blue)- Emerged seeds at first count (2.7.2000)

3.6(b) Result of Terrace-riser Trial at Basantapur

Germination of Chiraito seeds tested in different configured terrace risers but having height 4 feet and replicated 5 times is sown in Table 6, Photo 5. The data highly varied based on replications (91-1315) and treatments. However the treatment means were 512-997 emergence, except in over grass sown plots (119-124). The emergence was more in first counting (August) than the second counting in general due to chilling weather in winter. The emergence was significantly higher in the sliced/ grass cleared terrace riser and in the broadcasted plot than line sowing (Barakoti 2003 & 2004). The Pie chart (Fig. 4) shows clearly the differences among the types of beds and methods of sowing.

Table 6: Comparing germination of Chiraito on terrace risers (means of 5 replicates) before and after winter at Basantapur site, Terhathum

Treatment	Before winter, Nov	After winter, May	Grand mean
Seed sown in row on sliced T-riser	819	512	665
Seed broadcasted on sliced T-riser	997	792	894
Seed broadcasted over grass cut T-riser	631	694	662
Seed broadcasted over grass bed T-riser (Control)	119	124	121

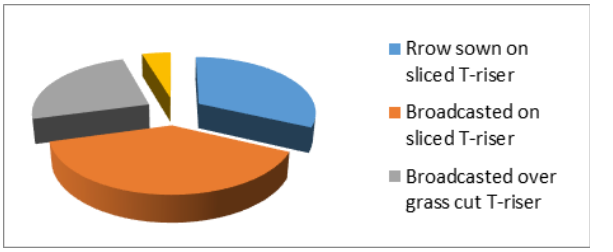

Fig.4: Germination of Chiraito on terrace risers (means) at Basantapur site, Terhathum

Photo 5: Researcher observing Chiraito seedlings in the terrace riser trial at Basantapur

4. CONCLUSION AND RECOMMENDATIONS

Swertia chirayita seed germination results obtained from various field experiments for the first time at ARS Pakhribas, NARC and its outreach sites are promising. The growing methods are easy and affordable to the farmers and commercial growers. The findings are useful to technical personnel and researchers as well. It has been supporting domestication of Chiraito as hill farmers have already adopted this technology for cultivation. However Pradhan and Badola (2011) have conducted germination researches after identification of successful technology from Nepal. It might be due to unavailability of research findings. Following conclusions and recommendations are based on the identified results.

Germination of Chiraito seeds can be seen at two weeks but seedling emergence is very low. Due to slow emergence in the field it takes 3 to 6 months for most seeds to germinate.

Chiraito seeds may germinate under different land conditions and elevations (1800-2200 m amsl). It can germinate and grow in the virgin meadow too.

One gram of seed can produce up to 2100 seedlings (means 1000-1500) in one square meter. But seed must be healthy, mature, pure and fresh.

Special care should be taken in bed preparation, seeding, mulching, irrigating, weeding and protecting from animals and rain.

Chiraito can also be propagated successfully without special seed treatment but soaking seeds in water for 24 hours enhances germination.

The germination is better in the terrace riser than in slightly sliced/ grass cut surface.

The methods and technologies employed here in various experiments for better germination of seed are recommended for domestication of Chiraito.

ACKNOWLEDGEMENTS

The authors would like to acknowledge Hill Agriculture Research Project (HARP) for financial support to the research project on Developing Propagation and Management Techniques for Domestication of Chiraito (*Swertia chirayita*) and station management for logistic support. Thanks are due to the station chief late Mr. P.L. Karna, and station-based staffs for help in implementing and data monitoring of the various experiments.

REFERENCES

Barakoti, T. P. (1999). Chiraito- An Introduction-Chiraito Mala- 1 (Technical Booklet, in Nepali), 33 pp, ARS Pakhribas, Dhankuta, Nepal.

Barakoti, T. P. (2000a). Chiraito to Boost Income. *The Kathmandu Post National Daily / Sunday Post*, Dec. 17, Kathmandu, Nepal.

Barakoti, T. P. (2000b). Germination of Chiretta (*Swertia chirayita*) Seeds Tested through Various Methods under different Conditions in the Eastern Hills of Nepal. In: Proceedings of Nepal-Japan Joint Symposium on Conservation & Utilization of Himalayan Medicinal Resources, held 6-11, 271-278, Kathmandu, Nepal.

Barakoti, T. P. (2001). Developing Propagation and Management Techniques for Domestication of Chiraito (*Swertia chirayita),* Project Completion Report (HARP '98/98), ARS Pakhribas, Dhankuta, Nepal.

Barakoti, T. P. (Ed.) (2002). Proceeding of Chiraito Workshop, 45pp, ARS Pakhribas, Dhankuta, Nepal.

Barakoti, T. P. (2003). Lessons learned from the Experiences of Uptake Pathways of Chiraito Domestication. In: Proceedings on Uptake Pathways and Scaling-up of Agricultural Technologies to Enhance Livelihoods of Nepalese Farmers, 73-81, Kathmandu, Nepal.

Barakoti, T. P. (2004). Attempts made for Domestication, Conservation and Sustainable Development of Chiretta (*Swertia chirayita*), (A Compilation), 162 pp, ARS Pakhribas, Dhankuta, Nepal.

Barakoti, T. P. (2008). Chiretta Technologies -*Swertia chirayita*(Roxb. ex Fleming) Karsten. In: NARC Research Highlights 2002/03-2006/07, 71-72pp, Nepal Agricultural Research Council, Kathmandu, Nepal.

Barakoti, T. P., Tiwari, N. N. & Yonzen, M. (2012). Quality of Chiretta (*Swertia chirayita*) in Cultivated and Wild Samples Collected from Different Districts of Nepal. Nepal Journal of Science and Technology, 13(2), 57-62. *Nepal Academy of Science and Technology*, Lalitpur, Nepal. DOI: 10.3126/njst.v13i2.7715

Barakoti, T. P. (2013). Country Status Report on Medicinal and Aromatic Plants of Nepal. In: Proceedings of Expert Consultation on Medicinal and Aromatic Plants in Asia and the Pacific, (pp…17) held in 2-3 December, Bangkok, Thailand.

Basnet, D. B. (2001). Evolving nursery practices and methods of cultivation of high value medicinal plant *Swertia chirayita, Environment and Ecology,* 935-938.

Bhandari, L., Bista, B. B., Bhatta, M. R., Khanal, C., Khanal, S., Ranjitkar, R. and Bhandari, D. P. (2019). Phytoconstituents, Antioxident and Bitterness Value of Swertia chirayita from Four Different Geographical Regions of Nepal, *J. Plant Res.* 17(1), 104-111.

Edwards, D. M. (1993). The marketing of non-timber forest products from the Himalayas: The trade between east Nepal and India. *Rural Development Forestry Network Paper*, 15b (ODI).

Fisher, R. A. (1918). One-way analysis of variance (ANOVA) of variable biological data.

Hamro Ban. (2010). Manual/Book. Regular publication of the Department of Forest, MoFSC, Nepal.

IUCN. (2000). National Register of Medicinal Plants. IUCN/MFSC, 161 pp., Nepal.

Joshi, K. & Joshi, A. (2008). *Swertia L*. (Gentianaceae) in Nepal Himalaya: Ethno botany and Conservation Status. *Ethno botanical Leaflets 12: 361-372.*

Joshi, P. & Dhawan, V. (2005). Swertia chirayita -An Overview. *Current Science, 89, 635-640.*

Khadka, R. J., Gurung, B. D., Tiwari, T. P., Gurung, G. B., Ghimire, R. P., Adhikari, K.

B. & Shrestha, D. N. (1994). A study on Chiraito, the high altitude cash crop of the eastern hills of Nepal. PAC Working Paper No. 107, Dhankuta, Nepal.

Mishra, B.P. (1926). *Bhavaprakashanighantu-Haritakyadinighantu, Bha. Tee.*

(Herbs Compendium), 34-35pp,. *ShreeVainkteswar* Stem Press, Bombay, India.

Nepal Monarchy: Kirata Dynasty. Wikipedia of Kirata, Google.

Niroula, B. & Kumari, A. (2012). Swertia Chirayita (Roxb. ex Fleming) Karsten Cultivation in Nepal Himalayas: Mini Review. In: Recent Advances in Medicinal Plants and their Cultivation (pp.94-99). First edition, Chapter: 9. Mangalam Publishers, Delhi, India.,

Parajuli, D. P., Gyanwali, A. R. & Shrestha, B. M. (1998). Manual of important non-timber forest products in Nepal. Institute of Forestry/ ITTOP, Nepal.

Pradhan, B. K. & Badola, H. K. (2011). Assessment of seedling emergence and vigor for quality planting material in thirteen populations of Swertia chirayita- a high value endangered medicinal herb, using substrate combinations, *Journal of Medicinal and Spice Plants*, 16 (1), 34-41. DOI: 10.1100/2012/128105
PMID: 22619581 PMCID: PMC3349092

Rajbhandari, S., Siwakoti, M., Rai, S. K. & Jha, P. K. (2017). An Overview of Plant Diversity in

Nepal, In: Plant Diversity in Nepal, (Book, pp 1-15), Botanical Society of Nepal, 2020.

Shrestha, K. K., Tiwari, N. N. & Ghimire, S. K. (2000). Medicinal and aromatic plant database of Nepal. The Himalayan Plants. In: Proceedings of Nepal-Japan Joint Symposium on Conservation and Utilization of Himalayan Medicinal Resources, Kathmandu, Nepal.

Antiurolithiasis, Anti-Inflammatory And *In Silico Docking Studies Of Karpura Shilajit*

N V L Suvarchala Reddy Vanukuru[1*], Mudunuri Ganga Raju[1] and Malkapuram Mamatha[1]

1 Department of Pharmacology, Gokaraju Rangaraju College of Pharmacy, Bachupally, Hyderabad, Telangana, India

***CORRESPONDING AUTHOR:**

N V L Suvarchala Reddy Vanukuru
Email: suvarchalakiran@gmail.com

ISSN : 2382-5359(Online), 1994-1412(Print)

DOI: https://doi.org/10.3126/njst.v22i2.85240

Date of Submission: 8 Feb, 2023

Date of Acceptance: 4 Mar, 2024

ABSTRACT

Urolithiasis is the condition where urinary calculi are formed anywhere within the excretory organ, bladder, and/or ureters. Asphaltum commonly called *Karpura shilajit* is known for different activities like antimicrobial, antidiabetic, antiulcer, fungitoxocity, estrogenic, anti-inflammatory, antihyperglycemic, antilithiatic activity and antioxidant activity. The aim of study is to evaluate anti-lithiatic activity by ethylene glycol ammonium chloride (0.75%) model for 28 days and *in vitro* anti-inflammatory activity by protein denaturation method using the mineral extract where cystone (500 mg/kg, *p.o.*) used as a standard drug in the present study. Preliminary Phytochemical screening resulted in the presence of flavonoids, saponins, carbohydrates, terpenoids and steroids. The Shilajit extract significantly restored creatinine, urea, uric acid, calcium, phosphate, oxalate, sodium and potassium levels in Ethylene glycol ammonium chloride induced urolithiasis model. Histopathological examination further confirmed the induction of lithiasis with crystal deposition in the sections of kidney treated with ethylene glycol-ammonium chloride. The mechanism by which the extract exhibited this effect is possibly through an anti-inflammatory, nephroprotection. *Karpura shilajit* had shown significant effect on urine volume, urine pH, urine excretion, sodium and potassium levels. The steroids, terpenoids and flavonoids isolated from Gas Chromatography-Mass Spectroscopy are docked with prostaglandin synthase inhibitor for anti-inflammation activity and Glycolate oxidase / Lactate dehydrogenase inhibitor. Overall results explain us that *Karpura shilajit* has proven nephroprotective activity by ethylene glycol induced model along with anti-inflammatory activity i.e., by controlling renal stone formation and increasing urine flow and reduction in impaired renal tubules.

Keywords: *Karpura shilajit*, Ethylene Glycol, Antilithiatic, anti-inflammatory, Docking.

1. INTRODUCTION

Lithiasis, often known as calculus, seems to be a disorder wherein acid salts and hard, tiny mineral fragments accumulate in either organ or duct of the body. Renal lithiasis can be defined as the consequence of an alteration of the normal crystallization conditions of urine in the urinary tract. (Grases *et al.* 2006). Nephrolithiasis is responsible for 2 to 3% of end-stage renal cases if it is associated with nephrocalcinosis (Alelign & Petros 2018). In our study lithiasis is induced by ethylene glycol –ammonium chloride model where cystone is the standard drug used. In addition to being uncomfortable as they try to pass through the tissue, the renal caliculi's restricted urine flow may also result in inflammation and increased pressure. Inflammation is the body's first response to infection or injury and is critical for both innate and adaptive immunity (Kany *et al.* 2019). Diclofenac sodium inhibits the enzyme cyclooxygenase (COX). The therapeutic effects of NSAIDs are attributed to the lack of these eicosanoids. Medicinal herbs are moving from fringe to mainstream use with a greater number of people seeking remedies and health approaches free from side effects caused by synthetic chemicals. One such example is the herbal mineral extract called Shilajit. It is widely used in traditional medicinal system of India has been reported to possess antioxidant, anti-inflammatory, memory enhancer and anti-ageing property. It is known as a rich source of humic substances, including fulvic acid (Suvarchala *et al.* 2022). The innumerable medicinal properties and therapeutic uses of Shilajit prove its importance as a valuable medicinal substance (Nareshrao & Talekar 2019). The aim of the study is to evaluate the antilithiatic activity of Karpura shilajit, docking studies of bioactive compounds obtained from GC-MS studies of *Karpura shilajit* and in *silico* ADME analysis of docked compounds by molinspiration to calculate the properties and to predict bioactivity.

2. MATERIALS AND METHODS

2.1 Identification of Chemical Constituents

Selected mineral was screened for the presence of various phytoconstituents like glycosides, alkaloids, terpenoids, volatile oils etc., and also chemical compounds such as carbohydrates, protein and lipids that exert a physiological and therapeutic effect.

2.2 Acute Toxicity Testing

Studies were carried out in order to check the toxic effects of the extract. The study performed as per organization for economic cooperation and development (OECD) to evaluate the acute oral toxicity by up and down procedure. Animal's inbred colony of adult wistar albino rats (150-200 gm) are used for the present study. They were kept in polypropylene cages at 25 ± 2°C, with relative humidity 45- 55% under 12-hour light and dark cycles. All the animals were acclimatized to the laboratory conditions for a week before use. They were fed with standard animal feed and water ad. libitum. All the pharmacological experimental protocols were approved by the IAEC.

2.3 Experimental Protocol

Animal procurement Wistar albino rats (Approx. 150 to 200 g) were procured from Gentox Bioservices, Hyderabad, and present study was carried out in CPCSEA approved animal house of Gokaraju Rangaraju College of Pharmacy, Bachupally, Hyderabad, India (Reg, No. 1175/PO/Re/S/08/CPCSEA).

2.4 In vitro evaluation of Antilithiatic Activity

2.4.1 Homogenous precipitation method

Step-1: Preparation of experimental kidney stones (Calcium oxalate stones) by homogenous preci pitation: Equimolar solution of calcium chloride dihydrate (AR) in distilled water and sodium oxalate (AR) in 10 mL of 2N H2SO4 were allowed to react in sufficient quantity of distilled water in a beaker. The resulting precipitate was calcium oxalate. Precipitate freed from traces of sulphuric acid by ammonia solution. It was washed with distilled water and dried at 60ºC for 4 hours.

Step-2: Preparation of semi-permeable membrane from eggs: The semi-permeable membrane of eggs lies in between the outer calcified shell and the inner contents like albumin & yolk. Shell was removed chemically by placing the eggs in 2M HCl for an overnight, which caused complete decalcification. Further, washed with distilled water, and carefully with a sharp pointer a hole was made on the top and the contents squeezed out separately from the decalcified egg. Then egg membrane washed thoroughly with distilled water, and placed it in ammonia solution, in the moistened

condition for a while & rinsed it with distilled water. Stored in refrigerator at a pH of 7-7.4.

Step-3: Estimation of calcium oxalate by Titrimetry: weighed exactly 1 mg of the calcium oxalate and 10 mg of the extract/compound/ standard and packed together in semi evaluation permeable membrane by suturing. This was allowed to suspend in a conical flask containing 100 mL 0.1M TRIS buffer. One group served as negative control (contained only 1 mg of calcium oxalate). Conical flask, of all groups in an incubator, preheated to 37°C for 2 h, for about 7-8 h. The contents of semi-permeable membrane from each group were removed into a test tube. Added 2 mL of 1N sulphuric acid and titrated with 0.9494N KMnO4 till a light pink colour end point obtained.

1 mL of 0.9494N KMnO4 = 0.1898 mg of 4 Calcium

The amount of undissolved calcium oxalate was subtracted from the total quantity used in the experiment in the beginning, to know how much quantity of calcium oxalate actually dissolved the test substance(s) (Suvarchala *et al.* 2021).

2.5 In vitro Evaluation of Anti-inflammatory Activity

2.5.1 Protein denaturation Assay

2.5.1.1 Preparation of reference drug (positive control)

NSAID (Diclofenac sodium) was used as reference drug. It was crushed into fine powder. About 0.2 g of drug powder was measured using a digital analytical balance (Shimadzu corporation, Japan) and was added to 20.0 ml of distilled water. The solution was mixed well using a vortex.

2.5.1.2 Serial dilutions

Serial dilution from 1000 µg/ml to 0.01µg/ml was performed for shilajit and for reference drug (Diclofenac sodium). All samples contained 5.0 ml of total volume. Reaction mixtures were prepared using 2.8 ml of phosphate-buffered saline (pH 6.4) and 0.2 ml of egg albumin (from fresh hen's egg). Then 2 ml of extract from each different concentration were mixed gently with reaction mixtures. A similar procedure was used for reference drug (Diclofenac) and they were used as positive controls for this study. In addition, distilled water was used as negative control.

2.5.1.3 Inhibition of protein denaturation

Reaction mixtures were incubated in a water bath at 37°C ± down 2°C for 15–20 min, and later, it was heated at 70°C at which the reaction mixture was maintained for 5 min. Then, the reaction mixture was allowed to cool at room temperature for 15 min. Absorbance of reaction mixture before and after denaturation was measured for each concentration (1000 µg/ml, 100µg/ml, 10µg/ml, 1 µg/ml, 0.1µg/ml and 0.01µg/ml) at 680 nm using a colorimeter. Each test was repeated thrice and the mean absorbance was recorded. The percentage of inhibition of protein was determined on a percentage basis with respect to control using the following formula (Raju et al. 2018).

$$\text{Percentage inhibition (\%)} = \frac{\text{Absorbance of control} - \text{Absorbance of test}}{\text{Absorbance of control}} \times 100$$

2.6 In vivo Evaluation of Antilithiatic Activity

2.6.1 Ethylene glycol – ammonium chloride induced urolithiasis

2.6.1.1 Experimental animal groups

The animals are divided in to five groups containing six animals in each group. Group I is Control received (0.5%) gum acacia, Group II (Disease control group), III (*Karpura shilajit* (100 mg/kg), IV *Karpura shilajit* (200 mg/kg) & V cystone (500 mg/kg) received 0.75% v/v ethylene glycol for 28 days and 1% w/v ammonium chloride for first 3 days in distilled water additionally Group III received *Karpura shilajit* (100 mg/kg, bd. wt, p.o) for 15-28 days, Group IV received Karpura shilajit (200 mg/kg, bd. wt, *p.o*) for 15-28 days and group V received cystone (500 mg/kg, bd. wt, *p.o*) for 15-28 days.

2.6.1.2 Procedure

Ethylene glycol and ammonium chloride induced hyperoxaluria model was used to induce urolithiasis in rats. It was used to evaluate antilithiatic effect of *Karpura shilajit* in wistar albino rats. This is a chronic

model of urolithias where treatment period was 28 days. All the animals in different groups placed individually in metabolic cages for 24 hours with free access to drinking water, Analysed for urine volume and urine pH on 0th, 14th and 21st day. A drop of concentrated Hydrochloric acid was added to urine and stored at 40ºC. Under anaesthesia blood was withdrawn from retro orbital sinus on 0th, 7th, 14th, 21st and 28th day a sample was centrifuged at 3000 rpm for 15 min. Serum obtained was analysed for creatinine, BUN, uric acid, calcium, phosphate, oxalate, sodium and potassium (Suvarchala *et al.* 2020).

2.7 Histopathology of Kidney

For the histopathological examinations, the kidney tissue samples from the animal were fixed in 10% formalin for at least 24 h. Then the paraffin sections were prepared and cut into 5-µm thick sections in a rotary microtome. The sections were stained with Haematoxylin-eosin dye. The histopathological examination of slides were performed under plain and polarized light microscope and photographed by camera. Histopathological changes, aggregation of calcium oxalate crystals and stones in the kidney tissues were recorded (Suvarchala *et al.* 2020).

2.8 Statistical Analysis

Values are expressed as Mean ± SEM, (n=6). All the groups were compared with control, disease control and standard. By using Dunnett's test, significant values were expressed as p= 0.0001, p< 0.0001, p< 0.0005, p= 0.001.

2.9 Molecular Docking Studies

Molecular docking is a kind of bioinformatics modelling which involves the interaction of two or more molecules to give the stable adduct. Depending upon binding properties of ligand and target, it predicts the three-dimensional structure of any complex. In study mcule software is used for docking and visualized in discovery studio (Suvarchala *et al.* 2019).

2.10 Ramachandran Plot

Generated by PROCHECK validation server showing the stereo chemical quality of the protein 5AIS & 7M2O. Ramachandran plot has been generated from PROCHECK validation server was used to access the quality of the model by looking into the allowed and disallowed regions of the plot (Suvarchala et al. 2022).

2.11 Statistical Analysis

Values are expressed as Mean ± SEM, (n=6). All the groups were compared with control, diabetic control and standard by using Dunnett's test. Significant values were expressed as control group (**=p<0.01, *=p<0.05), diabetic control (A= p<0.01, B = p<0.05) and standard (a = p< 0.01, b = p< 0.05), ns- non significant.

3. RESULTS AND DISCUSSION

Karpura shilajit was explored for its antioxidant, antilithiatic and anti-inflammatory activity using suitable in vitro and in vivo models. All the results obtained in the study were included below.

3.1 Preliminary Identification Tests

Identification tests of the mineral extract revealed the presence of terpenoids, sterols, saponins, alkaloids, carbohydrates.

3.2 Acute Toxicity Study

Administration of *Karpura shilajit* at 2000 mg/kg dose showed no mortality (death rate) or no evidence of adverse effects implying that Karpura shilajit is nontoxic. No changes observed in behavioural outline, clinical signs and body mass of mice throughout 14 days of study. This shows that *Karpura shilajit* is safe to use at dose of 2000 mg/kg.

3.3 In-vitro Evaluation of Antilithiatic Activity

3.3.1 Homogenous precipitation method

Step 1: Preparation of experimental kidney stones

A)

Step 2: Preparation of semipermeable membrane from eggs

B)

C)

D)

Step 3: Estimation of calcium oxalate by titrimetry

E)

F)

G)

H)

Fig.1: In vitro antilithiatic activity by Homogenous precipitation method

A)Preparation of sodium oxalate and CaCl2., B) Eggs placed in HCl overnight, C) Contents of the egg squeezed out, D) Semi permeable egg membrane placed in ammonia solution, E) Calcium oxalate + 10 mg control/ Shilajit/ Cystone packed in membrane, placed in conical flask containing Tris buffer, F) Suturing of the membrane with contents in it, G) Conical flasks placed in incubator for 2 h at 37ºC, H) estimation of percent dissolution of calcium oxalate by titrimetric.

Table 1: Effect of *Karpura shilajit* on percent dissolution calcium oxalate by homogenous precipitation method

Group	Percent dissolution calcium oxalate (%)
Blank	0
Karpura shilajit	73.5±0.49
Cystone	64.25±0.54

The *in-vitro* antilithiatic activity of Shilajit was carried out by using homogenous precipitation method. Blank group showed no percent dissolution of calcium oxalate was found to be 0 %. Shilajit has shown increase in percent dissolution calcium oxalate to 73.5 %. The potential of the extract was comparable to that standard cystone and percent dissolution of calcium oxalate value was found to be 64.25 %.

3.3.2 In vitro evaluation of anti-inflammatory activity

3.3.2.1 Protein denaturation assay

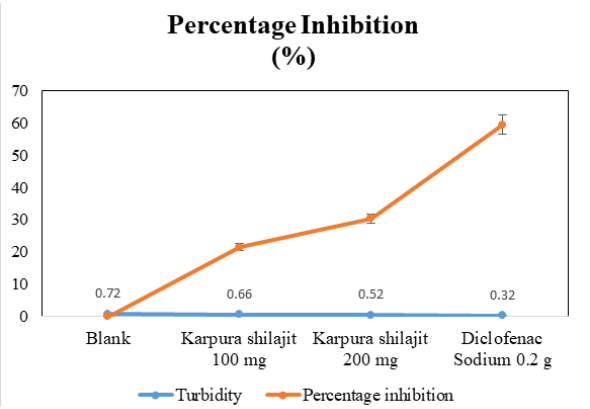

Fig.2: Effect of Karpura shilajit and Diclofenac sodium on turbidity and percentage inhibition in invitro Protein Denaturation assay method.

The *in-vitro* antilithiatic activity Karpura shilajit was carried out by using Protein Denaturation assay. Blank group showed high turbidity so the percent inhibition was found to be 0 %. Shilajit has shown increase in percent inhibition, decrease in turbidity with increase in dose, Shilajit 100 - 21.51 % and Shilajit 200 – 30.37 % . The potential of the extract was comparable to that standard Diclofenac sodium and percent inhibition value was found to be 59.49.

3.4 *In vivo* evaluation of antilithiatic activity

3.4.1 Ethylene glycol – ammonium chloride induced urolithiasis

In lithiatic disease control group the creatinine, uric acid, BUN, calcium and potassium levels were increased and sodium level was decreased after the administration of ethylene glycol-ammonium chloride and it was known to be significant in comparison with normal control. In treatment groups the *Karpura shilajit* 100 mg/kg and 200 mg/kg produced significant increase in sodium levels and significant decrease in creatinine, uric acid, phosphate, BUN, calcium and potassium levels respectively and showed results compared with disease control group. The dose of 200 mg/kg had shown better response than the 100 mg/kg dose which was comparable to standard Cystone shown in Table 2, Figure 3

Table 2: Effect of *Karpura shilajit* on serum creatinine, Uric acid, BUN, Sodium, potassium and calcium levels in ethylene glycol- ammonium chloride model.

	Control	Disease control	Karpura shilajit 100 mg/kg	Karpura shilajit 200 mg/kg	Cystone 500 mg/kg
Creatinine (mg/dL)	0.67±0.03	6.17±0.23^{a}	2.90±0.09^{a*B}	1.80±0.08^{a*ns}	1.62±0.10^{a*}
Uric acid (mg/dL)	0.94±0.19	4.80±0.27*	2.53±0.14^{a*D}	1.69±0.14^{a*ns}	1.49±0.14^{*a}
Potassium (mEq/L)	3.73±0.11	20.1±0.94*	6.48±0.25^{a*ns}	6.14±0.33^{a*ns}	5.78±0.28^{*a}
BUN (mg/dL)	33.5±0.69	106.83±0.84*	54.33±0.60^{a*A}	47.5±0.91^{a*C}	43.12±0.72^{*a}
Sodium (mEq/L)	140.8±0.80	76.5±0.81*	126.6±0.54^{a*A}	138.16±0.86^{*aA}	140.16±0.70^{*a}
Calcium (mg/dL)	10.15±0.2	15.31±0.21*	12.43±0.27^{a*C}	11.59±0.32^{a**ns}	10.76±0.42^{**a}

The values were expressed as mean ± SEM (n=6), analysis was performed with one way ANOVA followed by Dunnett's multiple comparison test against control (*= p=0.0001, **= p<0.001, ***= p<0.0001), against disease (a= p=0.0001, b= p<0.0001) and against Cystone 500 (A= p=0.0001, B= p<0.0001, C= p<0.001, D= p=0.001). ns = non-significant

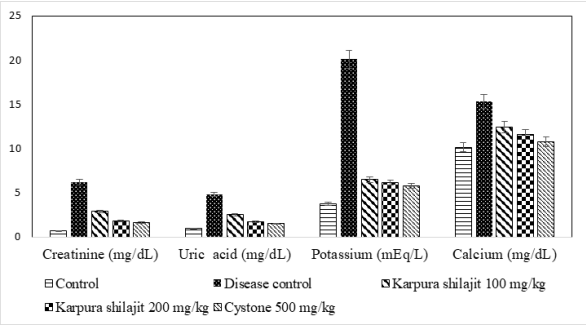

Fig.3: Effect of Karpura shilajit on serum creatinine, Uric acid, potassium and calcium levels in ethylene glycol- ammonium chloride model.

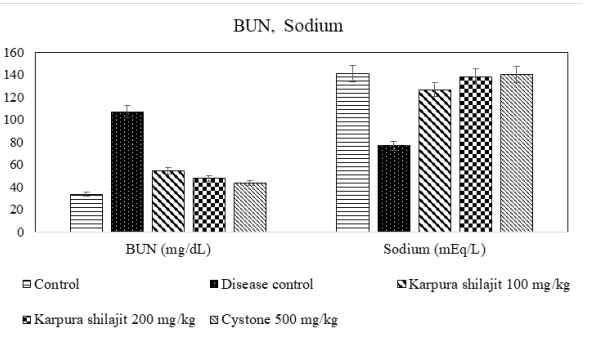

Fig.4: Effect of Karpura shilajit on serum BUN and Sodium levels in ethylene glycol- ammonium chloride model

3.5 Molecular Docking Studies

To perform docking, initially the protein was downloaded from PDB and molecular docking performed in mCule software and visualized in discovery studio. Some compounds exhibited good binding ability with prostaglandin synthase inhibitor (PDB ID: 5AIS) for anti-inflammation activity and glycolate oxidase/lactate dehydrogenase inhibitor (PDB ID: 7M2O) antilithiatic activity were given [Fig. 5 &6] and docking results with glide score (Table 3).

Table 3: Glide scores of *Karpura shilajit* constituents with 5AIS and 7M2O protein

Constituents	Glide scores (KcaL/moL)	
	5AIS	7M2O
Berginin	-5.9	-7.0
Bendazol	-7.2	-8.1
2,5 Anhydrotalitol	-4.2	-5.1
Xylofuranose	-4.1	-4.7
Thymol	6.3	-6.4
Cystine	-4.0	-5.5
6-Nitroimidazo [1,2-a] Pyridine	-5.8	-5.8
Cycloheptatriene	-5.2	-4.8
2-(4-Nitrophenyl) Succinic acid	-6.6	-6.6
Tartronic acid	-4.1	-4.4
Ferulic acid	-6.5	-6.6
2,4,4-Trimethoxy chalcone	-7.5	-7.7
D-Ribitol-5-Phosphate	-5.0	-5.5
Quinoline -2-Carboxylic acid	-7.4	-6.9
Cyclopropane Carboxamide	-4.0	-4.3

ANTI–INFLAMMATORY Protein PDB ID (5AIS)

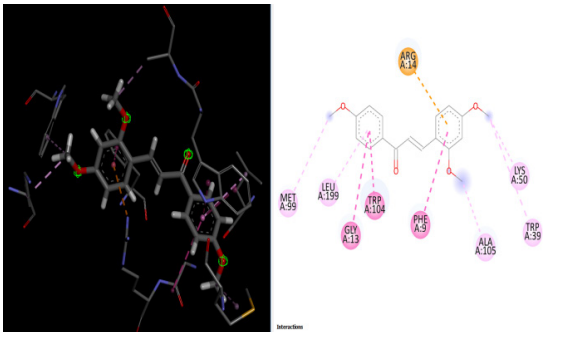

a) 2,4,4`-trimethoxy chalcone = -7.5

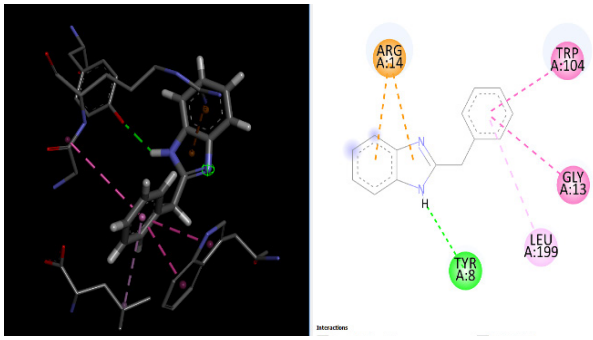

b) Bendazol = -7.2

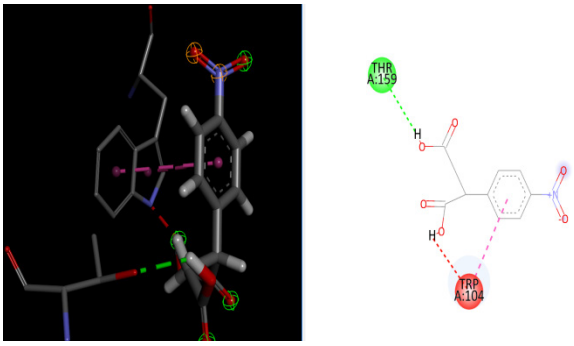

c) Ferulic acid = -6.5

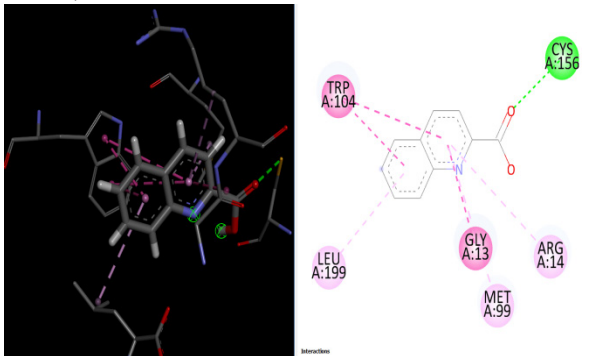

d) Quinoline-2-carboxylic acid = -7.4

Fig.5: 3D & 2D structures of Prostaglandin synthase inhibitor (PDB ID: 5AIS) for anti-inflammation activity

Anti urolithiatic activity Protein PDB ID (7M2O)

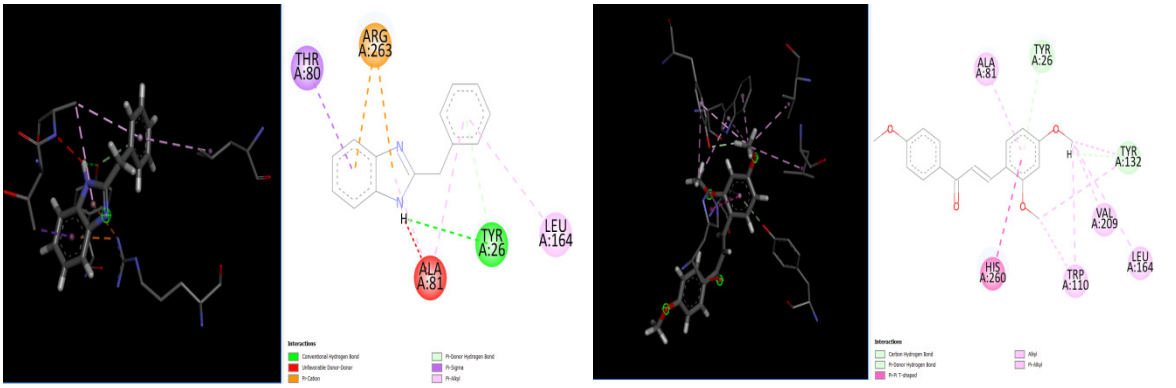

a) Bendazole: -8.1 b) 2,4,4'-Trimethoxychalcone: -7.7

c) Berginin: -7.0 d) Qunoline-2-carboxylic acid: -6.9

Fig.6: 3D & 2D structures of Glycolate oxidase / Lactate dehydrogenase inhibitor (PDB ID: 7M2O) antilithiatic activity

The more negative the Glidescore the more favourable is the binding. G score = glidescore,

3.6 Ramachandran plot Analysis

Protein 5AIS and 7M2O were analysed for Ramachandran plot to know amino acid presence in different regions of respective protein tabulated in table 4 and pictorial representation by fig. 7.

Table 4: Ramachandran plot status with protein 5AIS and 7M2O

Residues	5AIS	7M2O
Most favourable region (%)	94.9	93.2
Additional allowed regions (%)	4.6	5.4
Generously allowed regions (%)	0.6	1.4
Disallowed regions (%)	0.0	0.0

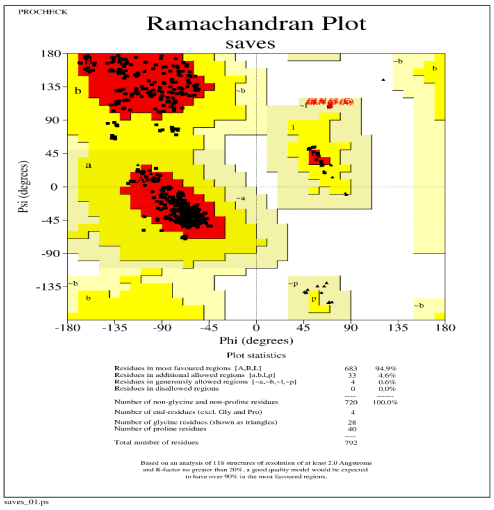

a) 5AIS

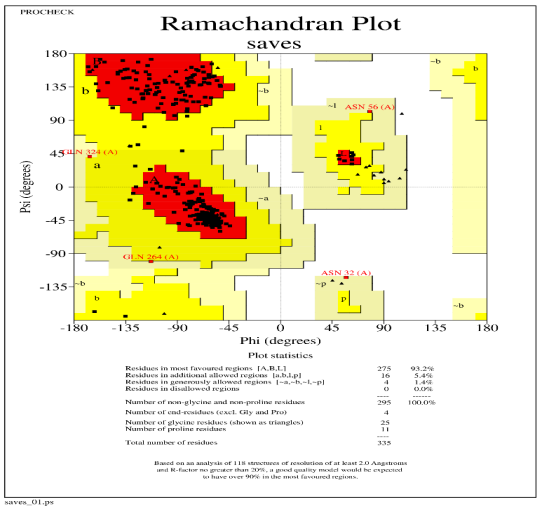

b) 7M2O

Fig.7: Ramachandran plot of protein 5AIS and 7M2O

4. DISCUSSION

The present work aimed with the objective of phytochemical investigation with anti-lithiatic and anti-inflammatory activity of mineral extract of *Karpura shilajit* in wistar albino rats. Preliminary phytochemical investigation of shilajit showed the presence of alkaloids, steroids, carbohydrates, saponins and terpenoids. In acute toxicity study of shilajit the maximum accepted dose was found to be 2000 mg/kg, bd.wt. (*p.o*). *In vitro* antilithiatic activity by homogenous precipitation method, shilajit and cystone dissolved calcium oxalate precipitate that is prepared. The percent dissolution of calcium oxalate is high in cystone and shilajit compared to blank.

Model used for *in vivo* lithiasis induction is ethylene glycol – ammonium chloride model which cause induction of calcium oxalate urolithiasis. Hyperoxaluria is a more significant risk factor in the pathogenesis of renal stone (Takawal *et al.* 2012). When EG is used alone, kidney crystal deposition can be quite inconsistent. To achieve uniformly high rate of kidney crystal deposition, ammonium chloride has been used in combination with ethylene glycol (Bano *et al.* 2018). EG is readily absorbed in intestine and is metabolized in the liver to oxalate leading to hyperoxaluria. Furthermore, accumulation of the calcium oxalate crystals in the kidney decreased the urinary pH, which is one of the indications of urolithiasis (Ilhan *et al.* 2014). In disease group, there is decrease in urine pH, urine volume, increased kidney weight which is due to renal impairment, *Karpura shilajit* and cystone group the results are reversed. The percent change in body weight is significantly low in disease group where as there is increasing order shilajit 100, shilajit 200, cystone and control group. Disease control group showed enhanced levels of urea, creatinine, uric acid, calcium, phosphate, electrolyte potassium and decreased sodium levels. Cystone and shilajit was found to show good nephroprotective activity by decreasing the elevated levels of urea, creatinine, uric acid, calcium, phosphate, electrolyte potassium and increased sodium electrolyte level in serum. *Karpura shilajit* 200 showed better effects than *Karpura shilajit* 100.

Steroids have been used to treat or prevent the induced mucosal inflammatory reactions that cause edema formation due to stone presence, which will eventually facilitate stone expulsion. Corticosteroids stabilize lysosomes of neutrophils by exerting anti-inflammatory and anti-edema actions; they also may exhibit their inflammation reduction by inhibiting prostaglandin release at the site of obstruction (Nouri *et al.* 2017). The potential urolithiasis preventive effect might have been contributed by the rich terpenoid content, which prevented the formation of the calcium oxalate crystals by either of the mechanisms; increased bioavailability of nitric oxide that suppressed the influx of calcium by

cGMP pathways and its nephroprotective action.

Primary hyperoxaluria (PH) produce glyoxylate reductase (GR), impairing hepatic detoxification of glyoxylate and corresponding excessive oxalate production in the liver via the action of lactate dehydrogenase A (LDHA). Oxalate produced in the liver is excreted via the kidneys, but when present at high concentrations, it complexes with calcium to form calcium oxalate salt. Deposits of calcium oxalate within the kidney can lead to inflammation. As kidney function deteriorates, concentrations of plasma oxalate increase, and calcium oxalate can accumulate. Two inhibition mechanisms have been the focus of therapeutic development for PH: glycolate oxidase and LDHA (Ding *et al.* 2021). Prostaglandin D2 (PGD2) is an allergic and inflammatory mediator produced by mast cells and Th2 cells, PG inhibitors have an anti-inflammatory effects. The compounds present in *Karpura shilajit*, are docked with prostaglandin synthase inhibitor protein (PDB ID: 5AIS) for anti-inflammation activity and Lactate dehydrogenase inhibitor protein (PDB ID: 7M2O) antilithiatic activity and Ramachandran plot is analysed.

Bendazole, 2,4,4-Trimethoxychalcone and Quinoline-2-Carboxylic acid showed good docking score when compared to other compounds for protein 7M2O & 5AIS and Ramachandran plot showed > 93% of amino acids in mostly allowed regions. In the present study the superposition of 2,4,4'-Trimethoxychalcone, Bendazole and other compounds docking found with prostaglandin synthase inhibitor protein (PDB ID: 5AIS) and lactate dehydrogenase inhibitor protein (PDB ID: 7M2O) protein have validated the accuracy of our docking study, Ramachandran plot that resulted anti-inflammatory and antilithiatic activity.

5. CONCLUSION

In the present study, *Karpura shilajit* was screened for in vitro antilithiatic activity by homogenous precipitation method which has shown increase in percent dissolution calcium oxalate. The presence of terpenoids, and sterols, flavonoids might be responsible for anti-inflammatory activity. *Karpura shilajit* was screened for in vivo antilithiatic activity by ethylene glycol ammonium chloride induced lithiasis. During histopathological examinations shilajit has shown decrease in calcium oxalate crystal deposition, with increase in dose. The results were comparable with standard and control groups. Histopathology results have revealed *Karpura shilajit's* potential in reducing the stone formation and regeneration of damaged glomeruli. Molecular docking studies confirmed the lactate dehydrogenase inhibitory effect and PG's inhibitory effect of the compounds, as they occupied the binding site and was found to possess hydrogen bonding interactions. The Glide scores order for all molecules reflected the experimental lactate dehydrogenase inhibitory effect and PG's inhibitory activity.

ACKNOWLEDGEMENTS

The authors are grateful to the Principal Prof. M. Ganga Raju and Management of the Gokaraju Rangaraju College of pharmacy, for the constant support and encouragement during the course of the work.

REFERENCES

Alelign, T., Petros, B., Kidney Stone Disease: An Update on Current Concepts. Hindawi advances in Urology 1-12:2018.
DOI: 10.1155/2018/3068365
PMID: 29515627 PMCID: PMC5817324

Bano, H., Jahan, N., Makbul, S.A.A., 2018. Effect of Piper *cubeba* L. fruit on ethylene glycol and ammonium chloride induced urolithiasis in male Sprague Dawley rats. Integrative medicine research 1-8.
DOI: 10.1016/j.imr.2018.06.005
PMID: 30591890 PMCID: PMC6303358

Ding, J., Gumpena, R., Boily, M. O., Caron, A., Chong, O., Cox, J. H., Powell, D. A. 2021. Dual Glycolate Oxidase/Lactate Dehydrogenase A Inhibitors for Primary Hyperoxaluria. ACS Medicinal Chemistry Letters 12(7):1116-1123.
DOI: 10.1021/acsmedchemlett.1c00196
PMID: 34267881 PMCID: PMC8274068

Ganga Raju, M., Kumara Swamy, K., 2018. Anti-inflammatory and antiradical potential of methanolic extract of *Cajanus cajan*. Asian Journal of Pharmacy and Pharmacology 4(6): 860-864.
DOI: 10.31024/ajpp.2018.4.6.21

Grases, F., Bauza, C.A., Prieto, R.M., 2006. Renal lithiasis and nutrition. Nutritional journal 5(23):1-7.
DOI: 10.1186/1475-2891-5-23
PMID: 16956397 PMCID: PMC1586208

Ilhan, M., Ergene, B, Suntar, I., Ozbilgin, S., Citollu, G.S., Demirel, M.A., Kele, G.H., Altun, L., Akkol, E.K., 2014. Preclinical Evaluation of Antiurolithiatic Activity of *Viburnum opulus L*. on Sodium Oxalate-Induced Urolithiasis Rat Model. Evidence-Based Complementary and Alternative Medicine 1-10. DOI: 10.1155/2014/578103
PMID: 25165481 PMCID: PMC4137613

Kany, S., Vollrath, J.T., Relja, B. 2019. Cytokines in Inflammatory Disease, International Journal of Molecular Sciences 20(23): 60-80. DOI: 10.3390/ijms20236008
PMID: 31795299 PMCID: PMC6929211

Nareshrao, P.D., and Talekar, M. 2019. Shilajitu Asphaltum traditional Medicine. World Journal of Pharmacy and Pharmaceutical Sciences 4(11):1985-94.

Nouri, A., Hassali , M.A., Hamza, A.A., 2017. The role of corticosteroids in the management of kidney stones disease: a systematic review, Research Article - Clinical Practice 14(6): 368-375. DOI: 10.4172/clinical-practice.1000133

Suvarchala Reddy, N. V. L. V., Ganga Raju, M., Anusha, V., Gaikwad, A., Pulate, C., Mahajan, K., Tare, H., 2022.Investigation of potential antiurolithiatic activity and *in silico* docking studies of *Karpura shilajit*. International Journal of Health Sciences 6(S4): 8900-8916. DOI: 10.53730/ijhs.v6nS4.11875

Suvarchala Reddy, V. N.V.L., Ganga Raju, M., Mamatha, M., 2021. Antilithiatic activity of leaf extract of Citrus *medica* on sodium oxalate urolithiais - *in vitro* and *in vivo* evaluation. International Journal of Pharmaceutical Sciences and Research 12(7): 3709-3715.

Suvarchala Reddy, V.N.V.L., Anarthe, S.J., Raju, M.G., Akhila, M., Raj, G.B.P., 2019. Molecular docking studies of isolated compounds from *Cassia fistula* on HMG-COA reductase. Asian Journal of Research in Chemistry 12(2): 89-93. DOI: 10.5958/0974-4150.2019.00020.8

Suvarchala Reddy, V.N.V.L., Ganga Raju, M., Goud, R.M., Shabnamkumari, T., 2020. Neuroprotective Activity of Methanolic extract of *Terminala bellerica* Fruit against Aluminium Chloride and Haloperidol Induced Amnesia in Mice. Journal of Young Pharmacists 12(2)Suppl: s87-s90. DOI: 10.5530/jyp.2020.12s.53

Suvarchala Reddy, V.N.V.L., Mamatha, M., Ganga Raju, M., 2020. Effect of *Citrus medica* leaf extract on Ethylene Glycol - Ammonium Chloride induced urolithiasis in Wistar Albino rats. Journal of Advanced Scientific Research 11: 29-37.

Suvarchala Reddy, V.N.V.L., Raju, M.G., Mamatha, M., Thakur, S.K., 2022. Antihyperlipidemic Studies of Methanolic Extract of *Gossypium herbaceum*: An In silico and In vivo Approach. Asian Journal of Research in Medical and Pharmaceutical Sciences 11(3): 32-42. DOI: 10.9734/ajrimps/2022/v11i330193

Takawal, R.V., Mali, V.R., Kapase, C.U., Bodhankar, S.L., 2012. Effect of *Lagenaria siceraria* fruit powder on sodium oxalate induced urolithiasis in Wistar rats. Journal of Ayurveda & Integrative Medicine 3(2): 75-79. DOI: 10.4103/0975-9476.96522
PMID: 22707863 PMCID: PMC3371562

Flowering of *Prunus cerasoides* D.Don in its Native Land (The Himalayas) and Some Other Countries in Asia

Umed Kumar Pun[1*], Sudhir Shrestha[2] and Nirajan Bhandari[3]

[1] *King Mongkut's Institute of Technology Ladkrabang, Bangkok, Thailand*
[2] *Floriculture Development Centre, Lalitpur, Nepal*
[3] *College of Natural Resource Management, Agriculture and Forestry University, Pakhribas, Dhankuta, Nepal*

***CORRESPONDING AUTHOR:**

Umed Kumar Pun
Email: umedpun@gmail.com

ISSN : 2382-5359(Online), 1994-1412(Print)

DOI:
https://doi.org/10.3126/njst.v22i2.85241

Date of Submission: 15 Mar, 2024

Date of Acceptance: 11 Jul, 2024

ABSTRACT

Prunus cerasoides D. Don is the botanical name of the Himalayan cherry and is distributed in the Himalayas and other regions of Asia. Time to defoliation, time to flowering, and flower colour were reviewed in the research database such as Google scholar, ResearchGate and Google. Survey was also carried out in Kathmandu valley, Pokhara, Chitwan of Nepal and Chiang Rai of Thailand to understand the stated parameters. Three colours of flowers were observed in the Himalayan cherry: light pink, white and pink. In the similar locations, light pink type cherry tree flower earlier followed by white whereas flowering was late in pink type flowers. Altitude of the location influenced the time to flower induction and the trend was observed in all the types. This probably could be triggered by lower minimum temperature and was found important to influence flowering time in contrast to the geographical location in the Himalayan region. In South Asian countries, Himalayan cherry flowers from mid part of October to January. However, flowering of Himalayan cherry was found to be in November-December (Japan), December-January (Vietnam), December-February (Thailand) whereas flowering was twice (March-April and August-September) in Indonesia.

Keywords: Defoliation, Flowering, Himalayan Cherry, *Prunus cerasoides*

1. INTRODUCTION

Prunus cerasoides is the name of the species for the Himalayan cherry and its Nepali name is Painyu. It has similar vernacular names in different places such as Bhenkal (Uttarakhand, India), Pajja (Himachal Pradesh, India), Dieng Kaditusoo (Meghalaya, India), Tlaizawng (Mizoram, India) and, Nang Phaya Sua Krong (Thailand). Himalayan cherry is found in the mid hills of Nepal and has been reported from several districts especially from Lumbini Province, Gandaki Province, Bagmati Province, and Koshi Province of Nepal (*Pun et al* 2023). Unlike its

popular cousin, the Sakura (*Prunus serrulata*), it is not so familiar globally but, in the Himalayan region, where it originates, it is becoming popular recently. In the Himalayan region, cherry primarily flowers in autumn-winter that ranged anywhere from October to December depending on the altitude of the locations. The flowering period of the Himalayan cherry may range from two to three weeks after first flowering. The parks, towns and forest are laden with cherry blooms during the flowering season. There is even weeklong Himalayan cherry festival celebrated in the mid November at Shillong, Meghalaya since 2016 (Govil 2018).

Despite of the recent popularity, this tree species is still not much researched for its ornamental value. This tree species has been found important for bee keeping in the hills, as fodder for the cattle (Tiwari *et al* 2009) and as important framework tree species for restoring evergreen forest in northern Thailand (Pakkad *et al* 2003). The plant is reported to exist in the northern and north-eastern hill states of India, hills of Nepal, Pakistan, Bhutan, Myanmar, China, Thailand (Kerby *et al* 2000) and Indonesia (Kurniwan *et al* 2021). This research attempted to review and record the existence of this species in the region. In addition, it also recorded the location of the city or town where this tree has been reported flowering with Global Positioning System (GPS), record defoliation and flowering time, and colours of flowers.

2. MATERIALS AND METHODS

Relevant information regarding *Prunus cerasoides* was generated from electronic database such as Academic Journals, Google scholar, ResearchGate, Google, and eFloraofIndia (https://efloraofindia.com). Information of interest were time of defoliation, flowering time, and colour of flowers from the Himalayan region and other regions in Asia where it is reported. Flower colours were assessed visually both from the internet or physically. Data in Nepal was generated by visiting the site of tree during the time of defoliation and flowering whereas information from other countries were accessed through literature. Survey was done in Kaski, Chitwan, Lalitpur, Bhaktapur, Kathmandu of Nepal, and Chiang Rai of Thailand. Detail of geographical location such as GPS was derived from the internet database. Climatic data of the location of interest was derived Climate Data (https://en.climate-data.org) and compared with the time of flowering to understand critical factor influencing flower induction.

3. RESULTS

3.1 Defoliation, Flowering, and Flower Colour of Himalayan Cherry in Nepal

The defoliation and flowering of Himalayan cherry in Nepal occurs in autumn-winter (Table 1). However, time of defoliation of leaves was influenced by type of flower colour and altitude. Defoliation occurred earlier on trees bearing light pink, followed by white and pink flowers. This characteristic showed similar trend irrespective of the locations. Similarly, defoliation occurred earlier in higher altitude in contrast to lower altitude, but the trend of light pink flower flowering earlier than others was observed. Light pink was the earliest to defoliate at 1875 meters above sea level (masl), (first week of October), followed by 1560masl (second week of October). White defoliated at 1875masl (second week of October), followed by 1560masl (last week of October), and at 415masl (last week of December). However pink defoliated at 1875masl (third week of October) and 1560masl (last week of October). The difference in defoliation time of light pink Himalayan cherry tree was one week between 1875masl and 1560masl. However, in white Himalayan cherry tree, the difference in defoliation time was two weeks between 1875masl and 1560masl but the difference was more when the altitude was much lower (250masl) (ten weeks as compared with 1875masl and eight weeks as compared with 1560masl). In pink Himalayan cherry, the difference in defoliation time was one week between 1875masl and 1560masl. Time taken from defoliation to flowering ranged from one to three weeks and consistently it was one week with light pink type but one to three weeks in white and two weeks in pink type across the altitude types.

Types and altitude seem to influence the time to flowering in Himalayan cherry (Table 1). Light pink seems to flower earlier than white and pink types. Himalayan cherry in higher altitudes flowered much earlier than the lower altitudes. In case of light pink Himalayan cherry, flowering began in second week of October in Shivpuri, Kathmandu (1875masl), third week of October in Godavari (1560masl), second week of November in Bhaktapur (1401masl) and Ilam (1206masl) and first week of December in Pokhara

(822masl). Similarly, in case of white Himalayan cherry, flowering began in the third week of October in Shivapuri, Kathmandu (1875masl) and second week of November in Godavari, Lalitpur (1560masl) and third week of January in Chitwan (250masl). The trend was alike in the case of the pink Himalayan cherry too. Flowering was much earlier (first week of November) in Shivapuri, Kathmandu (1875masl) as compared to Bhaktapur (1401masl; third week of December). There was no influence of the latitudes and longitudes of the observed locations within the geographical range of (26.9099°N to 28.2096°N) and (83.9856°E to 87.9283°E).

Table 1: Time of defoliation, flowering, and flower colour of Himalayan cherry in Kathmandu valley of Nepal

Location	Altitude (m)	GPS coordinates	Defoliation time	Flowering time	Colour of flower
Shivapuri-Nagarjun National Park, Kathmandu	1875	27.6016°N 85.3653°E	First week of October	Second week of October	Light pink
Shivapuri-Nagarjun National Park, Kathmandu	1875	27.6016°N 85.3653°E	Second week of October	Third week of October	White
Shivapuri-Nagarjun National Park, Kathmandu	1875	27.6016°N 85.3653°E	Third week of October	First week of November	Pink
Floriculture Development Center, Godavari, Lalitpur*	1560	27.6016°N 85.3653°E	Second week of October	Third week of October	Light pink
Floriculture Development Center, Godavari, Lalitpur*	1560	27.6016°N 85.3653°E	Last week of October	Second week of November	White
National Botanical Garden, Godavari, Lalitpur*	1560	27.6016°N 85.3653°E	Last week of October	Second week of November	Pink
Pokhara, Kaski*	822	28.2096°N 83.9856°E	Last week of November	First week of December	Light pink
Sericulture Development Center, Bhandara, Chitwan	250	27.771°N 84.602°E	Last week of December	Third week of January	White

Source: Field survey October 2022 to January 2023

*Surveyed two years (October 2021 to January 2022 and October 2022 to January 2023)

3.2 Types of Himalayan Cherry

Himalayan cherry based on the colour of the flowers are of three types such as light pink, white and pink (Table 1 and Photos 1-3).

Photo 1: Light Pink Himalayan cherry (Godavari, 1560masl, PC: Sudhir Shrestha)

Photo 2: White Himalayan cherry (Godavari, 1560masl, PC: Sudhir Shrestha)

Photo 3: Pink Himalayan cherry (Shivapuri, 1875masl, PC: Sudhir Shrestha)

3.3 Flowering of Himalayan cherry in India

In India, Himalayan cherry begins flowering in high hills of Uttarakhand beginning in the third week of October followed by high hills of Himachal Pradesh in November and the northeast of India (Kohima or Shillong) (Table 2). In Himachal Pradesh, altitude range from 1200masl (Dalhousie) to 2276masl (Shimla) is reported to flower in November, not specified in some cases but in Dharamsala (1750masl), it flowers in second week of November. Similarly, in Uttarakhand, altitude range from 430masl (Dehradun) to 2680masl (Chapota) is reported to flower in Mid-December and third week of October respectively in light pink types. However, the pink colour Himalayan cherry is reported to flower in the first week of November at Chapota (2680masl). Flowering of Himalayan cherry in the northeast is reported in the second week (Shillong) and third week (Kohima) of November. There is no clear influence of the latitudes and longitudes of the various locations; (32.5395°N to 25.5788°N) and (75.9709°E to 94.1086°E). The flowering trend of the Himalayan cherry in India is similar to Nepal and is influenced by types (light pink flowers earlier than other) and altitudes (earlier flowering in higher altitudes than lower).

Table 2: Flowering of Himalayan cherry and flower colour in different Himalayan regions of India

S/N	Name of location	Altitude (m)	GPS coordinates	Flowering time	Flower colour	Source
1	Dalhousie, Himachal Pradesh	1200	32.5395°N 75.9709°E	November	Pink	
2	Dharmsala, Himachal Pradesh	1750	32.2190°N 76.3234°E	Fourth week of October	Light Pink	
3	Shimla, Himachal Pradesh	2276	31.1048°N 77.1734°E	November	Light Pink	
4	Dehradun, Uttarakhand, India	430	30.3165°N 78.0322°E	Mid-December	Light Pink	
5	Chapota, Uttarakhand, India	2680	30.3462°N 79.0485°E	Third week of October First week of November	Light Pink Pink	
6	Ramgarh, Uttarakhand	1518	29.4464°N 79.5596°E	Third week of October	Light Pink	
7	Kohima, Nagaland, India	1444	25.6751°N 94.1086°E	Third week of November	Light Pink	
8	Shillong, Meghalaya, India	1491	25.5788°N 91.8933°E	Second week of November	Light Pink	

Source: eFloraofIndia

3.4 Flowering of Himalayan Cherry in some Asian Countries

In some of the Asian countries, flowering time of the Himalayan cherry seem to be unaffected by altitude (Table 3). In Kurashiki (3masl), white Himalayan cherry flowered in November-December much earlier than the light pink (December-January) or pink (December-January) flowering in Chiang Mai, Thailand (310masl) or light pink (December-January) in Da Lat, Vietnam (1500masl) or Pink (January-February) in Chiang Rai, Thailand (1500masl). In Mae Fah Luang arboretum, Doi Tung (>1500masl), Chiang Rai, several Himalayan cherry trees (pink) was post peak flowering in the first week of February. Interestingly, about 1200masl on the way to Chiang Rai city from Doi Tung, the pink type of Himalayan cherry was in full bloom, suggesting the influence of altitude on flower induction. Himalayan cherry, light pink type is reported to flower twice in Cianjur, Indonesia (392masl): March-April and August-October. Flowering time of Himalayan cherry in Cianjur is different to other regions because it is in the Southern Hemisphere, and it is cold in August-October but flowering in March-April is unexplainable from temperature perspective, but other factors could be playing some role.

Table 3: Flowering of Himalayan cherry and flower colour in different regions of Asia.

S/N	Name of location	Altitude (m)	GPS coordinates	Flowering time	Flower colour	Source
1	Kurashiki, Japan	3	34.5850°N 133.7720°E	November-December	White	
2	Chiang Rai, Thailand*	1500	20.3352°N 99.8109°E	January-February	Pink*	
3	Chiang Mai, Thailand	310	18.7883°N 98.9853°E	December January	Light Pink Pink	
4	Da Lat, Vietnam	1500	11.9404°N 108.4583°E	December-January	Light Pink	
5	Cianjur, West Java, Indonesia	392	6.8168°S 107.1425°E	March-April August-October	Light Pink Light Pink	

Source: Field survey February 2023*, https://shutterstock.com (ID1605121330), https://tuoitrenews.vn/news/vietnam-life/photo (ID20231229)

3.5 Minimum Temperatures of Town and Cities in the Himalayas and other Asian Cities at the time of Defoliation and Flowering

The minimum temperature in the Himalayas when defoliation and flowering occur averaged 15°C and 12°C respectively (Figure 1). The minimum temperature was much cooler in Dalhousie and defoliation occurred at about 10°C and flowering at about 5°C as compared to other towns/cities. In other cities in Asia, the flowering occurred at varied temperatures, Kurushiki (5°C), Chiang Mai (15°C), Da Lat, and Chiang Rai (<15°C) and 18-19°C in Cianjur (Figure 2). In Cianjur, the minimum temperature is 18-20°C all through the year.

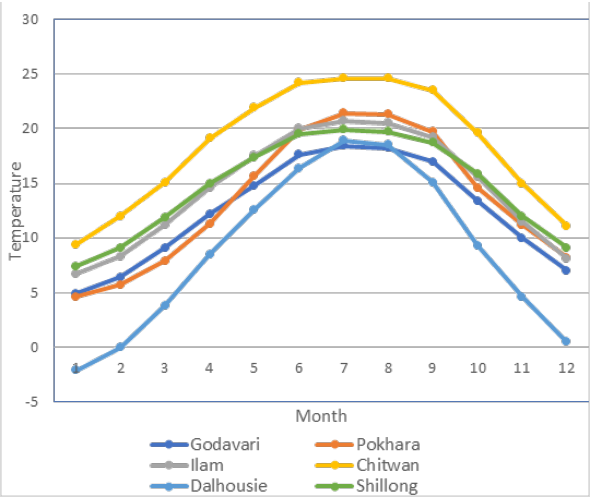

Fig.1: Minimum temperature of town/cities in the Himalayas (Source: Climate Data)

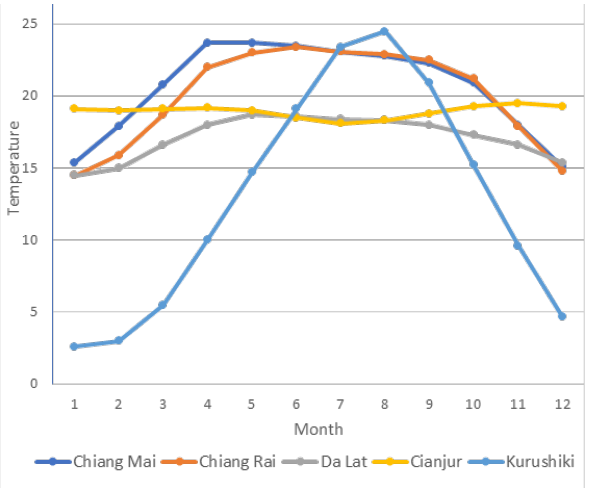

Fig.2: Minimum temperature of the cities in other regions of Asia (Source: Climate Data)

4. DISCUSSION

4.1 Types of Himalayan Cherry

Three types of Himalayan cherry were categorised based on the flower colours. They are light pink, white, and pink. All these three colours are reported from India (Joseph *et al* 2018), but this is the first reporting from Nepal.

4.2 Defoliation of Himalayan Cherry

In the Himalayan region, defoliation is influenced by the types of Himalayan cherry and altitudes. Light pink flowers earlier than others (white or pink) and therefore may need less low minimum temperature for defoliation. Higher altitude induces early defoliation of leaves and therefore it may be associated with the lowering of minimum temperature of 15°C or less. However, in the other Asian regions such as Thailand and Vietnam, the trigger is minimum temperature of about 15°C in Chiang Mai and Da Lat (the lowest temperature of the year in these locations) whereas the minimum temperature is about 5°C in Kurashiki, Japan. The defoliation in Indonesia is not very clear because it happens twice a year and the minimum temperature (18-19°C) conditions are similar all year round (Kurniwan *et al* 2021). The geographical position (latitudes and longitudes) is perhaps not influencing the leaf defoliation in contrast to the Japanese cherry (Sakura).

4.3 Flowering of Himalayan Cherry

Himalayan cherry began flowering in the Himalayas from October until January. Flowering is influenced by the type and altitude. Light pink flowers earlier than white and pink in the similar altitude and all types of Himalayan cherry flowers earlier in the higher altitude than lower altitudes in similar sequence. All colours of Himalayan cherry defoliate, and flowers based on the altitude but seems to be not influenced by the global positions. The flowering occurs when the minimum temperature is less than 12°C in the Himalayas but in the other regions, flowering occurs when the temperature is below 10°C (Kurashiki, Japan) or around 15°C in Chiang Mai, Thailand and Da Lat, Vietnam. The falling night temperature and shorter day length is perhaps associated with defoliation, flower bud initiation, flowering, and emergence of leaves. The twice flowering season in Cianjur, Indonesia is yet to be understood and needs further study (Kurniwan *et al* 2021). Could it be the southern hemisphere effect because *P. cerasoides* is also reported to flower twice in Bali of Indonesia in similar months (Oktavia *et al* 2023) unlike the single season flowering in the Himalayas and the northern hemisphere. Lack of fruition in the Himalayan cherry of Indonesia (Oktavia *et al* 2023) may be the factor that results in two flowering seasons. Himalayan Cherry of white flower colour has been reported to flower earlier at higher elevation than the lower elevation in the Sikkim Himalayan region (Lachungpa, 2012) and our data agrees to this fact. The earliest flowering begins from 7000-8000' (first week of November) (2334-2667masl), 5000' (second week of November) (1667masl) and 3000-4000' (third week of November) (1000-1333masl).

Similar, trend has been observed in light pink, white and pink Himalayan cherry in different altitudes of Nepal and India. This confirms the analogy that lowering of temperature could be the trigger factor in inducing leaf fall and accelerate flower bud emergence. Global position (latitudes and longitudes) doesn't seem to influence flowering in the Himalayan cherry unlike the Japanese cherry (Sakura) which is highly influenced and begins flowering in spring season from south and heads towards the north Japan with some exceptions. This variation in the initiation of flowering is due to early onset of spring in the south Japan as compared with the north Japan. In 2021, the earliest flowering was forecasted in Fukuoka (19th March) in southern Japan and the last was in Kushiro (10th May) in northern Japan (Anonymous 2021). The contrasting characteristics being the need of warmer temperature for flower induction of the Japanese cherry (Sakura) (few exceptions) whereas Himalayan cherry need cooler temperature for flower induction.

This clearly shows that Himalayan cherry can be planted across Nepal and enjoyed by people across the nation at different time of the year. Cluster plantation at different altitudes in villages, towns or cities or barren land in the forest could give a mass effect during the flowering season drastically improving the landscape and attracting visitors.

5. CONCLUSION

Himalayan cherry has been found distributed from South Asia to other regions of Asia. Defoliation and flowering were influenced by the types of Himalayan cherry and altitudes. The critical factor influencing these parameters could be the minimum low temperature with the onset of autumn at least in the Himalayan region. Thus, Himalayan cherry flowers between October to January in the Himalayas. This contrasts with the Japanese cherry (Sakura) that flowers with the increase in minimum temperature in Spring (March onwards). Unlike, the prevailing belief that the Himalayan cherry can be only grown in the mid hills (natural habitat), this paper shows that this beautiful tree can be grown from the highest reported altitude (2680masl, Chapota, India) to the lowest altitude (3masl, Kurashiki, Japan).

REFERENCES

Anonymous, 2021. Cherry Blossom Forecast in 2021 When to see cherry Blossom in Japan. https://en.japantravel.com/feature/cherry-blossom-in-japan

Govil, B. 2018. Lay out a picnic blanket and enjoy the Japanese art of hanami (seeing flowers) right here in our pink-coloured backyard. https://www.outlookindia.com/outlooktraveller/explore/story/69162/cherry-blossoms-bloom-early-in-shillongand-theres-a-festival-to-celebrate-it-too

Joseph, N., N. Anjum and Y.C. Tripathi. 2018. *Prunus cerasoides* D. Don: A Review on its Ethnomedicinal uses, Phytochemistry and Pharmacology. International Journal of Pharmaceutical Sciences Review and Research. 48(1), 62-69.

Kerby, J., S. Elliott, F. J. Maxwell, D. Blakesley, and V. Anusarsunthorn. 2000. Tree Seeds and Seedlings for Restoring Forests in Northern Thailand. Forest Restoration Research Unit, Biology Department, Science Faculty, Chiang Mai University, Thailand, pp. 152.

Kurniawan, V., D. M. Putri, S. Normasiwi and M. I. Surya. 2021. Phenology and morphological flower of *Prunus cerasoides* Buch.-Ham. ex D. Don. In *IOP Conference Series: Earth and Environmental Science*. 948(1), 012047. DOI: 10.1088/1755-1315/948/1/012047

Lachungpa, S. T. 2012. Green governance: policies, programmes and vision of the forestry sector of Sikkim. Forest, Environment and Wildlife Management Department, Gangtok, Sikkim.

Oktavia G. A. E., T. Iryadi, R. Warseno and H. Purnobasuki. 2023. The flowering process of *Prunus cerasoides* in Blai Botanic Gardens, Indonesia. Biodiversitas. 24(2), 1186-1191.

Pakkad, G., C. James, F. Torre, S. Elliott and D. Blakesley. 2004. Genetic variation of *Prunus cerasoides* D. Don, a framework tree species in northern Thailand. New forests. 27, 189-200. DOI: 10.1023/A:1025010403477

Pun. U. K., S. Shrestha and N. Bhandari 2023. Flowering of Himalayan cherry (Prunus cerasoides) in Nepal. Nepalese Floriculture. 26, 19-23

Tiwari, P., J. K. Tiwari and R. Ballabha. 2009. *Prunus cerasoides* D. Don (Himalayan Wild Cherry): A Boon to Hill-Beekeepers in Garhwal Himalaya. Nature and Science. 7(7), 21-23.

Civil Engineering, Original Article

Seismic Performance of CSEB Masonry Building

Hari Ram Parajuli[1*] and Bishwas Paudel[2]

[1] *Dept. of Civil Engineering, Pulchowk Campus, Tribhuwan University, Nepal*
[2] *Dept. of Civil Engineering, Thapathali Campus, Tribhuwan University, Nepal*

***CORRESPONDING AUTHOR:**

Hari Ram Parajuli
Email: hariparajuli@ioe.edu.np

ISSN : 2382-5359(Online), 1994-1412(Print)

DOI:
https://doi.org/10.3126/njst.v22i2.85242

Date of Submission: 14 Nov, 2021

Date of Acceptance: 13 Jul, 2025

ABSTRACT

The study aims to evaluate the seismic performance of Compressed stabilized earthen block (CSEB) masonry building with and without earthquake resistant features. FEM based structural analysis software ANSYS was used to model and analyse the structures. The building is modelled with macro-modelling approach and SOLID65 element was selected to represent the nature of the masonry. Linear and non-linear static analyses were conducted for both models. The nonlinear concrete model based on William-Warnke failure criteria was used. The pushover curves were developed for the normal masonry building (M1) and the timber reinforced masonry building (M2) to compare the seismic performance. The performance level of buildings was assessed using procedures stated in FEMA 356. The seismic analyses showed that the building model M2 having earthquake resisting features performed well during the earthquake. The first mode time period is decreased by 41.7%, the capacity is increased by 64.62% in x direction and 66.5% in y direction after addition of the reinforcement in M1 model. The performance level was at collapse stage (CO) in the unreinforced model in transverse direction, while, it was in range between immediate occupancy (IO) and life safety (LS) level after addition of timber reinforcement.

Keywords: FEM Based, Timber Reinforcement, Seismic Analysis

1. INTRODUCTION

Earthen walls are considered to be sustainable materials for their low embodied energy (Egenti & Khatib, 2016). Compressed stabilized earthen block (CSEB) masonry presents an environmentally and economically sustainable alternative to conventional residential construction materials such as clay brick masonry or concrete masonry (Maini 2005 and Hoff 2016). Compressed stabilized earthen blocks with specific composition and stabilization can show better performance against seismic failure (Riza, Rahman, & Zaidi, 2011). A number of researchers (Rigassi, 1985; ASTM International, 1989; Egenti, Khatib, & Oloke, 2014; Maini, 2005; Egenti & Khatib, 2016, Guinea 2015, Arumala & Gondal 2007) who have done extensive work in the field of earth construction

have identified unique advantages from their studies. Reinforcing and introducing seismic character in the building can be a way to reduce vulnerability of the building (Maini, 2005).This study focuses on assessing the structural resistance of CSEBs with and without reinforcement with the help of Finite Element Modelling (FEM). The objective of the study is to evaluate the seismic performance of CSEB masonry buildings with and without timber reinforcement.

2. MATERIALS AND METHODS

The research was carried out aiming at finding the result based on cause and effect. Literature review was followed by the selection of suitable CSEB masonry building configuration (Betti et al 2016). The assessment of effect of introducing timber reinforcement in the building was carried out with the help of FEM. During the modeling, the element type and material properties, failure criteria, loading criteria and boundary conditions were selected (Chavez & Meli, 2012, Endo et al 2015). A non-linear finite element analysis was carried out using the ANSYS software. The masonry was modeled using homogeneous macro-modeling approach with solid65 element. The building was analyzed for both gravity and seismic loadings. The natural period and vibration mode were computed to recognize the dynamic properties of structure. Then non-linear static pushover analysis was carried out to determine the performance of the building in terms of storey drift as per FEMA 356.

3. NUMERICAL MODEL

Large number of numerical modellings of masonry has been done by using in the researches using FEM (Lourenço 1996, Rots 1997, Zucchini et al. 2007, Parajuli et. 2008 & 2011, Parajuli 2012 & 12016, Parajuli & Ghimire 2020, Mark et al 2004). A typical CSEB (Keshav et al.2012, Patowary 2015) masonry building of one storey with area 40.54 m2 (7.05m x 5.75m) and 2.475 m high was selected (Fig. 1). Model M1 (Fig. 2) was CSEB without any reinforcement and Model M2 (Fig. 3) is CSEB with timber reinforcement in plinth, sill, lintel and roof.

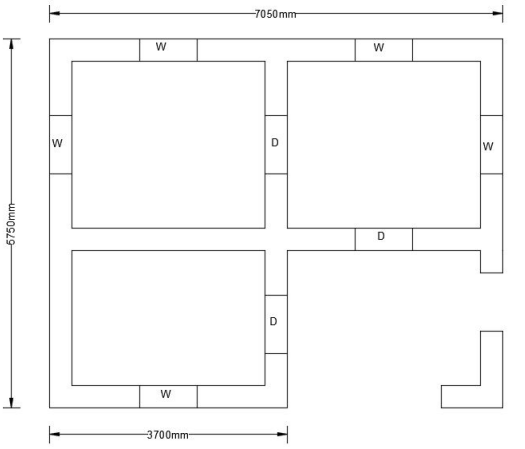

Fig.1: Plan of selected building

The size of the compresses stabilized earth block used is 300mm*200mm*100mm and block was stabilized by 8% cement as a stabilizer agent. The sizes of door and window are 900mm * 2100mm and 750mm * 1200mm respectively. The size of timber band is 75mm*100mm. The mechanical properties of the CSEB and CSEB masonry with 1:6 cement sand mortar was taken in reference to (Bhatta, 2015). The important factor was taken 1 as residential building, seismic zone V, response reduction factor (R) was taken 1.5 and medium type of soil was considered as seismic deign parameters as per IS 1893.The load are mentioned the Table 1.

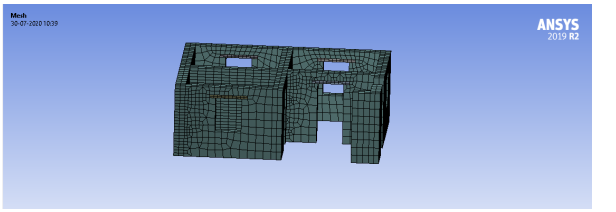

Fig.2: Model M1

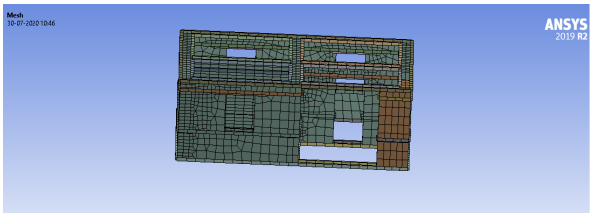

Fig.3: Model M2

Table 1: Load on the building

Roof live load	1.5 kN/m2
Live load	3.0 kN/m^2

The monotonic lateral loading was applied in the form of inertial load. The loads were applied through a horizontal acceleration. The static structural analysis included application of self-weight in a first step and a lateral load was applied in second step after the deformation. Material properties of CSEB (Murthy et al 2019), masonry and timber are explained in the Tables 2-4.

Table 2: Material property

Material	Description	Mean Value
CSEB	Specific weight of CSEB unit	1950 Kg/m^3
	Dry compressive strength of CSEB unit	8.1 MPa
	Wet compressive strength of CSEB unit	5.5 MPa
CSEB Masonry	Compressive strength of CSEB masonry	2.705 MPa
	Shear strength of CSEB masonry	0.146 MPa
	Modulus of Elasticity	338.125 MPa
	Shear Modulus	152.72 MPa
	Specific weight of masonry	1950 Kg/m^3
	Poisson's ratio	0.15
Timber	Density	650 Kg/m^3
	Modulus of Elasticity	11000 MPa
	Poisson's ratio	0.2

Table 3: Material properties for FEA simulation

Description	Value
Compressive strength of masonry	2.705Mpa
Tensile strength of masonry	0.27 Mpa
Open shear crack transfer coefficient	0.15
Closed shear crack transfer coefficient	0.75

Table 4: Stress-strain properties for accuracy

Stress (Mpa)	Strain(mm/mm)
0.0000	0.00000
0.8115	0.00240
1.7330	0.00580
2.3380	0.00920
2.6300	0.01260
2.7050	0.01600

4. SEISMIC ANALYSIS

Non-Linear Analysis

Analysis was evaluated through capacity curve, which represents the value of the applied action i.e. seismic load on the building in relation to the displacement of the control point. The most common control point is the top point of the structure. Pushover analysis can be performed in various direction (Rios & Dwyer 2018). The change in slope of a pushover curve can give an indication of damage of particular segments of the building. For, obtaining the pushover curve the procedure stated in FEMA-356 was followed and capacity curve was obtained. Procedures for performance assessment. The nonlinear concrete model based on William-Warnke 1975 failure criteria was used.

Capacity curves of both unreinforced and reinforced model (with different aspect ratios, compressive strength and loading conditions) are obtained by utilizing the previously mentioned analysis technique in ANSYS.

If a performance assessment is required, then the capacity curve is converted to Acceleration Displacement Response Spectrum (ADRS) format and compared with demand (in terms of acceleration spectrum).

The point where the capacity and the demand for that specific building intersects was regarded as the performance point and it was used in order to assess the seismic performance of the building.

The ranges for determining performance level for masonry in terms of storey drift is shown in Table 5.

Table 5: Performance drift limits (masonry buildings)

Building Type	Performance level for drift (%)		
	Collapse Prevention (CP)	Life Safety (LS)	Immediate Occupancy (IO)
Unreinforced Masonry	1	0.6	0.3
Reinforced Masonry	1.5	0.6	0.2

5. RESULT AND DISCUSSION

Modal analysis

From the free vibration analysis fundamental time periods were calculated and presented the Table 6.

Table 6: Fundamental Time-Period for M1 and M2

Model	Fundamental Time period (sec)		
	Empirical Formula		Modal Analysis
	X-direction	Y-direction	
M1	0.101	0.112	0.146
M2	0.101	0.112	0.085

The timber band reinforced as earthquake resistant features provided increases in stiffness of the building , maintaining structural integrity. Furthermore, the time period of building model reinforced with timber bands was seen to be less than that of unreinforced building model.

Development of capacity curves

Pushover analysis of the selected buildings was carried out in longitudinal (X) and transversal (Y) direction. Gravity was applied in a first loading step and then seismic forces proportional to mass of the structure were incremented until the analysis stops due to the collapse of the model. The capacity curves had been defined making reference to different control points. Finally, the performance point of buildings was determined as per FEMA 356.

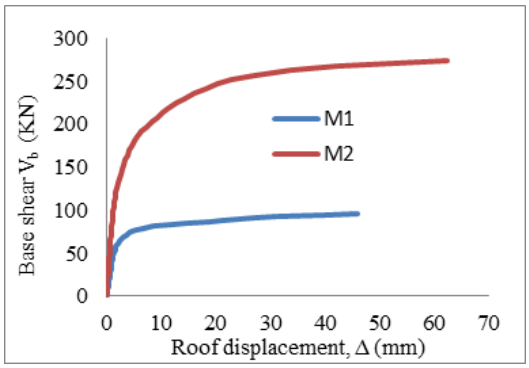

Fig.4: Capacity curve for M1 and m2 along x-direction

Along the longitudinal direction (+X), the first horizontal branch of the capacity curve was seen at base shear for 80 KN for M1 and 220 KN for M2. The ultimate state reached at base shear 97 KN and a roof displacement of 45.96 mm for model M1 while for model M2, the ultimate state is reached at base shear 274.175 KN and a roof displacement of 62.314 mm. Hence, it can be seen that after the addition of earthquake resistant features as wooden bands in building, the capacity of building increased by 64.62 % and roof displacement by 26%. This has been plotted in the Fig. 4

In the positive transverse direction (+Y), the first horizontal branch of the capacity curve is seen at base shear 72.346 KN for M1 and 235.79 KN for M2. The ultimate state is reached at base shear of 87 KN and a roof displacement 65.16 mm for model M1. Similarly, the ultimate state is reached at 260 KN and a roof displacement for model M2. Hence, it can be seen that after the addition of earthquake resistant features as timber bands in building, the capacity of building increase by 66.5 % and roof displacement is increase by 20%. The base share and displacement relations has been plotted in the Fig. 5.

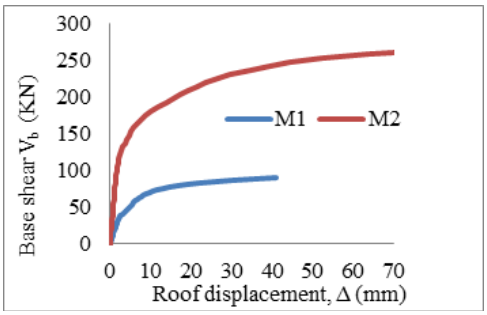

Fig.5: Pushover curve for M1 and M2 along y-direction

Building Performance

The performance point in terms of storey drift from analysis was found 0.81% for unreinforced masonry model M1 and 0.52% for reinforced masonry with timer bands model M2. The drift obtained from the analysis are shown in the Table 7. The comparison of building capacity and demand are show in the Figs 6-9.

Table 7: Roof drift of M1 and M2 in x and y direction

S. N	Loading	Model	Roof Displacement (mm)	Storey Height (mm)	Roof Drift (%)
1	Along X	M1	21.088	2475	0.852
2		M2	12.880	2475	0.520
3	Along Y	M1	25.967	2475	1.049
4		M2	15.525	2475	0.630

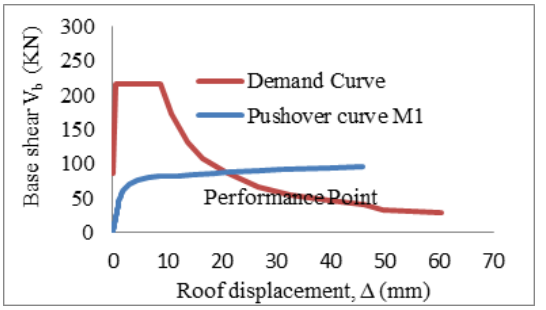

Fig.6: Performance level for M1along X-direction

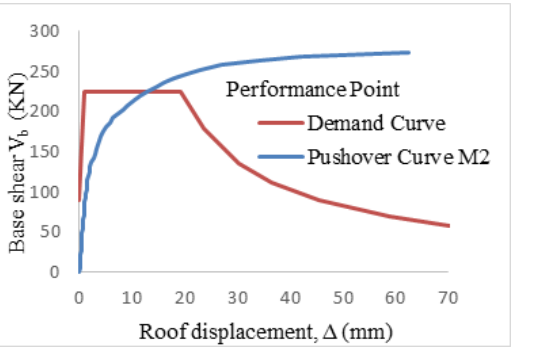

Fig.7: Performance level for M2 along X-direction

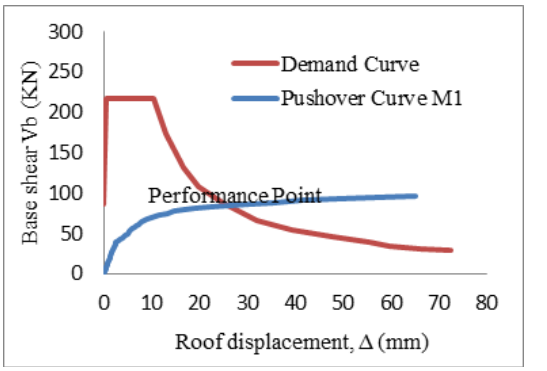

Fig.8: Performance level for M1 in Y direction

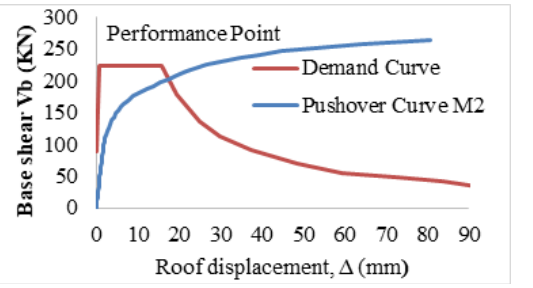

Fig.9: Performance level for M2 along Y-direction

The performance point in terms of storey drift from analysis was found to be found 1.05% for unreinforced masonry M1 and 0.63% for reinforced masonry with timer bands model M2. This due to the reason that timber bands give structural integrity to the building and during the earthquake, building shows box behavior and prevent from collapse and causalities.

6. CONCLUSION

From the investigation through numerical analysis,

following conclusions are made.

1. Comparing the fundamental time period of both models obtained from empirical formula and seismic analysis, the time period decreased in Model M2, due to change in mass and structural stiffness which was increased by addition of timber bands as earthquake resistant features in model M1. The first mode time period of Model M2 decreased by 41.7% than that of model M1.

2. Wooden bands can contribute to the improvement of the seismic capacity of CSEB masonry building in both cases. The capacity of model M1 increased by 64.62% and 66.5% in case of x-direction and y-direction respectively. These Earthquake resisting features could prevent collapse of out-of-plane walls of buildings.

3. From the numerical study, after the addition of timber bands, the performance point of the building as per FEMA-356 is increased. Even though the capacity curve increased with the timber bands, the performance level was at collapse stage at unreinforced model at transverse direction. However, building's performance level reached in range between immediate occupancy (IO) and Life safety (LS) level after addition of timber bands.

4. This study aims at making extensive use of raw earth as a building material, there by using a local resource to help develop technologies that are energy saving, eco-friendly (Auroville, 1989 & 2005) higher strength and sustainable development. The result of this study shall be used for the understanding the seismic behavior of unreinforced and timber reinforced masonry building as built by using locally available materials. It shall also be helpful in deciding the use of CSEB as alternative building materials and use of timber bands as earthquake resistant features for sustainable and low-cost housing. Macro modelling approach for modelling of masonry was considered during seismic analysis. In present study non-linear static analysis was carried out and for further work dynamic nonlinear analysis may also be carried out.

REFERENCES

ANSYS, R. 10, Release 10 Documentation for ANSYS, Element Reference.

Arumala, J. O., & Gondal, T. (2007). Compressed earth building blocks for affordable housing. In The construction and building research conference of the Royal Institution of Chartered Surveyors, pp. 95-98.

Building with Earthen in Auroville, 1989, https://www.earth-auroville.com/maintenance/uploaded_pics/Earth-in-Auroville.pdf.

Auroville Building Centre 2005, Earthen architecture for sustainable habitat and Compressed stabilized earth block technology', Introduced in Heritage program-Saudi Arabia.

Betti, Michele, Luciano Galano, and Auroville Andrea Vignoli (2016), Finite element modelling for seismic assessment of historic masonry buildings. Earthquakes and their impact on society.Springer, Cham, p. 377-415. DOI: 10.1007/978-3-319-21753-6_14

Bhatt T.P, (2015), Study on Strength Characteristics of Compressed Cement Stabilised Soil Block as an alternative wall making material in: Dissertation Degree in Civil Engineering T.U.,Pulchwok Campus.

Chávez, M., & Meli, R. (2012). Shaking table testing and numerical simulation of the seismic response of a typical Mexican colonial temple. Earthquake engineering & structural dynamics, 41(2), 233-253. DOI: 10.1002/eqe.1127

Endo, Y., Pelà, L., Roca, P., Da Porto, F., & Modena, C. (2015). Comparison of seismic analysis methods applied to a historical church struck by 2009 L'Aquila earthquake. Bulletin of earthquake engineering, 13(12), 3749-3778. DOI: 10.1007/s10518-015-9796-0

FEMA 356 (2000), Prestandard and Commentary for the Seismic Rehabilitation of Buildings, American Society of Civil Engineers, USA.

Guinea, G. V., Hussein, G., Elices, M., & Planas, J. (2000). Micromechanical modeling of brick-masonry fracture. Cement and concrete research, 30(5), 731-737. DOI: 10.1016/S0008-8846(00)00228-3

IS 1893-2002 (part-1), Criteria for earthquake resistance design of structure. Bureau of Indian standard, 2002.

Hoff, E. C. (2016), Appraisal of the Sustainability of Compressed Stabilized Earthen Masonry, University of Nebraska - Lincoln Digital Commons @ University of Nebraska - Lincoln, Architectural Engineering -- Dissertations and Student Research.

Keshav, Lakshmi, and V. G. Srisanthi. "Masonry CSEB Building Models under Shaketable Testing-An Experimental Study." Proceedings of World Academy of Science, Engineering and Technology. No. 72. World Academy of Science, Engineering and Technology (WASET), 2012.

Lourenço, P. B. "Computational strategy for masonry structures." Delft University of Technology and DIANA Research (1996).

Mark, JM, Peter, WK & Robert, EM 2004, Modelling soil/structure interaction for masonry structures, Journal of Structural Engineering,vol.130, pp. 641-649. DOI: 10.1061/(ASCE)0733-9445(2004)130:4(641)

Maini, S. (2005). Earthquake Resistant Buildings With Hollow Interlocking Blocks. Auroville: Auroville Earth Institute.

Maini, S. (2010). Production and Use of Compressed Earth Stabilized Earth Block: Code of Practice.

Murthy CVR, TV Srinivas, and Krishnamurthy Pandurangan, 2019, Behaviour of Compressed Stabilised Earth Block Masonry under Compressive Loading. International Journal of Engineering and Applied Sciences (IJEAS) ISSN (2019): 2394-3661. DOI: 10.31873/IJEAS.6.1.10

Parajuli H. R. (2012), Determination of the Kathmandu World Heritage brick masonry buildings' mechanical properties, 15 WCEE, Lisbon. Portugal.

Parajuli H. R., Kiyono J., Taniguchi H. (2011), Structural Assessment of the Kathmandu World Heritage Buildings, Proceeding of 31st Conference on Earthquake Engineering, JSCE, Tokyo, Japan.

Parajuli H. R. & Ghimire A., 2020, Investigation on Lateral Loading on Masonry Walls, Nepal Journal of Science and Technology (NJST), Vol 19(2), p. 33-40. DOI: 10.3126/njst.v20i1.39385

Parajuli H. R. 2016, Performance Evaluation of Mud Bonded Stone Masonry Houses under Earthquake Loadings,Nepal Journal of Science and Technology (NJST), Vol 17(1), p. 23-26. DOI: 10.3126/njst.v17i1.25060

Parajuli H., Kiyono J., Ono Y., 2008, Effectiveness of wooden bond beams in dry stone masonry houses, Journal of Applied Mechanics Vol.11. DOI: 10.2208/journalam.11.615

Patowary, B. N., Nath, N., Hussain, I., & Kakoti, H. J. (2015). Study of compressed stabilised earth block. International Journal of Scientific and Research Publications, 5(6), 2250-3153.

Rios, A. J., & O'Dwyer, D. (2018, April). FEM non-linear modelling of cob using ANSYS. In The 9th International Conference on Computational Methods (iccm2018).

Riza, Fetra Venny, Ismail Abdul Rahman, and Ahmad Mujahid Ahmad Zaidi. "Preliminary study of compressed stabilized earth brick (CSEB)." Australian Journal of Basic and Applied Sciences 5.9 (2011): 6-12.

Rots, JG 1997, Numerical models in Diana, In: Structural masonry - an experimental / numerical basis for practical design rules, (Eds. Rots J.G.) A.A. Balkem publishers, Rotterdam, Netherlands, pp.46-95. DOI: 10.1201/9781003077961-3

William, K. J., and E. P. Warnke. Constitutive model for the triaxial behaviour of concrete (paper III-l). Proc., Seminar on Concrete Structures Subjected to Triaxial Stresses. 1975.

Zucchini, A., & Lourenço, P. B. (2007). Mechanics of masonry in compression: Results from a homogenisation approach. Computers & structures, 85(3-4), 193-20 DOI: 10.1016/j.compstruc.2006.08.054

List of Reviewers and Editors Vol 22(2)

Prof. Dr. Paras Nath Yadav
Academician
Nepal Academy of Science and Technology (NAST)
Email: pnyadav219@gmail.com

Prof. Dr. Krishna Das Manandhar
Professor
Central Department of Biotechnology
Tribhuvan University
Email: krishna.manandhar@cdbt.tu.edu.np

Prof. Dr. Panna Thapa
Professor
Department of Pharmacy
Kathmandu University(KU)
Email: pannathapa@ku.edu.np

Dr. Krishna Pant
Reader
Central Department of Botany
Tribhuvan University
Email: Krishna.pant@cdb.tu.edu.np

Dr. Achyut Adhikari
Associate Professor
Central Department of Chemistry
Tribhuvan University
Email: achyutraj05@gmail.com

Dr. Jarina Joshi
Assistant Professor
Central Department of Biotechnology
Tribhuvan University
Email: jarinarjoshi@gmail.com

Prof. Dr. Jagat Kumar Shrestha
Associate Academician
Nepal Academy of Science and Technology (NAST)
Email: jagatshrestha@ioe.edu.np

Prof. Dr. Bal Krishna Bal
Professor
Department of Computer Science and Engineering
Kathmandu University(KU)
Email: bal@ku.edu.npEditorial Board Members

Dr. Deepak Raj Pant
Reader
Central Department of Botany
Tribhuvan University
Email: deepak.pant@cdb.tu.edu.np

Dr. Kshitij Charana Shrestha
Associate Professor
Institute of Engineering
Tribhuvan University
Email: kshitij.shrestha@pcampus.edu.np

Dr. Sarbesh Das Dangol
Assistant Professor
Madan Bhandari University of Science and Technology (MBUST)
Email: Sarbesh008@gmail.com

Dr. Ananda kumar Gautam
Director
Nepal Agricultural Research Council(NARC)
Email: akg.aerd.narc@gmail.com

Regd. No. 87/055/56 DAO/MOH/GON Volume 22(2) Jul-Dec 2023

Nepal Journal of Science and Technology (NJST) 22(2)
Published Year: 2025

Nepal Journal of Science and Technology (NJST)

NEPAL ACADEMY OF SCIENCE AND TECHNOLOGY (NAST)
Khumaltar, Lalitpur
GPO Box 3323, Kathmandu
Tel. 5547717, 5547715 Fax: 977-1-5547713
Email: njst@nast.org.np; scitechawareness@gmail.com

ISSN: 1994- 1412
8137 2157
e-ISSN 2382-5359 (Online)